

Instituto Tecnológico y de Estudios Superiores de Monterrey

Campus Monterrey

School of Engineering and Sciences



Synthesis, characterization, and application of micro- and nanomaterials for the removal of organic contaminants from groundwater and wastewater

A dissertation presented by

Carolina Orona Nívar

Submitted to the
School of Engineering and Sciences
in partial fulfillment of the requirements for the degree of

Doctor of Philosophy

In

Engineering Science

Monterrey Nuevo León, December 3rd, 2020

Acknowledgements

I would like to express my deepest gratitude to all those who have been side by side with me during my Ph.D. studies. My sincere thanks to my advisor Dra. Nancy Ornelas for her encouragement and guidance during every stage of my research. Also, I would like to thank my co-advisor Dr. Jürgen Mahlknecht as well as my thesis committee members: Dr. Netzahualpille Hernández, Dra. Alejandra García and Dr. Raúl García for their valuable contribution and feedback to this thesis.

I would like to thank Tecnológico de Monterrey for granting me a scholarship that covered the tuition fee during my Ph.D. studies. Likewise, I express my gratitude to CONACyT for the support provided through scholarship #583166 during my Ph.D. studies and #291250 during my international research stay.

Also, I would like to thank my loved family for their unconditional support through this endeavor. Thanks to my friends and colleagues: Eliana Torres, Iris Aguilar, Melisa Rodriguez, Raul García, Marcela Herrera, and Fabian Lugo for the good moments shared at the office and laboratory.

Finally, I would like to extend my appreciation to Professor Mika Sillanpää and to all the great people I met at the Department of Green Chemistry in Mikkeli. during my research stay in Finland. Thank you for your support, and friendship.

Dedication

My humble effort I dedicate to my sweet and loving

Father and Mother

José Luis Orona Rueda

Guadalupe Návar Ramírez

My Sister

Angélica Orona Návar

**Whose affection, love, encouragement and prays of day and night make me able
to get such success and honor**

Synthesis, characterization, and application of micro- and nanomaterials for the removal of organic contaminants from groundwater and wastewater

By

Carolina Orona Návar

Abstract

The increasing presence of chemicals and pharmaceuticals in the aquatic environment represents a latent threat both to ecosystems and to human health. Conventional treatment methods for water hardly eliminate these pollutants, which are usually dissolved in low concentrations (μgL^{-1} or ngL^{-1}). Because of their physicochemical characteristics, the use of micro- and nanomaterials in advanced treatment processes represents a feasible alternative to eliminate this kind of persistent pollutants.

In this study, different methods were applied to enhance the performance of micro- and nanomaterials for water treatment applications. Specifically, titanate nanotubes were synthesized, characterized, and successfully used for the adsorption of six organic pollutants of interest. First and second order kinetic models as well as, adsorption isotherms of Freundlich and Langmuir were investigated. Also, the photocatalytic activity of different bismuth-based materials was investigated. For instance, the photocatalytic efficiency of BiVO_4 was enhanced through rare-earth doping (Gd^{3+}) and a series of $\text{Bi}_2\text{O}_3/\text{rGO}/\text{Mo}_n\text{O}_{3n-1}$ all-solid-state ternary Z-scheme were synthesized as well. The synthesized photocatalysts were studied through photocatalytic degradation of selected contaminants and the photocatalytic experiments were carried out in different water matrices such as pure water, groundwater, or urban wastewater effluent. Also, different light sources were applied during photocatalytic processes to evaluate and compare the performance using conventional and LED light sources. To better understand the properties of the synthesized materials, scanning electron microscopy (SEM), X-ray diffraction (XRD), Raman spectroscopy, X-ray photoelectron spectroscopy (XPS), and diffuse reflectance spectroscopy (DRS) among other techniques, were applied.

All the synthesized materials, after being modified in their physical or chemical form, showed a better performance than the pristine materials during adsorption or photocatalysis treatments for the removal of persistent organic contaminants in the water.

Contents

Declaration of Authorship	3
Acknowledgements	4
Dedication	5
Abstract	6

Chapter 1

Introduction	9
1.1 Introduction	10
1.2 Motivation	13
1.3 Problem Statement and Context.....	13
1.4 Objectives	14
1.5 Hypothesis.....	15
1.6 Outline.....	15

Chapter 2

Adsorptive removal of emerging pollutants from groundwater by using modified titanate nanotubes.....	20
---	----

Chapter 3

$\text{Bi}_2\text{O}_3/\text{rGO}/\text{Mo}_n\text{O}_{3n-1}$ all – solid - state ternary Z-scheme for visible - light driven photocatalytic degradation of bisphenol A and acetaminophen in groundwater	44
--	----

Chapter 4

Gd^{3+} doped BiVO_4 and visible light-emitting diodes (LED) for photocatalytic decomposition of bisphenol A, bisphenol S, and bisphenol AF in water	68
---	----

Chapter 5

Removal of pharmaceutically active compounds and bacteria inactivation from urban wastewater effluents by UVA-LED photocatalysis with Gd ³⁺ doped BiVO ₄	97
--	----

Chapter 6

Conclusions	128
6.1 Conclusion.....	129
6.2 Contributions	129
6.3 Future work	130
Supplementary information	131
Curriculum Vitae	138

Chapter 1

Introduction

1.1 Introduction

Water pollution is not a local problem, but a global one. It is known that the availability of water resources is strongly linked to water quality since the presence of contaminants in water resources can prohibit different types of water uses [1]. Every day tens of million cubic meters of wastewater are discharged to water bodies in the world, and significant volumes of the discharged wastewater is not treated [2]. In recent years the threat to water resources quality as well as surrounding ecosystems has aroused scientific interest in presenting solutions through the development of treatment systems that are both effective and profitable [3,4].

Generally, treatments to obtain purified water require the use of physical, chemical, and/or biotechnological processes, which need to consume both resources and energy. Although the side effects on the use of such technologies have not been directly measured, there is no efficient method that does not contribute in a collateral way to environmental pollution.

A wide variety of chemical compounds have been detected in water bodies worldwide [5]. Among them, pollutants of emerging concern (PECs) have been widely studied since, although its adverse effects on ecosystems are known, the magnitude of such effects is still unknown [6,7]. Furthermore, most PECs are not considered within any regulatory framework so far [8]. PECs are often classified as persistent organic pollutants (POPs), veterinary drugs, endocrine disrupting compounds, pharmaceutically active compounds, food additives, and personal care products among others [7]. Within these categories, pharmaceutically active compounds represent a wide range of contaminants, since most of them are not completely assimilated within the organism and once they are excreted eventually reached water bodies as their original chemical form or as metabolites [9]. On the other hand, there are a variety of industrial compounds used for example, as additives, disinfectants, flame retardants, and plasticizers among others [10]. Many articles have reported the presence of such contaminants at low concentrations in water bodies, including rivers, groundwater, and effluent streams from WWTP. However, it should be noted that the conventional treatment methods seldom eliminate those contaminants which are found dissolved in wastewater in concentrations as low as $\mu\text{g/L}$ or ng/L [11].

Therefore, the implementation of effective, economic, and environmentally benign water treatment technologies that complement the conventional treatment process is desirable.

There are several approaches to apply nanotechnology for removing organic pollutants from water. Among the most used methods that incorporate micro and nanomaterials are adsorption, photocatalysis, catalytic ozonation, membrane filtration, and electrochemical processes among others [12,13]. For this study, adsorption and photocatalytic processes were selected as water treatments to study the characteristics of different materials to evaluate their potential and efficiency in pollutants removal from water.

Adsorption is a process in which generally particles of a gas or liquid (adsorbate) adhere to a solid surface (adsorbent). Adsorption and absorption are two different processes. In adsorption, the interaction occurs on the surface, while, in the absorption, the adsorbate molecules are immersed in the adsorbent (Figure 1).

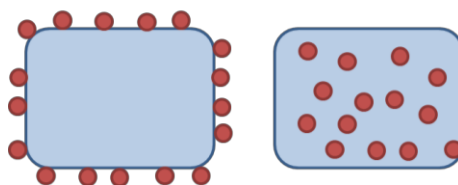


Figure 1. Adsorption vs absorption.

Adsorption depends on the type of interaction of the adsorbed molecules and the adsorbent surface. Those interactions can be either chemical (chemisorption) or physical (physisorption). In chemisorption, the formation of chemical bonds is favored due to the electron transfer. Chemical adsorption is limited to a monolayer and has stronger interactions than physical adsorption, which presents weaker interactions such as Van der Waals forces. In physisorption, the equilibrium is normally reached quickly and multilayer formation is possible. Adsorption processes are reversible (desorption). The adsorption is a function of the concentration of the adsorbate and the temperature of the solution [14]. Because adsorption occurs on the surface, the surface properties of adsorbent materials are very important (e.g. surface area).

The adsorption of a molecule on a solid surface is the fundamental principle that gives rise to a wide range of chemical and technological applications [15]. Adsorption is considered a universal water treatment technique that can be applied for the removal of contaminants which are soluble and insoluble in water.

Photocatalysis is a process in which a photoreaction is started and accelerated upon irradiation of light in the presence of a solid material known as a photocatalyst.

Photocatalytic processes in water follow five main steps:

- 1.- Transfer of reactants in water to the surface of photocatalysts.
- 2.- Adsorption of reactants onto the surface of the photocatalyst.
- 3.- Photonic activation of the surface of photocatalyst and reaction in the adsorbed phase.
- 4.- Desorption of reaction products.
- 5.- Elimination of reaction products from the interface region.

The formation of electron-hole pairs occurs when photocatalyst adsorb the light with energy equal to or greater than the band gap energy of photocatalyst. Thus, electrons (e^-) in the valence band (VB) jump to the conduction band (CB) leaving a positively charged hole (h^+) in the VB. Then, the photogenerated electrons and holes promote a series of redox reactions on the surface of the semiconductor (Figure 2). These reactions can be summarized as follows:

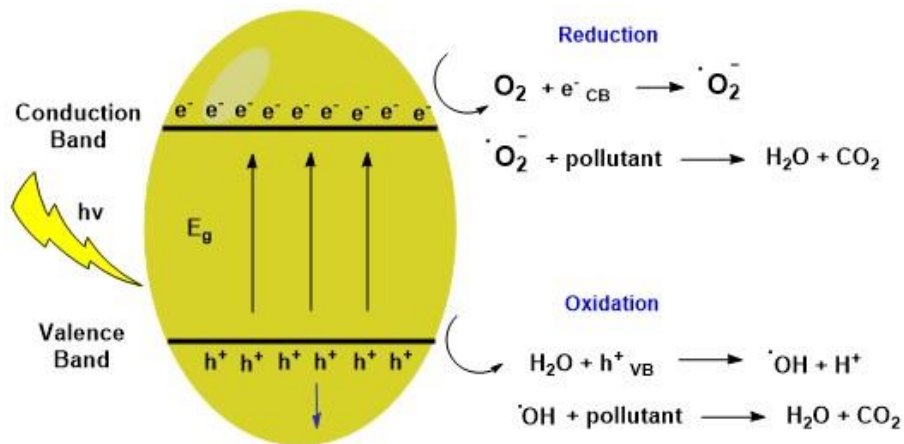
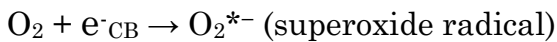
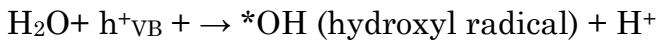
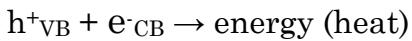
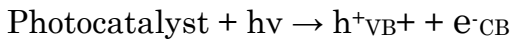


Figure 2. Mechanism of photocatalysis.

One of the main advantages of the photocatalytic processes have in comparison with other advanced treatments is that in an efficient process complete

mineralization could be reached leaving carbon dioxide and water as final products. Moreover, by taking advantage of solar applications or LED light sources, the processes may become affordable and benign to the environment.

In general, nanotechnology can play an important role in solving many of the problems related to water purification and quality. For this purpose, certain nanomaterials may be subject to modifications in their shape (spheres, nanotubes, thin films), size, composition (doping and composites), and/or structure (solid or mesoporous) to enhance their performance, specificity, and efficiency in complex pollutant removal processes. Thus, the applications of nanomaterials in water treatment are varied [13,16,17]. Nano-scale materials are generally favorable for heterogeneous photocatalysis since a higher specific surface area can be obtained with smaller particle size [18].

In this thesis, different micro- and nanomaterials such as titanate nanotubes, bismuth vanadate, and bismuth oxide were investigated as potential adsorbents or photocatalysts for efficient removal of a variety of organic pollutants including disrupting endocrine compounds, pharmaceutically active compounds, pesticides, and plastic additives among others.

1.2 Motivation

Water is one of the most valuable resources we have, however its quality and availability have been strongly affected by the presence of organic pollutants. These types of contaminants are seldom eliminated in conventional wastewater treatments.

The motivation for this research is focused on the enhancement of micro- and nanomaterials through physical and chemical modifications in order to be applied in advanced wastewater treatment processes. A combination of conventional and advanced water treatment could be adequate to efficiently remove most of the contaminants present in the water. Contributing to improving the quality and availability of water through efficient, profitable, and eco-friendly processes are our final goal.

1.3 Problem Statement and Context

The presence of emerging contaminants in the environment has become a critical issue worldwide. A variety of persistent organic pollutants such as

pharmaceuticals, personal care products, pesticides, flame retardants, and industrial additives, are released and dispersed into the water bodies every day [19,20]. Conventional treatment processes are not able to completely eliminate these contaminants, which are usually present in low concentrations (mg L^{-1} or ng L^{-1}) causing negative impacts on the environment and human health [6,7].

Heterogeneous photocatalysis, alone or combined with other processes, is a clear candidate to improve the current technological options for wastewater treatment. Semiconductors represent, by far, the most representative and widely investigated photoactive materials [21]. However, the main drawbacks of the mentioned photocatalytic semiconductors are that most of them are not ideal for solar photocatalytic applications due to its wide band gap, causing that less than 5% of the total solar energy can be utilized [22]. Moreover, the rapid recombination of electrons and holes is also a problem, since they recombine before arriving at the surface to initiate reactions, which sacrifices their performance [23].

Different approaches have been explored to avoid problems such as recombination and non-visible light active photocatalysts. For instance, it is possible to increase the concentration of charge carriers and suppress electron-hole recombination by making modifications on semiconductors band gap structure through doping, and/or the formation of heterojunctions [24,25].

1.4 Objectives

This thesis is focused on improving the performance of micro and nanomaterials through physical and chemical modifications for the efficient removal of organic pollutants in water through adsorption and photocatalytic processes. To achieve the goal set, the following specific objectives have been considered:

- I. To synthesize pristine materials for water treatment applications. Specifically, titanate nanotubes as adsorbents and bismuth-based materials as photocatalysts.
- II. To evaluate the feasibility of physical and chemical modifications to synthesized materials to enhance its potential as adsorbents or photocatalysts in the removal of organic contaminants.
- III. To perform physicochemical characterizations of pristine and modified materials by Raman spectroscopy, X-ray diffraction (XRD), nitrogen (N_2) sorption analysis, scanning electron microscopy (SEM), transmission electron microscopy (TEM), and UV-Vis diffuse reflectance spectroscopy (DRS) among others.

- IV. To study the effect that morphology control, chemical modification, doping, and formation of heterostructures have on the efficiency of the synthesized materials through quantitative analysis of contaminants degradation/transformation in adsorption or photocatalytic processes.
- V. To investigate the photocatalytic activity as well as the kinetics of the prepared bismuth-based photocatalysts for the degradation of organic pollutants from water using UV, UV-LED, visible, and visible-LED light sources.
- VI. To investigate adsorption capacity and kinetics of the prepared titanate nanotubes for the removal of organic pollutants in water.
- VII. To investigate the stability and the recyclability of the prepared adsorbents and photocatalysts through cycling use experiments.
- VIII. To propose the degradation/transformation mechanism of the pollutants studied and to evaluate the possible formation of by-products.
- IX. To evaluate the efficiency and applicability of the synthesized materials in a real water matrix such as groundwater and wastewater through analysis using techniques such as UV-Vis spectroscopy and high performance liquid chromatography (HPLC) with UV-Vis detector or coupled with mass spectroscopy.

1.5 Hypothesis

The physical and chemical modifications that are made to the materials will improve their efficiency during the adsorption or photocatalytic treatment for the removal of organic pollutants both in synthetic water samples and in complex matrices such as wastewater and groundwater.

1.6 Outline

This thesis is structured as follows:

Chapter 2 corresponds to the publication of [Orona-Navar *et. al.*,2018], which presents the adsorptive removal of six organic pollutants using unmodified titanate nanotubes as well titanate nanotubes modified by using a surfactant. The nanomaterials were synthesized, characterized, and analyzed as potential adsorbents of 2,4,6-trichlorophenol, oxytetracycline, 2,4-dichlorophenol, tolazamide, captopril, and metformin in water reaching a maximum adsorption percentage of 83%, 78%, 54%, 43%, 30%, and 47% respectively. First and second-order kinetic models, as well as, adsorption isotherms of Freundlich and Langmuir were investigated. The adsorption studies were carried out both in pure water and groundwater matrix.

Chapter 3 This chapter shows the investigation of the effect on photocatalytic efficiency of bismuth vanadate doped with different concentrations of gadolinium (Gd^{3+}). The photocatalytic performance of doped materials was evaluated through the decomposition of bisphenol A in water using an LED-visible light source. It was found that 4% of Gd^{3+} in molar mass showed the best photocatalytic efficiency. Decomposition of bisphenol S and bisphenol AF was studied using the photocatalyst with the optimal concentration of Gd^{3+} , reaching decomposition percentages up to $44.36\% \pm 2.74$, and $74.11\% \pm 5.09$, respectively after three hours of reaction. Reactive species were identified by scavenging tests and kinetic studies were performed. A decomposition pathway was proposed for the three studied pollutants.

Chapter 4 presents the article [Orona-Navar *et. al.*, 2020]. The mentioned article is focused on testing the most efficient synthesized photocatalyst ($BiVO_4$ doped with Gd^{3+} 4% in molar mass) on a real municipal wastewater effluent where 22 different pharmaceutically active compounds (PhACs) were detected. High photocatalytic removal efficiency (80 – 100%) was observed for some of the studied PhACs (e.g. naproxen and furosemide) whereas moderate efficiency (40 – 70%) was observed for others (e.g. acetaminophen and azithromycin) after 180 min (UVA dose = 139.5 Wh m^{-2} , $t_{30W} = 279 \text{ min}^{-1}$). Some of the studied PhACs like clarithromycin and Ibuprofen showed poor removal efficiency (< 30%). In addition to photocatalytic removal of PhACs, disinfection tests were performed to investigate the inactivation of Total coliforms, *Escherichia coli*, *Enterococci*, and *Klebsiella pneumoniae* naturally present in the effluent.

Chapter 5 presents the publication [Rubio-Govea, Orona-Návar C. *et.al.*, 2020], which investigates the photocatalytic activity of the ternary z-scheme composite $Bi_2O_3/rGO/Mo_nO_{3n-1}$ in the degradation of bisphenol A and acetaminophen under UV and visible light in both pure water and groundwater matrices. Through this study, it was found that the presence of reduced graphene oxide. plays an important role in the composite material since it helps in delaying the recombination time of photogenerated electron/hole (e^-/h^+) pairs, greatly improving the photocatalytic activity of the photocatalyst.

Chapter 6 Presents the general conclusion derived from this research. Also, the main contributions of this work have been highlighted. Finally, future work on this research line has been proposed.

References:

- [1] WWAP, Informe Mundial de las Naciones Unidas sobre el Desarrollo de los Recursos Hídricos 2017. Aguas Residuales: El Recurso Desaprovechado, Paris, 2017. <http://unesdoc.unesco.org/images/0024/002476/247647s.pdf>.
- [2] WWAP (United Nations World Water Assessment Programme), The United Nations World Water Development Report 2017. Wastewater: The Untapped Resource, Paris, 2017. www.unwater.org (accessed November 21, 2019).
- [3] X. Qu, P.J.J. Alvarez, Q. Li, Applications of nanotechnology in water and wastewater treatment., *Water Res.* 47 (2013) 3931–46. doi:10.1016/j.watres.2012.09.058.
- [4] M. Sillanpää, M.C. Ncibi, A. Matilainen, Advanced oxidation processes for the removal of natural organic matter from drinking water sources: A comprehensive review, *J. Environ. Manage.* 208 (2018) 56–76. doi:10.1016/J.JENVMAN.2017.12.009.
- [5] T. Aus Der Beek, F.A. Weber, A. Bergmann, S. Hickmann, I. Ebert, A. Hein, A. Küster, Pharmaceuticals in the environment-Global occurrences and perspectives, *Environ. Toxicol. Chem.* 35 (2016) 823–835. doi:10.1002/etc.3339.
- [6] P. Sathishkumar, R.A.A. Meena, T. Palanisami, V. Ashokkumar, T. Palvannan, F.L. Gu, Occurrence, interactive effects and ecological risk of diclofenac in environmental compartments and biota - a review, *Sci. Total Environ.* 698 (2020) 134057. doi:10.1016/j.scitotenv.2019.134057.
- [7] R. Naidu, V.A. Arias Espana, Y. Liu, J. Jit, Emerging contaminants in the environment: Risk-based analysis for better management, *Chemosphere.* 154 (2016) 350–357. doi:10.1016/j.chemosphere.2016.03.068.
- [8] R. Benson, O.D. Conerly, W. Sander, A.L. Batt, J.S. Boone, E.T. Furlong, S.T. Glassmeyer, D.W. Kolpin, H.E. Mash, K.M. Schenck, J.E. Simmons, Human health screening and public health significance of contaminants of emerging concern detected in public water supplies, *Sci. Total Environ.* 579 (2017) 1643–1648. doi:10.1016/J.SCITOTENV.2016.03.146.
- [9] B. Tiwari, B. Sellamuthu, Y. Ouarda, P. Drogui, R.D. Tyagi, G. Buelna, Review on fate and mechanism of removal of pharmaceutical pollutants from wastewater using biological approach, *Bioresour. Technol.* 224 (2017) 1–12. doi:10.1016/j.biortech.2016.11.042.

- [10] World Health Organization, Guidelines for drinking-water quality. Vol. 2, Health criteria and other supporting information: addendum, Guidel. Drink. Qual. 2 (1998). <http://www.who.int/iris/handle/10665/63844>.
- [11] A.R. Lado Ribeiro, N.F.F. Moreira, G. Li Puma, A.M.T. Silva, Impact of water matrix on the removal of micropollutants by advanced oxidation technologies, *Chem. Eng. J.* 363 (2019) 155–173. doi:10.1016/j.cej.2019.01.080.
- [12] R. Dewil, D. Mantzavinos, I. Poulios, M.A. Rodrigo, New perspectives for Advanced Oxidation Processes, *J. Environ. Manage.* 195 (2017) 93–99. doi:10.1016/J.JENVMAN.2017.04.010.
- [13] Z. Cai, A.D. Dwivedi, W.-N. Lee, X. Zhao, W. Liu, M. Sillanpää, D. Zhao, C.-H. Huang, J. Fu, Application of nanotechnologies for removing pharmaceutically active compounds from water: development and future trends, *Environ. Sci. Nano.* 5 (2018) 27–47. doi:10.1039/C7EN00644F.
- [14] G. Guirado, J.A. Ayllón, A simple adsorption experiment, *J. Chem. Educ.* 88 (2011) 624–628. doi:10.1021/ed100324s.
- [15] I.I. of Technology, Adsorption in Solution, 2009.
- [16] P. V Kamat, D.M. U, Nanoparticles in advanced oxidation processes, *Curr. Opin. Colloid Interface Sci.* 7 (2002) 282–287.
- [17] I. Mohmood, C.B. Lopes, I. Lopes, I. Ahmad, A.C. Duarte, E. Pereira, Nanoscale materials and their use in water contaminants removal-a review., *Environ. Sci. Pollut. Res. Int.* 20 (2013) 1239–1260. doi:10.1007/s11356-012-1415-x.
- [18] L. Zhang, Toward designing semiconductor-semiconductor heterojunctions for photocatalytic applications, *Appl. Surf. Sci.* 430 (2018) 2–17. doi:10.1016/J.APSUSC.2017.07.192.
- [19] N.H. Tran, M. Reinhard, K.Y.-H. Gin, Occurrence and fate of emerging contaminants in municipal wastewater treatment plants from different geographical regions-a review, *Water Res.* 133 (2018) 182–207. doi:10.1016/J.WATRES.2017.12.029.
- [20] T. Deblonde, C. Cossu-Leguille, P. Hartemann, Emerging pollutants in wastewater: A review of the literature, *Int. J. Hyg. Environ. Health.* 214 (2011) 442–448. doi:10.1016/j.ijheh.2011.08.002.
- [21] J.M. Coronado, F. Fresno, R. Portela, Design of Advanced Photocatalytic

Materials for Energy and Environmental Applications, 2013.
doi:10.1007/978-1-4471-5061-9.

- [22] L. V. Bora, R.K. Mewada, Visible/solar light active photocatalysts for organic effluent treatment: Fundamentals, mechanisms and parametric review, *Renew. Sustain. Energy Rev.* 76 (2017) 1393–1421. doi:10.1016/j.rser.2017.01.130.
- [23] O. Monfort, G. Plesch, Bismuth vanadate-based semiconductor photocatalysts : a short critical review on the efficiency and the mechanism of photodegradation of organic pollutants, *Environ. Sci. Pollut. Res.* 25 (2018) 19362–19379.
- [24] A. Malathi, J. Madhavan, M. Ashokkumar, P. Arunachalam, A review on BiVO₄ photocatalyst: Activity enhancement methods for solar photocatalytic applications, *Appl. Catal. A Gen.* 555 (2018) 47–74. doi:10.1016/j.apcata.2018.02.010.
- [25] J. Low, J. Yu, M. Jaroniec, S. Wageh, A.A. Al-Ghamdi, Heterojunction Photocatalysts, *Adv. Mater.* 29 (2017). doi:10.1002/adma.201601694.
- [26] C. Lee, S. Liu, H.-C. Chen, Application of hydrothermal method derived titanate nanotubes as adsorbents., *Recent Pat. Nanotechnol.* 3 (2009) 203–212. doi:10.2174/187221009789177786.
- [27] L.-C. Juang, C.-K. Lee, C.-C. Wang, S.-H. Hung, M.-D. Lyu, Adsorptive Removal of Acid Red 1 from Aqueous Solution with Surfactant Modified Titanate Nanotubes, *Environ. Eng. Sci.* 25 (2008) 519–528. doi:10.1089/ees.2007.0118.
- [28] H.-P. Chao, C. Lee, L. Juang, Y. Han, Sorption of Organic Compounds , Oxyanions , and Heavy Metal Ions on Surfactant Modified Titanate Nanotubes, *Ind. Eng. Chemistry Res.* 52 (2013) 9843–9850. doi:10.1021/ie4010699.

Chapter 2

Adsorptive removal of emerging pollutants from groundwater by using modified titanate nanotubes

This Chapter has been published as:

C. Orona-Návar, R. García-Morales, R. Rubio-Govea, J. Mahlkecht, R.I. Hernandez-Aranda, J.G. Ramírez, K.D.P. Nigam, N. Ornelas-Soto, Adsorptive removal of emerging pollutants from groundwater by using modified titanate nanotubes, *J. Environ. Chem. Eng.* 6 (2018) 5332–5340. doi:10.1016/j.jece.2018.08.010.

1. Introduction

In the last few decades, a wide variety of chemical compounds have been detected in water bodies worldwide [1]. Some of them are known as pollutants of emerging concern (PECs) and have been extensively studied since they are considered a threat both to the aquatic ecosystems and to the human health [2,3]. The concern around PECs lies in the lack of knowledge about the magnitude of the negative effects that these pollutants might have on ecosystems; moreover, most of PECs are not considered within any regulatory framework so far [4].

PECs have been classified as persistent organic pollutants (POPs), veterinary drugs, endocrine disrupting compounds, pharmaceuticals, food additives and personal care products among others [5]. Within these categories, pharmaceuticals cover a wide range of compounds, which have been originally developed to promote a biological effect in the human body. However, they are seldom completely assimilated within the organism. Therefore, most pharmaceuticals are excreted either in their original chemical form or as metabolites, reaching water sources in different ways [6]. On the other hand, there are industrial compounds such as chlorophenols, which are widely used as additives for wood, antiseptics, disinfectants, as well as, to produce pesticides. Among all possible chlorinated phenolic compounds, 2-chlorophenol, 2,4-dichlorophenol and 2,4,6-trichlorophenol are most likely to affect water, producing chlorination by-products in wastewater treatment plants (WWTP) [7].

Many articles have reported the presence of PECs at low concentrations in water bodies, including rivers, groundwater and effluent streams from WWTP among others. The conventional methods used in WWTP, such as biological treatments, are not efficient enough to eliminate PECs [8]. Antidiabetic Metformin drug, for instance, is one of the most prescribed pharmaceuticals, it has been detected in surface water, groundwater and wastewater at maximum concentrations of 2.64, 1.58 and 222.10 μgL^{-1} respectively [9–11]. Likewise, antibiotics like oxytetracycline, captopril, as well as phenolic compounds such as 2,4-Dichlorophenol have been found at concentrations around 6.79, 13.34 and 230 μgL^{-1} respectively [12–14].

In parallel to efforts aimed at assessing the toxicological behavior of these pollutants, there is also arduous research work, focused on their removal from surface and groundwater bodies. Among the most popular alternative techniques used to remove PECs, advanced oxidation processes (AOPs) based on ozone, UV radiation, and gamma radiation, as well as electrochemical processes have been extensively studied; nonetheless, the main drawback of these advanced

treatments is usually a generation of toxic by-products [15]. Removal by adsorption processes have also been widely investigated by using diverse adsorbent substances, such as nanomaterials [16,17]. In this context, carbon nanomaterials (e.g. carbon nanotubes) have been used to adsorb a variety of chemicals with high efficiencies [18,19]. Nevertheless, obtaining these carbon nanomaterials involves high costs, complex production processes, as well as bioaccumulation and toxicity effects in biota exposed to this material [20,21].

Titanate nanotubes (TNTs) have shown an extraordinary sorption capacity, because of its porosity, surface area, and ion exchange capacity; making them suitable candidates to adsorb organic molecules [22,23]. The TNTs surface is apparently positively-charged in acidic solution and negatively charged in alkaline solution. However, if the TNTs surface is modified with a surfactant or other organic cations, a positive surface charge can be induced by both acid and alkaline solutions, and then, anionic compounds can also be adsorbed [24,25].

In this work, the adsorption behavior of 2,4-dichlorophenol, 2,4,6-trichlorophenol, Tolazamide, Captopril, Oxytetracycline, and Metformin was studied for the first time using TNTs and modified titanate nanotubes (TNTs-CTAC) as adsorbents. Experiments were carried out in both ultrapure water and groundwater samples, in order to evaluate the effect of a complex matrix (groundwater) on the removal of these organic pollutants.

2. Methods and Instrumentation

2.1 Materials

High purity grade standards of 2,4-dichlorophenol (2,4-DCP), 2,4,6-trichlorophenol (2,4,6-TCP), tolazamide (TLZ), metformin (MET), captopril (CTP), and oxytetracycline (OTC) were obtained from Sigma Aldrich, USA. Acetonitrile and ethanol (HPLC grade) were supplied from Tedia. Titanium oxide nanoparticles (TiO_2) (Degussa, P25) were supplied by Sigma-Aldrich; and finally, Hexadecyltrimethylammonium chloride (CTAC) from Sigma.

2.2 Synthesis of TNTs and TNTs-CTAC

TNTs were obtained via a hydrothermal method. Typically, 2 g of TiO_2 nanoparticles were mixed with 50 ml of 10 M NaOH solution; and followed by a hydrothermal treatment of the mixture at 150°C in a Teflon-lined autoclave for 36 h. The precipitate was washed with deionized water and 0.001 N HCl aqueous solution until the pH value of the rinsing solution was nearly neutral. Afterwards, the TNTs were immersed into 200 ml HCl aqueous solution (0.1 N) for 24 h, then washed with deionized water and finally dried at 105°C for 24 h

and stored in glass vials at room temperature. According to Chung-Kung Lee et al. [26], under these conditions a nanotubular structure with high surface area as well as high pore volume is ensured.

In order to obtain TNTs with a positively charged surface, a methodology similar to the suggested by Chung-Kung Lee et al. [22] was followed. Briefly, 1 g of TNTs were dispersed in 100 ml of deionized water, then CTAC was added to the solid suspension in a weight ratio of CTAC: TNTs (0.5:1) and remained in agitation for 6 h to promote a cation exchange between Na^+ and CTAC ions. Finally, the TNTs were washed, freeze-dried and stored in glass vials until used. These modified TNTs were denoted as TNTs-CTAC.

2.3 Characterization of nanomaterials (TNTs and TNTs-CTAC)

Scanning electron micrograph (SEM) images of TNTs and TNTs-CTAC were recorded on a JSM-7800 (JEOL) electron microscope operating at 15 kV. An X-ray powder diffractometer (Empyrean) with Cu K α radiation source was used to determine the crystalline structure of the adsorbents. Specific surface area and mesoporous structure were characterized by nitrogen adsorption-desorption isotherms using the Autosorb-1 (Quantachrome) at 77 K. Surface area was determined from the Brunauer-Emmett-Teller (BET) equation, and pore size distribution was analyzed by using the Barrett-Joyner-Halenda (BJH) method. Raman spectra were acquired with a Renishaw inVia Raman spectrometer. Sample excitation was carried out with an 830nm diode laser with a nominal output of 100mW.

2.4 Organic Pollutants

Certain persistent organic compounds were selected to be adsorbed onto TNTs and TNTs-CTAC. All the selected compounds with purities greater than 95% were obtained from Sigma Aldrich. All the standard solutions were prepared in ultra-pure water. An antibiotic (Oxytetracycline), a β -blocker (Captopril), two antidiabetics (Metformin, Tolazamide) and two phenolic compounds (2,4-dichlorophenol, 2,4,6-trichlorophenol) were selected for these adsorption studies. Their chemical structures are shown in Fig. 1.

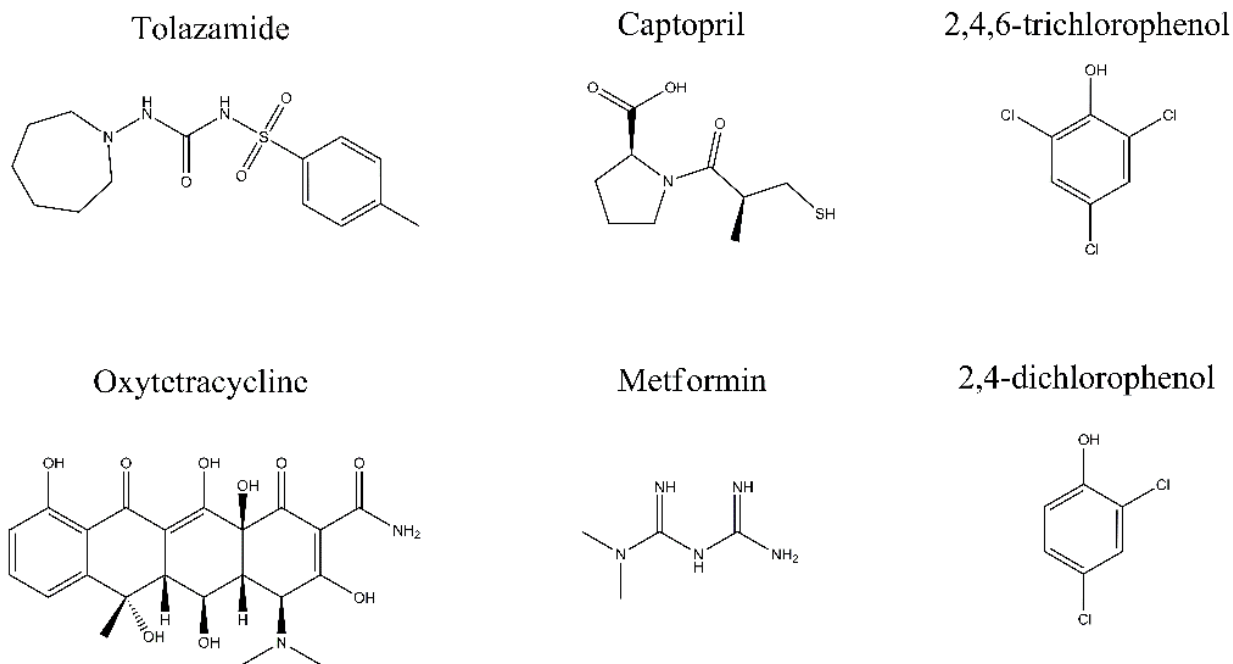


Figure 1. Chemical structures of organic pollutants.

2.5 Adsorption study

Adsorption experiments were performed at constant temperature (27 ± 1 °C) and stirring (550 rpm). Adsorption kinetics were first performed to find the equilibrium adsorption time. Thus, based on Xiong et al. [27] 0.05 g of adsorbent nanomaterial were suspended in water by ultrasound and added to a 100 ml solution with an initial concentration of 30 mg L^{-1} of a particular pollutant (adsorbate). For all the studied pollutants this adsorbent/adsorbate ratio is adequate to gradually observed the saturation of adsorption sites until equilibrium is reached. Aliquots were withdrawn from prepared solution at different contact time intervals and centrifuged at 13500 rpm for 5 minutes. The supernatant was filtered with a $0.45 \mu\text{m}$ PTFE membrane and analyzed by high performance liquid chromatography (HPLC). According to previous tests (data not shown), where the concentration of pollutant standard solutions was measured before and after passing them through a PTFE syringe filter, it was demonstrated that there was not adsorption during the filtration process. Chromatographic analysis was carried out with a ZORBAX Eclipse XDB C18 (150 mm x 4.6 mm, 5μ) column at room temperature using an Agilent 1200 series with a UV visible detector. The mobile phase, flux, and time were varied depending adsorbate characteristics (Table 1).

Table 1. HPLC parameters for analysis of selected organic pollutants.

	Tolazamide	Metformin	Captopril	2,4-Dichlorophenol 2,4,6-Trichlorophenol	Oxytetracycline
Eluents	A: 90% Acetonitrile. B: 10% Acetonitrile pH 3	A: K ₂ HPO ₄ B: Methanol	A: 90% Acetonitrile. B: 10% Acetonitrile pH 3.	A: Water (0.1% Formic acid). B: Acetonitrile (0.1% formic acid).	A: Water (0.1% formic acid). B: Acetonitrile (0.1% formic acid).
Elution Mode	Gradient 0 min – A 10% 5 min – A 35% 15 min – A 90%	Isocratic: A – 40% B – 60%	Isocratic: A – 50% B – 50%	Gradient: 0 min – A 50% 11 min – A 10% 15 min – A 50%	Isocratic: A – 85% B – 15%
Analysis Conditions	Flux: 0.5 ml/min Time: 25 min Injection: 20 µl λ = 225 nm	Flux: 1 ml/min Time: 10 min Injection: 20 µl λ = 230 nm	Flux: 0.8 ml/min Time: 10 min Injection: 20 µl λ = 225 nm	Flux: 1 ml/min Time: 16 min Injection: 20 µl λ = 280 nm	Flux: 1 ml/min Time: 10 min Injection: 20 µl λ = 360 nm

Kinetic experiments revealed that 180 min were required to reach the equilibrium at the adsorption system. Thereby, the amount of pollutant adsorbed onto TNTs or TNTs-CTAC at equilibrium (q_e) and at time 't' (q_t), were calculated by equations (1) and (2), respectively. Where, C_0 is the initial concentration and C_t is the concentration at time t (mg L^{-1}) of the adsorbates in aqueous solution, V is the volume (L) of the liquid phase and m is the mass (g) of the adsorbent. The removal efficiency (R), was calculated according to equation (3).

$$q_e = (C_0 - C_e) V/m \quad \text{Eq. (1)}$$

$$q_t = (C_0 - C_t) V/m \quad \text{Eq. (2)}$$

$$R = ((C_0 - C_t)/C_0) * 100 \quad \text{Eq. (3)}$$

Similarly, the experiments to obtain the Langmuir and Freundlich isotherms were carried out in 100 ml solutions varying adsorbate concentrations (ranging from 5 to 40 mg L^{-1}); aliquots were withdrawn at the initial time and after 180 min, when the equilibrium was reached. Then, concentrations were determined by HPLC (Table 1). Each experiment was done triplicate and the data were averaged. Blanks were also performed.

Based on the physicochemical characteristics of the pollutants (supplementary material S1) and supported by preliminary tests, TNTs were chosen to adsorb metformin, while TNTs-CTAC, were used to adsorb tolazamide, captopril, oxytetracycline, 2,4-dichlorophenol, and 2,4,6-trichlorophenol. Likewise,

preliminary experiments were carried out to determine the optimal pH for adsorption of each pollutant. Thus, it was found that 2,4,6-TCP, OTC, CTP and TLZ were better adsorbed at pH 4, while for 2,4-DCP and MET pH 6 was more adequate. For adsorption experiments, the required pH was adjusted by adding diluted solutions of NaOH/HCl.

2.5.1 Adsorption Isotherms

Langmuir and Freundlich isotherm models were applied in order to describe the relationship between the adsorbate concentration in solution and the adsorbent. Equations (4) and (5) describes Langmuir [28] and Freundlich [29] models respectively.

$$q_e = Q_m K_L C_e / (1 + K_L C_e) \quad \text{Eq. (4)}$$

$$q_e = K_F C_e^{1/n} \quad \text{Eq. (5)}$$

Where q_e represents the amount of pollutant adsorbed at equilibrium (mg g^{-1}), Q_m is the maximum adsorption capacity of the adsorbent (mg g^{-1}), C_e is the equilibrium concentration (mg L^{-1}), K_L is the Langmuir constant (L mg^{-1}). K_F is the Freundlich constant (mg g^{-1}) (mg L^{-1})- $1/n$, and $1/n$ is the heterogeneity factor.

2.5.2 Adsorption Kinetics

Two kinetic models were used to describe the adsorption process. The pseudo-first-order (PFO) model proposed by Lagergren [30] is expressed according to the following Equation (6).

$$q_t = q_e (1 - \exp(-k_1 t)) \quad \text{Eq. (6)}$$

Where q_e and q_t are the adsorption capacity (mg g^{-1}) at equilibrium and the elapsed time t , respectively, and k_1 is the pseudo-first order rate constant (min^{-1}).

The pseudo-second order (PSO) equation, first proposed by Blanchard et al. [31] can be expressed as equation (7)

$$q_t = t / [(1/k_2 q_e^2) + (t/q_e)] \quad \text{Eq. (7)}$$

Where k_2 represents the pseudo-second order rate constant ($\text{g mg}^{-1} \text{min}^{-1}$). PFO and PSO kinetic models have been widely applied to describe adsorption of an adsorbate from an aqueous solution and are applicable for the initial adsorption stages and the whole range of adsorption, respectively.

Equilibrium and kinetic parameters were obtained by fitting the models studied with experimental data through non-linear regression. Polymath 6.10 and OriginPro 8.5 Software were employed to make the relevant calculations, and the adjusted determination coefficient (R^2 adj.) as well as the average relative error (ARE) were calculated according to equations (8) and (9), respectively, to guarantee the fit quality [32,33].

$$R^2_{adj} = 1 - ((n - 1)/(1 - (n_p + 1))) (1 + R^2) \quad \text{Eq. (8)}$$

$$ARE = 100/n \sum_{i=1}^n |(q_{i,exp} - q_{i,cal})/q_{i,cal}| \quad \text{Eq. (9)}$$

Where n is the number of experimental points, n_p is the number of model parameters, $q_{i,exp}$ is the experimental value of q (adsorption capacity) measured at equilibrium, and $q_{i,cal}$ is each value of q obtained from the fitted model.

Residual analysis was carried out to determine whether the non-linear isotherm and kinetic models were adequate and meets the assumptions of normality, constant variance and independence. Minitab 17 software was used for mentioned calculations.

2.6 Groundwater experiments

Kinetics and removal efficiencies were also determined using groundwater samples, obtained from several aquifers located in Nuevo Leon, a state, in the northeastern Mexico. The pH in groundwater samples varied between 6.77 and 7.88, indicating neutral to slightly alkaline water conditions within the studied area. The experiments to obtain the adsorption kinetics were carried out following the methodology mentioned in section 2.5, substituting ultra-pure water for groundwater.

3. Results and Discussion.

3.1 Characterization of adsorbents

The morphologies of TNTs and TNTs-CTAC are shown in Fig. 2. They show a nanotubular structure with an average outer diameter of 10.27 ± 2.74 and 11.90 ± 2.84 nm for TNTs and TNTs-CTAC, respectively. Both materials with a length of hundreds of nanometers. Insets on Fig. 2 show the diameter size distribution of TNTs and TNTs-CTAC. It is evident that the nanotubular structure is maintained after CTAC modification.

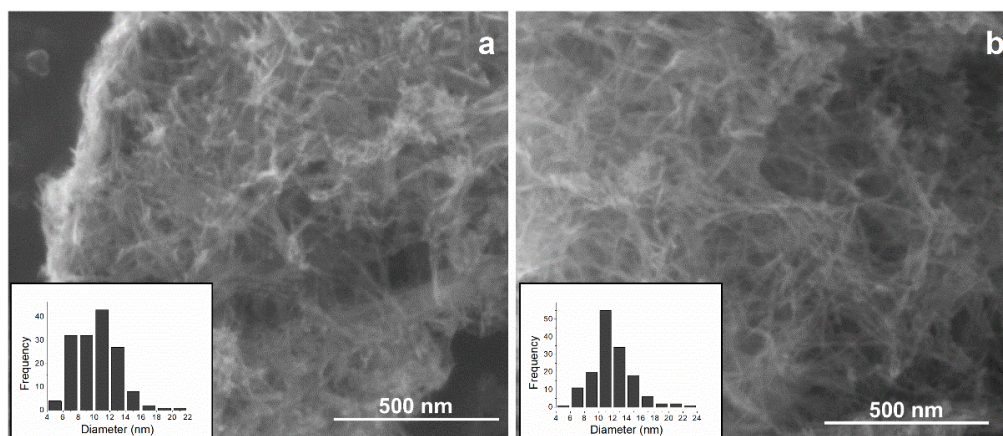


Figure 2. SEM micrography: a) TNTs b) TNTs-CTAC.

XRD patterns shown in Fig. 3 indicate that no significant changes occur in the crystalline structure after modification of the nanotubes. The six possible reflections detected at 2θ were 24.5, 28.5, 32, 38.1, 43.8, and 48.3, attributed to the presence of hydrogen and sodium titanate compounds [34]. These compounds favor interaction between the adsorbent and adsorbates, for instance, promoting chemisorption through the formation of hydrogen bonds [35].

The precise crystalline structure is still under discussion, as it is known that using different temperatures during the hydrothermal treatment, as well as different HCl concentrations during acid rinsing, may induce significant changes in the phase structure of TNTs [36]. Nevertheless, the layered trititanic acid ($H_2Ti_3O_7$) with a monoclinic crystal structure has been widely accepted so far [37].

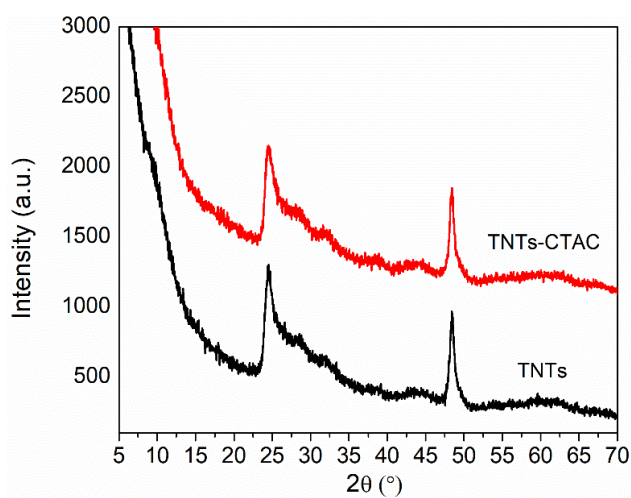


Figure 3. XRD patterns of adsorbent nanomaterials: TNTs and TNTs-CTAC.

In agreement with SEM and XRD results, the Raman spectra of TNTs does not differ from that of TNTs-CTAC (Fig. 4), in such a way that, it can be inferred that CTAC has probably been adsorbed on the nanotubes surface by ion exchange instead of forming a weak bond onto TNTs surface [38,39]. In addition, it is possible that the amount of CTAC present in the TNTs-CTAC, after several washing steps was not enough to be noticeable by Raman spectroscopy. The characteristic Raman peaks of titanate nanotubes (187, 269, 453, 660 and 828 cm^{-1}) are mainly attributed to titanate species [40–42]. Lee C. et. al. [39] has reported the presence of anatase phase in titanate nanotubes synthesized over 160°C. Therefore, anatase phase is not present either TNTs and TNTs-CTAC as it ascertained by Raman and XRD spectra.

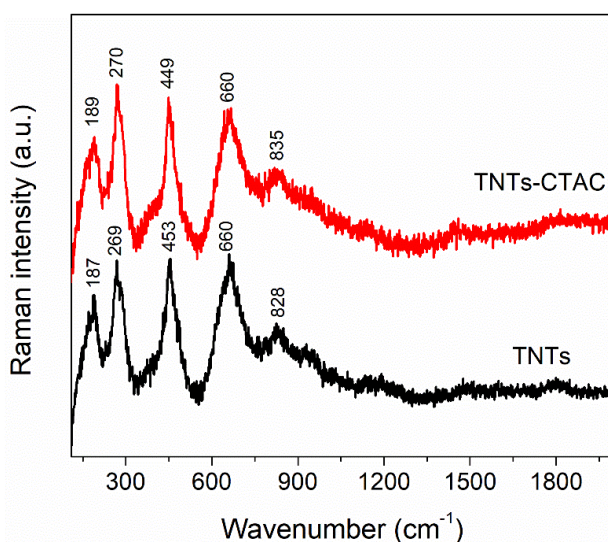


Figure 4. Raman spectra of titanate nanotubes (TNTs) and modified titanate nanotubes (TNTs-CTAC).

The obtained BET surface areas were 457.9 $\text{m}^2 \text{g}^{-1}$ and 277.4 $\text{m}^2 \text{g}^{-1}$ for TNTs TNTs-CTAC respectively, and both are higher than those previously reported by several authors (Table 2). A high surface area is desirable in order to have more active sites in the nanomaterial and consequently, achieve better removal efficiencies in adsorption processes [16]. BET surface area and pore volume of TNTs-CTAC are slightly smaller than those obtained for unmodified TNTs, suggesting that CTAC molecules may be occupying a space in the surface area of the nanotubes.

Table 2. Comparison of BET surface area and porosity of TNTs and TNTs-CTAC.

	Surface area (BET) [m ² /g]	Pore volume (BJH) [cc/g]	Average pore diameter [nm]	Reference
TNTs	457.9	1.838	16.03	Present work
	241	1.09	14.7	[26]
	221.8	0.874	13	[27]
	276	0.964	14.4	[28]
TNTs-CTAC	277.4	1.424	19.91	Present work
	45.3	0.206	8.9	[27]
	231	0.783	16.9	[28]

Fig. 5 shows the nitrogen adsorption-desorption isotherms and pore size distribution for TNTs and TNTs-CTAC. Both samples are classified as type IV isotherms, where the characteristic formation of a hysteresis loop suggest capillary condensation at mesopores (2-50 nm). The observed hysteresis loops can be classified as H3 type and exhibit the formation of slit-shaped pores due to the presence of aggregates of plate-like particles [43].

The presence of larger pores (Fig. 5, inset) can be mainly attributed to the empty cavities formed by aggregation of TNTs [44] as observed in SEM images.

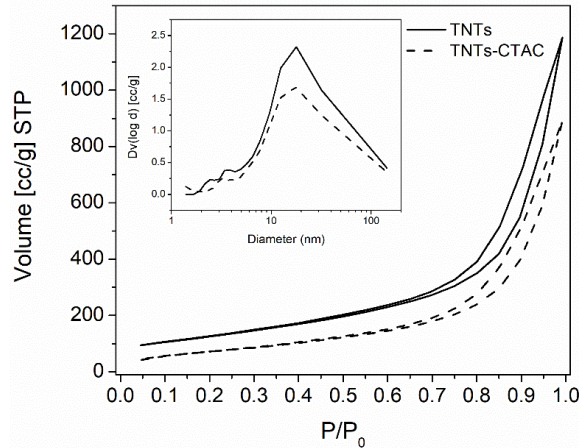


Figure 5. Nitrogen adsorption-desorption isotherms and pore size distributions of TNTs and TNTs-CTAC.

3.2 Adsorption kinetics

The effect of contact time on the adsorption of tolazamide, captopril, oxytetracycline, 2,4-dichlorophenol, and 2,4,6-trichlorophenol onto TNTs-CTAC, and metformin onto TNTs is shown in Fig. 6. A rapid initial uptake during the first 30 minutes of contact can be observed; by further increasing contact time,

equilibrium was reached at 180 minutes for all the pollutants, with coefficients of variation lower than 5% of two consecutive measurements (180 and 300 min); except for oxytetracycline, which after 180 minutes was still being adsorbed. For the purposes of this work, the equilibrium for all the studied pollutants will be considered at 180 min.

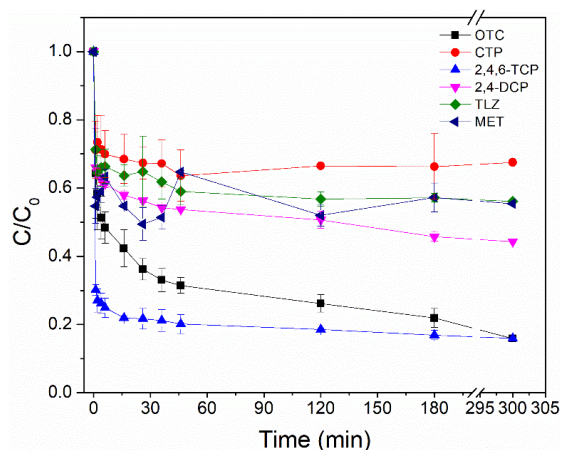


Figure 6. Effect of contact time on adsorption of oxytetracycline (OTC), captopril (CTP), 2,4-dichlorophenol (2,4-DCP), 2,4,6-trichlorophenol (2,4,6-TCP), and tolazamide (TLZ) by TNTs-CTAC, and metformin (MET) by TNTs. (adsorbent dosage = 0.5 gL⁻¹ and T=27°C).

Fig. 7, shows the removal efficiencies (%) reached for each pollutant. Pollutants were fast adsorbed onto nanotubes during the first five minutes and then more slowly until equilibrium was reached (around 180 min). Therefore, the best efficiencies, were achieved for 2,4,6-TCP, OTC, and 2,4-DCP, with 83%, 78% and 54%, respectively. Chao H. et al. [35] found that TNTs surface is positively charged in acidic solutions and negatively charged in alkaline solutions, based on their isoelectric point. They also reported a positively charged surface in the pH range of 3-11 for TNTs-CTAC. Hence, affinity of the studied pollutants to TNTs or TNTs-CTAC can be attributed to electrostatic interactions e.g., at pH 4 most of the studied pollutants exist in anionic form according to their pKa, then, they are preferably adsorbed onto TNTs-CTAC. Contrarily, metformin exists mainly in its cationic form (pKa = 12.33) at pH 6, and is; therefore, better adsorbed onto TNTs.

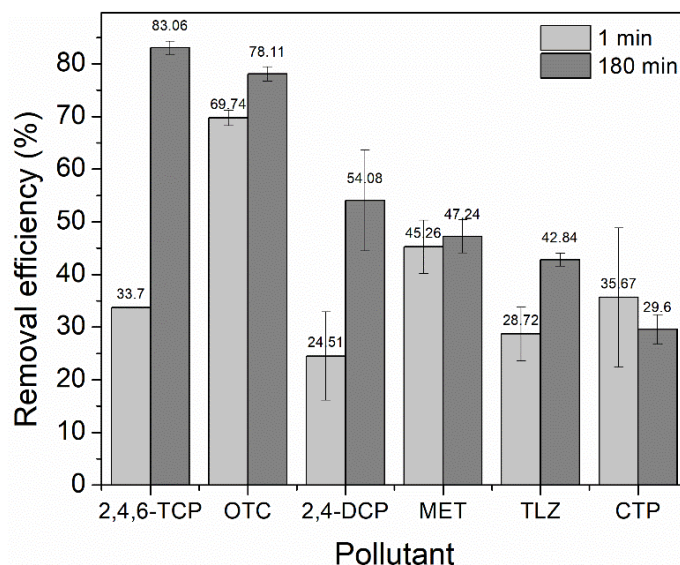


Fig. 7. Removal efficiencies (%) for organic pollutants.

Using equations (4) and (5), the kinetic and equilibrium parameters (q_e , k_1 and k_2) were obtained from the experimental data through non-linear regression analysis. The fit quality was determined through adjusted determination coefficient (R^2_{adj}), average relative error (ARE) and residual analysis. The obtained parameters of the two kinetic models are listed in Table 3.

Table 3. Kinetic parameters for the adsorption of the examined organic pollutants.

Kinetic models	Parameters	TNTs-CTAC					TNTs
		2,4-DCP	2,4,6-TCP	CTP	OTC	TLZ	MET
PFO	k_1 (min^{-1})	1.1123 ± 0.716	2.1225 ± 0.775	1.6831 ± 1.215	0.4541 ± 0.001	1.3677 ± 0.759	1.1009 ± 0.002
	q_e cal. ^a (mg g^{-1})	27.10 ± 2.53	47.18 ± 1.44	17.37 ± 1.35	39.18 ± 0.01	22.93 ± 1.62	28.39 ± 0.01
	R^2_{adj}	0.8687	0.9845	0.8992	0.8707	0.9188	0.7904
	ARE (%)	7.67	2.39	7.43	11.32	5.68	11.12
	k_2 ($\text{g mg}^{-1} \text{min}^{-1}$)	0.0606 ± 0.044	0.1226 ± 0.055	0.1618 ± 0.135	0.0163 ± 0.004	0.1070 ± 0.083	0.6120 ± 2.403
PSO	q_e cal. ^a (mg g^{-1})	28.46 ± 2.17	48.08 ± 1.05	18.05 ± 1.18	41.57 ± 1.69	23.76 ± 1.57	28.33 ± 2.14
	R^2_{adj}	0.9305	0.9933	0.9442	0.9487	0.9440	0.9225
	ARE (%)	6.28	1.80	5.40	6.88	5.85	5.83
	q_e exp. ^b (mg g^{-1})	33.01 ± 0.58	50.20 ± 0.50	18.46 ± 1.81	46.06 ± 1.62	25.80 ± 0.73	29.69 ± 0.13

^a The calculated adsorption capacity at equilibrium.

^b The experimental adsorption capacity measured at equilibrium.

Pseudo-second order kinetic model showed higher values for R^2_{adj} . Furthermore, the calculated adsorption capacities (q_e cal.) for PSO model, were very close to those obtained experimentally, and lower values of average relative error were obtained ($ARE < 7\%$). However, according to these parameters, some pollutants

such as 2,4,6-TCP, TLZ and CTP could also be described for the pseudo-first order kinetic model. To elucidate this, the analysis of the residuals was carried out to complement the study by corroborating the assumptions of normality, equal variance, and independency of the errors throughout the range of data for all the studied pollutants. Then, the goodness of fit of the non-linear regression models was examined. The residual plots support that PSO kinetic model fits better the data, since it was observed that residuals for this model have constant variance, are normally distributed, and are uncorrelated with each other. The residual analysis also provided the lack of fit p-value, considering a significance level of 0.05. For instance, 2,4,6-TCP obtained a p-value of 0.009 and 0.133 for PFO and PSO kinetic model respectively. When the p-value is larger than the significant level, the test does not detect any lack of fit, which was the case of the PSO kinetic model.

Therefore, the pseudo-second order kinetic model (Fig. 8b) is the one that best describes the adsorption process for all the studied pollutants, which suggest that a chemisorption process could have been carried out [32], possibly by the formation of hydrogen bonds between the -OH groups present in the molecular structure of the pollutants (2,4-DCP, 2,4,6-TCP, CTP, and OTC) and the oxygen atoms still present in the surface of the TNTs-CTAC [35]. These results also show that metformin presented the highest adsorption rate ($k_2=0.6120$), which means that the time required to reach the equilibrium was lower for MET than the other pollutants. In contrast, oxytetracycline exhibited the lowest rate ($k_2=0.0163$).

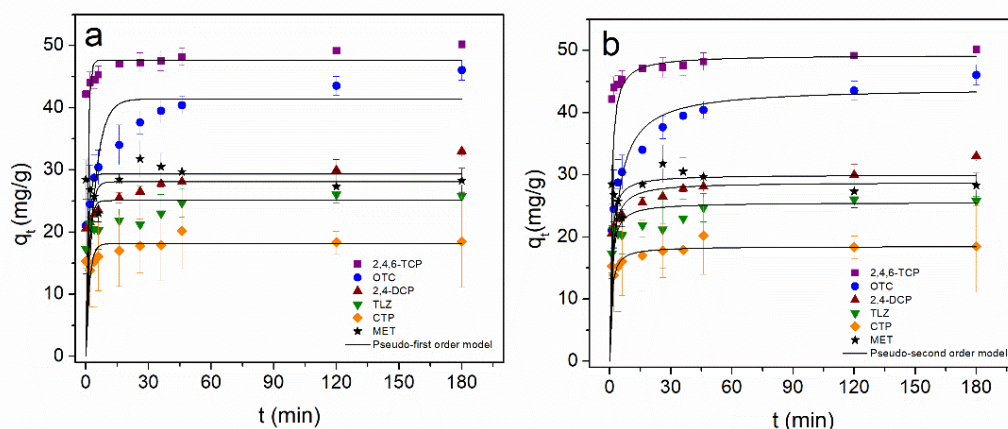


Figure 8. Non-linear pseudo-first (a) and pseudo-second (b) order kinetic plots for the adsorption of OTC, CTP, 2,4-DCP, 2,4,6-TCP and TLZ by TNTs-CTAC, and MET by TNTs. (adsorbent dosage = 0.5 gL⁻¹ and T=27°C).

3.3 Adsorption isotherms for organic pollutants.

The constants for Langmuir and Freundlich isotherm models were calculated from the non-linear regression of experimental data by using the equations (4) and (5) for the Langmuir and Freundlich models respectively. The Freundlich isotherm model is used to describe equilibrium data and adsorption characteristics for a heterogeneous surface assuming that the amount of adsorbate adsorbed increases infinitely with an increase in concentration, whereas Langmuir model assumes monolayer adsorption onto a homogeneous surface [32]. The constants obtained for Langmuir and Freundlich isotherm models are presented in Table 4.

Table 4. Isotherm constants for the adsorption of organic pollutants onto TNTs and TNTs-CTAC.

Isotherm models	Parameters	TNTs-CTAC					TNTs
		2,4-DCP	2,4,6-TCP	CTP	OTC	TLZ	MET
Freundlich	K _F	8.112 ±	29.619 ±	3.667 ±	22.117 ±	13.635 ±	5.946 ±
	(mg g ⁻¹)(mgL ⁻¹) ^{-1/n}	0.360	5.693	0.272	0.013	2.333	0.872
	1/n	0.513	0.272	0.368	0.347	0.206	0.472
	R ² _{adj.}	0.9748	0.9366	0.9882	0.7422	0.8343	0.8784
	ARE (%)	6.63	4.20	1.93	21.26	10.60	9.89
Langmuir	Q _m (mg g ⁻¹)	51.74 ± 2.09	59.85 ± 4.37	21.29 ± 1.33	64.09 ± 5.54	25.27 ± 1.36	35.55 ± 3.72
	K _L (L mg ⁻¹)	0.117 ± 0.011	0.919 ± 0.283	0.097 ± 0.016	0.489 ± 0.127	1.200 ± 0.404	0.110 ± 0.029
	R _L	0.175	0.026	0.203	0.049	0.020	0.184
	R ² _{adj.}	0.9928	0.9137	0.9670	0.9083	0.8098	0.9315
	ARE (%)	2.80	5.62	5.88	13.99	10.25	8.25

Langmuir model had a suitable fit to the adsorption data for 2,4-DCP, 2,4,6-TCP, OTC, TLZ and MET, showing lower values for average relative error (2.5% < ARE < 14%) than those obtained for Freundlich model (1.5% < ARE < 22%), as well as higher values for the adjusted determination coefficient in the case of 2,4-DCP, OTC and MET. Therefore, with a good fit to Langmuir equation, it can be inferred that a monolayer is formed during the adsorption of the organic pollutants onto the adsorbent. Furthermore, it indicates the presence of homogeneous active sites within the adsorbent [32]. In contrast, captopril (CTP) showed a better fit to the Freundlich isotherm model (R²_{adj.} > 0.98, ARE < 2%),

which suggests the formation of a multilayer on a heterogeneous surface during its adsorption process [45]. Langmuir and Freundlich isotherms for studied pollutants are depicted in Fig. 9.

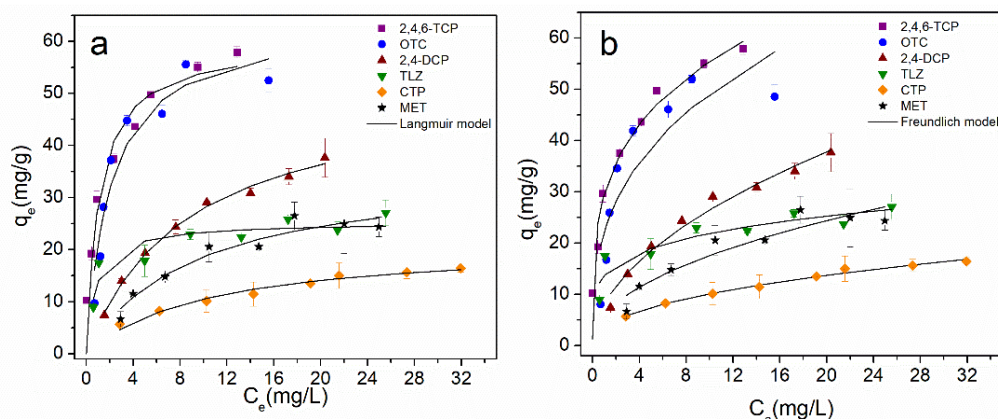


Figure 9. Adsorption isotherms of organic pollutants. a) Langmuir model b) Freundlich model.

As shown in Eq. 10, the dimensionless constant RL of the Langmuir isotherm indicates favorable adsorption for values within $0 < RL < 1$. Thus, all the studied pollutants, obtained a favorable RL value (Table 4).

$$R_L = 1/(1 + K_L C_0) \quad \text{Eq. (10)}$$

To the best of our knowledge, no studies are determining the adsorption processes of these particular pollutants onto any kind of titanate nanotubes. Some references can be found where other titania nanomaterials are used, e.g., Cong S. and Xu Y. [46] reported a maximum adsorption capacity (Q_m) of 5.05 mg g^{-1} for 2,4-DCP onto commercial TiO_2 nanoparticles. In this work, the maximum adsorption capacity for 2,4-DCP by using TNTs-CTAC as adsorbent was up to ten times higher ($Q_m = 51.74 \text{ mg g}^{-1}$).

Chao H. et al. [35] also studied the adsorption of certain phenolic compounds onto modified titanate nanotubes, reporting maximum adsorption capacity of 19.3 , 24.1 , and 32.6 mg g^{-1} for 1-pentanol, m-cresol, and phenol, however, said values are still beneath those obtained in the present study (59.85 mg g^{-1} for 2,4,6-TCP and 51.74 mg g^{-1} for 2,4-DCP).

3.4 Adsorption on groundwater matrices.

Removal efficiencies for most of the organic pollutants in groundwater samples were lower when compared to those in ultra-pure water (Fig. 10). This can be associated with the presence of several dissolved ions in groundwater, which can

interact with the adsorbent, competing for the adsorption sites at the TNTs or TNTs-CTAC surface. This is also reflected in the decrease of the adsorption capacity at equilibrium (q_e) for groundwater tests. Groundwater samples used in this work present a chemical composition mainly influenced by calcite and dolomite. Their concentration of major ions, Na^+ , K^+ , Ca^{2+} , Mg^{2+} , Cl^- , SO_4^{2-} , NO_3^- and HCO_3^- , is also related to water-rock interaction.

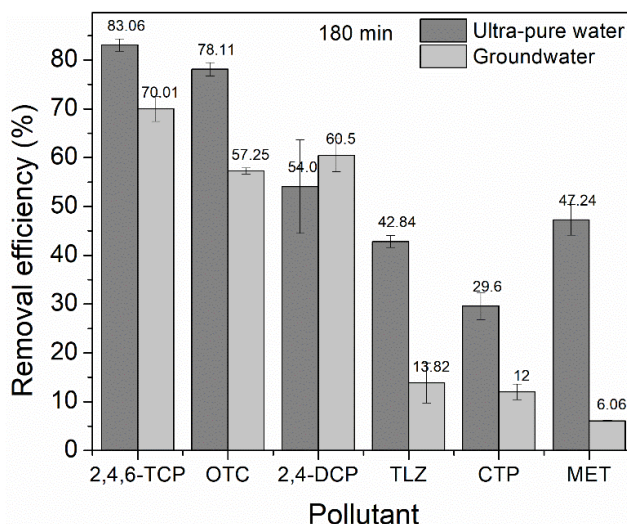


Figure 10. Removal efficiencies of organic pollutants in ultra-pure water and groundwater matrices.

For phenolic compounds and oxytetracycline, the removal efficiency achieved in groundwater samples was similar to the efficiency reached in ultra-pure water, and it was observed that their adsorption capacity (q_e) decreased less than 20% in comparison with ultra-pure water samples. On the other hand, the removal efficiency for the rest of the pollutants (TLZ, CTP, and MET) decreased considerably, as well as their adsorption capacity (>50%), suggesting that anions from groundwater could have been adsorbed at the surface of TNTs-CTAC and TNT-s, decreasing the active sites for adsorption.

The pseudo-first order and pseudo-second order kinetic models were also evaluated, and it was found that the experimental data were good fit to the PSO kinetic model (Fig. 11), with adjusted determination coefficients with higher values than the ones for PFO, as well as lower values of average relative error ($1.5\% < \text{ARE} < 33\%$). This suggests that the pollutants are probably being adsorbed by chemisorption, as they did in the pure water samples. Moreover, the adsorption rate, expressed by K_2 , increased in the groundwater matrices for all the pollutants studied (Table 5), demonstrating that pollutants reach equilibrium in a shorter time than they did in pure water samples.

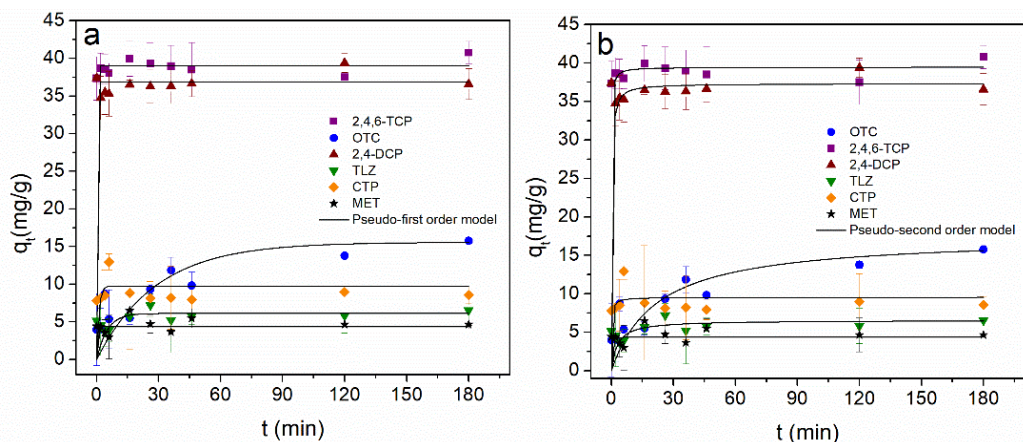


Figure 11. Non-linear pseudo-first (a) and pseudo-second (b) order kinetic plots for the adsorption of OTC, CTP, 2,4-DCP, 2,4,6-TCP, and TLZ by TNTs-CTAC, and MET by TNTs in groundwater. (adsorbent dosage = 0.5 gL^{-1})

Table 5. Non-linear pseudo-first and pseudo-second order kinetic parameters for the adsorption of organic pollutants in groundwater.

Kinetic models	Parameters	TNTs-CTAC					TNTs
		2,4-DCP	2,4,6-TCP	CTP	OTC	TLZ	MET
PFO	k_1 (min^{-1})	1.1009 ± 0.001	1.1009 ± 0.002	1.1010 ± 0.011	0.0669 ± 0.001	1.009 ± 0.011	1.1009 ± 0.013
	$q_{e \text{ cal.}}^a$ (mg g^{-1})	35.97 ± 0.01	38.36 ± 0.01	8.44 ± 0.01	13.04 ± 0.01	5.54 ± 0.01	4.58 ± 0.01
	$R^2_{\text{adj.}}$	0.8180	0.8632	0.6778	0.6280	0.6350	0.5648
	ARE (%)	8.10	7.25	12.54	80.31	15.74	19.30
PSO	k_2 ($\text{g mg}^{-1} \text{ min}^{-1}$)	1.009 ± 0.031	0.5665 ± 0.747	1.1009 ± 0.129	0.0110 ± 0.014	0.4259 ± 0.793	1.1008 ± 0.031
	$q_{e \text{ cal.}}^a$ (mg g^{-1})	36.56 ± 0.01	39.12 ± 0.79	8.97 ± 0.03	13.47 ± 3.56	5.74 ± 0.93	4.66 ± 0.01
	$R^2_{\text{adj.}}$	0.9863	0.9940	0.7590	0.7471	0.7293	0.6494
	ARE (%)	4.52	1.66	8.35	32.14	12.97	13.78
	$q_{e \text{ exp.}}^b$ (mg g^{-1})	36.58	40.78	8.66	15.77	6.52	4.66

^a The calculated adsorption capacity at equilibrium.

^b The experimental adsorption capacity measured at equilibrium.

4. Conclusions

Hydrothermal synthesis and characterization of titanate nanotubes and modified titanate nanotubes were carried out. The characterization of nanomaterial adsorbents showed that the tubular structure was preserved after CTAC modification.

Pseudo-second order kinetic model was found to fit well with the experimental data obtained from both the pure-water and the groundwater experiments for

all the organic pollutants studied. Furthermore, in the adsorption isotherm studies, the Langmuir model had a good fit to the experimental data in pure-water matrices by 2,4,6-TCP, OTC, 2,4-DCP, TLZ, and MET (R^2_{adj} . up to 0.93, ARE<14%), obtaining a maximum adsorption capacity of 59.85, 64.09, 51.74, 25.27 and 35.55 (mg g^{-1}) respectively. Whereas, Captopril obtained a better fit for the Freundlich isotherm (R^2_{adj} . > 0.98 and ARE<1.93%).

Removal efficiency decreased in groundwater matrices, probably due to the presence of other ions interacting with active sites on the nanotubes surface. Nevertheless, removal efficiencies up to 70% were achieved in this complex matrix. It was demonstrated that titanate nanotubes have the potential to be used as adsorbents of persistent organic pollutants in water and specifically groundwater.

To the best of our knowledge, this is the first study addressing the adsorption of 2,4-dichlorophenol, 2,4,6-trichlorophenol, Tolazamide, Metformin, Captopril, and Oxytetracycline onto titanate nanotubes. Moreover, the adsorptive removal of captopril, a highly prescribed drug, is reported for the first time.

Overall, titanate nanotubes present desirable characteristics for adsorption processes such as high surface area and effective ionic exchange properties, among others. In addition, its precursor (TiO_2) is a non-toxic material that can be easily produced on a large scale. Therefore, it is worthwhile to continue researching new ways of modifying either the surface or the crystalline structure of the TNTs to achieve a better specificity as well as higher efficiencies in the removal of persistent organic pollutants.

5. References

- [1] T. Aus Der Beek, F.A. Weber, A. Bergmann, S. Hickmann, I. Ebert, A. Hein, A. Küster, Pharmaceuticals in the environment-Global occurrences and perspectives, *Environ. Toxicol. Chem.* 35 (2016) 823–835. doi:10.1002/etc.3339.
- [2] N.H. Tran, M. Reinhard, K.Y.-H. Gin, Occurrence and fate of emerging contaminants in municipal wastewater treatment plants from different geographical regions-a review, *Water Res.* 133 (2018) 182–207. doi:10.1016/J.WATRES.2017.12.029.
- [3] N. Bolong, A.F. Ismail, M.R. Salim, T. Matsuura, A review of the effects of emerging contaminants in wastewater and options for their removal, *Desalination.* 239 (2009) 229–246. doi:10.1016/j.desal.2008.03.020.
- [4] R. Benson, O.D. Conerly, W. Sander, A.L. Batt, J.S. Boone, E.T. Furlong, S.T. Glassmeyer, D.W. Kolpin, H.E. Mash, K.M. Schenck, J.E. Simmons, Human health screening and public health significance of contaminants of emerging concern detected in public water supplies, *Sci. Total Environ.* 579 (2017) 1643–1648. doi:10.1016/J.SCITOTENV.2016.03.146.
- [5] R. Naidu, V.A. Arias Espana, Y. Liu, J. Jit, Emerging contaminants in the environment: Risk-based analysis for better management, *Chemosphere.* 154 (2016) 350–357. doi:10.1016/j.chemosphere.2016.03.068.
- [6] B. Tiwari, B. Sellamuthu, Y. Ouarda, P. Drogui, R.D. Tyagi, G. Buelna, Review on fate and mechanism of removal of pharmaceutical pollutants from wastewater using biological approach, *Bioresour. Technol.* 224 (2017) 1–12. doi:10.1016/j.biortech.2016.11.042.
- [7] World Health Organization, Guidelines for drinking-water quality. Vol. 2, Health criteria and other supporting information: addendum, *Guidel. Drink. Qual.* 2 (1998). <http://www.who.int/iris/handle/10665/63844>.
- [8] T. Deblonde, C. Cossu-Leguille, P. Hartemann, Emerging pollutants in wastewater: A review of the literature, *Int. J. Hyg. Environ. Health.* 214 (2011) 442–448. doi:10.1016/j.ijheh.2011.08.002.
- [9] L.E. Lesser, A. Mora, C. Moreau, J. Mahlknecht, A. Hernández-Antonio, A.I. Ramírez, H. Barrios-Piña, Survey of 218 organic contaminants in groundwater derived from the world's largest untreated wastewater irrigation system: Mezquital Valley, Mexico, *Chemosphere.* 198 (2018) 510–521. doi:10.1016/j.chemosphere.2018.01.154.

- [10] T.S. Oliveira, M. Murphy, N. Mendola, V. Wong, D. Carlson, L. Waring, Characterization of Pharmaceuticals and Personal Care products in hospital effluent and waste water influent/effluent by direct-injection LC-MS-MS, *Sci. Total Environ.* 518–519 (2015) 459–478. doi:10.1016/j.scitotenv.2015.02.104.
- [11] M. Scheurer, A. Michel, H.-J. Brauch, W. Ruck, F. Sacher, Occurrence and fate of the antidiabetic drug metformin and its metabolite guanylurea in the environment and during drinking water treatment., *Water Res.* 46 (2012) 4790–4802. doi:10.1016/j.watres.2012.06.019.
- [12] R. Salgado, J.P. Noronha, A. Oehmen, G. Carvalho, M.A.M. Reis, Analysis of 65 pharmaceuticals and personal care products in 5 wastewater treatment plants in Portugal using a simplified analytical methodology, *Water Sci. Technol.* 62 (2010) 2862–2871. doi:10.2166/wst.2010.985.
- [13] O. Olujimi, O.S. Fatoki, J.P. Odendaal, Method development for simultaneous determination of phthalate and eleven priority phenols as tert-butyltrimethylsilyl derivatives in grab samples from wastewater treatment plants using GC-MS in Cape Town, South Africa, *Fresenius Environ. Bull.* 20 (2011) 69–77.
- [14] N.H. Tran, H. Chen, M. Reinhard, F. Mao, K.Y.H. Gin, Occurrence and removal of multiple classes of antibiotics and antimicrobial agents in biological wastewater treatment processes, *Water Res.* 104 (2016) 461–472. doi:10.1016/j.watres.2016.08.040.
- [15] J. Rivera-Utrilla, M. Sánchez-Polo, M.Á. Ferro-García, G. Prados-Joya, R. Ocampo-Pérez, Pharmaceuticals as emerging contaminants and their removal from water. A review, *Chemosphere.* 93 (2013) 1268–1287. doi:10.1016/j.chemosphere.2013.07.059.
- [16] Z. Cai, A.D. Dwivedi, W.-N. Lee, X. Zhao, W. Liu, M. Sillanpää, D. Zhao, C.-H. Huang, J. Fu, Application of nanotechnologies for removing pharmaceutically active compounds from water: development and future trends, *Environ. Sci. Nano.* 5 (2018) 27–47. doi:10.1039/C7EN00644F.
- [17] M.B. Ahmed, J.L. Zhou, H.H. Ngo, W. Guo, Adsorptive removal of antibiotics from water and wastewater: Progress and challenges, *Sci. Total Environ.* 532 (2015) 112–126. doi:10.1016/j.scitotenv.2015.05.130.
- [18] O.G. Apul, T. Karanfil, Adsorption of synthetic organic contaminants by carbon nanotubes: A critical review, *Water Res.* 68 (2015) 34–55. doi:10.1016/j.watres.2014.09.032.

- [19] A. Dabrowski, P. Podkoscielny, Z. Hubicki, M. Barczak, Adsorption of phenolic compounds by activated carbon - A critical review, *Chemosphere*. 58 (2005) 1049–1070. doi:10.1016/j.chemosphere.2004.09.067.
- [20] K.-S. Lin, H.-W. Cheng, W.-R. Chen, C.-F. Wu, Synthesis, characterization, and adsorption kinetics of titania nanotubes for basic dye wastewater treatment, *Adsorption*. 16 (2010) 47–56. doi:10.1007/s10450-010-9216-3.
- [21] A.M. Cano, J.D. Maul, M. Saed, S.A. Shah, M.J. Green, J.E. Cañas-Carrell, Bioaccumulation, stress, and swimming impairment in *Daphnia magna* exposed to multiwalled carbon nanotubes, graphene, and graphene oxide, *Environ. Toxicol. Chem.* 36 (2017) 2199–2204. doi:10.1002/etc.3754.
- [22] C.-K. Lee, S.-S. Liu, L.-C. Juang, C.-C. Wang, M.-D. Lyu, S.-H. Hung, Application of titanate nanotubes for dyes adsorptive removal from aqueous solution., *J. Hazard. Mater.* 148 (2007) 756–760. doi:10.1016/j.jhazmat.2007.07.010.
- [23] Y. Zhang, Z. Jiang, J. Huang, L.Y. Lim, W. Li, J. Deng, D. Gong, Y. Tang, Y. Lai, Z. Chen, Titanate and titania nanostructured materials for environmental and energy applications: a review, *R. Soc. Chemistry Adv.* 5 (2015) 79479–79510. doi:10.1039/c5ra11298b.
- [24] L.-C. Juang, C.-K. Lee, C.-C. Wang, S.-H. Hung, M.-D. Lyu, Adsorptive Removal of Acid Red 1 from Aqueous Solution with Surfactant Modified Titanate Nanotubes, *Environ. Eng. Sci.* 25 (2008) 519–528. doi:10.1089/ees.2007.0118.
- [25] C.-K. Lee, L.-H. Lai, S.-S. Liu, F.-C. Huang, H.-P. Chao, Application of titanate nanotubes for ammonium adsorptive removal from aqueous solutions, *J. Taiwan Inst. Chem. Eng.* 45 (2014) 2950–2956. doi:10.1016/j.jtice.2014.08.014.
- [26] C.-K. Lee, S.-S. Liu, H.-C. Chen, Application of hydrothermal method derived titanate nanotubes as adsorbents., *Recent Pat. Nanotechnol.* 3 (2009) 203–212. doi:10.2174/187221009789177786.
- [27] L. Xiong, Y. Yang, J. Mai, W. Sun, C. Zhang, D. Wei, Q. Chen, J. Ni, Adsorption behavior of methylene blue onto titanate nanotubes, *Chem. Eng. J.* 156 (2010) 313–320. doi:10.1016/j.cej.2009.10.023.
- [28] I. Langmuir, The adsorption of gases on plane surfaces of glass, mica and platinum, *J. Am. Chem. Soc.* 40 (1918) 1361–1403. doi:10.1021/ja02242a004.

- [29] H.M.F. Freundlich, *Über die Adsorption in Lösungen*, *Zeitschrift Für Phys. Chemie.* 57U (1907) 385–470. doi:10.1515/zpch-1907-5723.
- [30] S. Lagergren, *About the theory of so-called adsorption of soluble substances*, *K. Sven. Vetenskapsakademiens Handl.* 24 (1898) 1–39.
- [31] G. Blanchard, M. Maunaye, G. Martin, *Removal of heavy metals from waters by means of natural zeolites*, *Water Res.* 18 (1984) 1501–1507.
- [32] A. Bonilla-Petriciolet, D.I. Mendoza-Castillo, H.E. Reynel-Avila, *Adsorption Processes for Water Treatment and Purification*, Springer, Aguascalientes, Mexico, 2017. doi:10.1007/978-3-319-58136-1.
- [33] M.I. El-Khaiary, G.F. Malash, *Common data analysis errors in batch adsorption studies*, *Hydrometallurgy.* 105 (2011) 314–320. doi:10.1016/j.hydromet.2010.11.005.
- [34] D. V. Bavykin, J.M. Friedrich, F.C. Walsh, *Protonated titanates and TiO₂ nanostructured materials: Synthesis, properties, and applications*, *Adv. Mater.* 18 (2006) 2807–2824. doi:10.1002/adma.200502696.
- [35] H. Chao, C. Lee, L. Juang, Y. Han, *Sorption of Organic Compounds, Oxyanions, and Heavy Metal Ions on Surfactant Modified Titanate Nanotubes*, *Ind. Eng. Chemistry Res.* 52 (2013) 9843–9850.
- [36] C.-K. Lee, K.-S. Lin, C.-F. Wu, M.-D. Lyu, C.-C. Lo, *Effects of synthesis temperature on the microstructures and basic dyes adsorption of titanate nanotubes.*, *J. Hazard. Mater.* 150 (2007) 494–503. doi:10.1016/j.jhazmat.2007.04.129.
- [37] N. Liu, X. Chen, J. Zhang, J.W. Schwank, *A review on TiO₂ -based nanotubes synthesized via hydrothermal method: Formation mechanism, structure modification, and photocatalytic applications*, *Catal. Today.* 225 (2014) 34–51. doi:10.1016/j.cattod.2013.10.090.
- [38] L.-C. Juang, C.-K. Lee, C.-C. Wang, S.-H. Hung, M.-D. Lyu, *Adsorptive Removal of Acid Red 1 from Aqueous Solution with Surfactant Modified Titanate Nanotubes*, *Environ. Eng. Sci.* 25 (2008) 519–528. doi:10.1089/ees.2007.0118.
- [39] C. Lee, S. Liu, H. Chen, *Application of Hydrothermal Method Derived Titanate Nanotubes as Adsorbents*, *Recent Pat. Nanotechnol.* 3 (2009) 203–212.
- [40] X.-Y. Liu, N.J. Coville, *A Raman Study of Titanate Nanotubes*, *South African J. Chem.* 58 (2005) 110–115. <http://journals.co.za/content/chem/58/1/EJC24357?fromSearch=true>.

- [41] T. Gao, H. Fjellvag, P. Norby, Crystal structures of titanate nanotubes: A Raman scattering study, *Inorg. Chem.* 48 (2009) 1423–1432. doi:10.1021/ic801508k.
- [42] S.J. Kim, Y.U. Yun, H.J. Oh, S.H. Hong, C.A. Roberts, K. Routray, I.E. Wachs, Characterization of Hydrothermally prepared titanate nanotube powders by ambient and in situ Raman spectroscopy, *J. Phys. Chem. Lett.* 1 (2010) 130–135. doi:10.1021/jz900025r.
- [43] K.S.W. Sing, D.H. Everett, R.A.W. Haul, L. Moscou, R.A. Pierotti, J. Rouquerol, T. Siemieniewska, Reporting Physisorption Data for Gas/Solid Systems with Special Reference to the Determination of Surface Area and Porosity., *Pure Appl. Chem.* 57 (1985) 603–619.
- [44] L. Wang, W. Liu, T. Wang, J. Ni, Highly efficient adsorption of Cr(VI) from aqueous solutions by amino-functionalized titanate nanotubes, *Chem. Eng. J.* 225 (2013) 153–163. doi:10.1016/j.cej.2013.03.081.
- [45] H.N. Tran, S.J. You, A. Hosseini-Bandegharai, H.P. Chao, Mistakes and inconsistencies regarding adsorption of contaminants from aqueous solutions: A critical review, *Water Res.* 120 (2017) 88–116. doi:10.1016/j.watres.2017.04.014.
- [46] S. Cong, Y. Xu, Enhanced sorption and photodegradation of chlorophenol over fluoride-loaded TiO₂, *J. Hazard. Mater.* 192 (2011) 485–489. doi:10.1016/j.jhazmat.2011.05.043.

Chapter 3

Bi₂O₃/rGO/Mo_nO_{3n-1} all – solid - state ternary Z-scheme for visible - light driven photocatalytic degradation of bisphenol A and acetaminophen in groundwater

This Chapter has been published as:

R. Rubio-Govea, C. Orona-Návar, S.F. Lugo-Bueno, N. Hernández, J. Mahlknecht, A. García-García, N. Ornelas-Soto, Bi₂O₃/rGO/Mo_nO_{3n-1} all-solid-state ternary Z-scheme for visible-light driven photocatalytic degradation of bisphenol A and acetaminophen in groundwater, *J. Environ. Chem. Eng.* 8 (2020) 104170. doi:10.1016/j.jece.2020.104170.

1. Introduction

Parallel to the fast population growth around the world, there has been rapid industrial development bringing along increasing amounts of industrial and household wastewater containing toxic organic pollutants that persist after most conventional treatments. These pollutants can cause deleterious effects on human health and ecosystems [1,2]. Therefore, special attention has been given to advanced oxidation processes (e.g. Fenton, photo-Fenton, photocatalysis, etc.) as it has been proven that these technologies are able to eliminate persistent pollutants from water that would be impossible to remove through conventional water treatment technologies [3,4].

Particularly, the interest in photocatalytic materials has been growing due to their application in removing environmental pollutants using sunlight [5,6]. Nevertheless, semiconductor oxide photocatalysts generally have a wide band gap, and as a consequence, they are active only under ultraviolet (UV) light illumination, which is about 5% of the solar spectrum [7,8], restricting their industrial application. The most common example is TiO_2 , which has excellent chemical stability, is non-toxic, and has an excellent photocatalytic activity. However, pure TiO_2 only absorbs UV light and has a fast recombination process of photogenerated electron-hole (e^-/h^+) pairs limiting its practical application [9,10].

Consequently, the development of visible light-driven photocatalysts has been a topic of increasing interest among researchers. Recently, bismuth-based photocatalysts, such as Bi_2O_3 , Bi_2S_3 , and BiOX ($X = \text{Cl}, \text{Br}, \text{I}$), have attracted interest because they present narrow band gaps and good photocatalytic activities under visible light [11]. Specifically, Bi_2O_3 have shown interesting electrical and optical properties, making it a promising material in the field of photocatalysis as it has a band gap between 2.6 and 2.9 eV [12,13] and it was recently reported that it is possible to tune its band gap by means of controlled processes resulting in materials with excellent photocatalytic activities [14]. In the same context, MoO_3 is a material with a band gap of 2.9 eV, and also presents good chemical stability, is non-toxic, and has an excellent capacity to adsorb dyes, which is a desirable property in photocatalytic processes. However, its main drawback is the fast recombination time of e^-/h^+ pairs, compromising its applicability in photocatalytic purposes [15,16].

One way to overcome said drawback is by coupling the material with other semiconductors that have a similar band structure to construct Z-scheme junction systems [17–19]. It is known that in this way it is possible to achieve

the promoted charge separation and efficient utilization of charge carriers with high driven forces for photocatalytic redox reactions [20]. Carbon-based materials, such as graphene and graphene oxide have proven to be an efficient component of Z-scheme systems, as they present unique electrical properties that make them suitable as an electron mediator to fabricate Z-scheme junctions [21,22].

Herein, we present for the first time the development of a visible light-driven $\text{Bi}_2\text{O}_3/\text{rGO}/\text{MoO}_3$ (BGM) photocatalytic nanocomposite for the degradation of organic pollutants in aqueous solution. The photocatalytic activity of the composites was evaluated for their ability to degrade Rhodamine B (RhB), a probe molecule, under visible and UV light irradiation. Particularly, we studied the influence of the Bi_2O_3 and rGO ratio in the photocatalytic performance of the samples. Additionally, the BGM composite that showed the best activity towards the degradation of RhB was used in the degradation of Bisphenol A (BPA) and Acetaminophen (AMP) in groundwater samples.

2. Experimental section

2.1 Reagents

Trisodium citrate dihydrate (99 %), bismuth (III) nitrate pentahydrate (99.99 %), ammonium hydroxide (28-30 %), nitric acid (70 %), sulfuric acid (99 %), potassium permanganate (99 %), rhodamine B (95 %), acetaminophen (99 %), bisphenol A (99 %), isopropanol (99 %), ammonium oxalate (98 %) and benzoquinone (99 %) were purchased from Sigma-Aldrich. Hydrogen peroxide (30 %) was purchased from J.T. Baker. N,N-dimethylacetamide (DMAc, 99 %), sodium molybdate dihydrate (99.9 %) and thiourea (99 %) were purchased from Merck. All reagents were of analytical grade and were used without further purification and all solutions were prepared using deionized water (18.2 M Ω cm).

2.2 Synthesis of bismuth (III) oxide (Bi_2O_3)

First, 5.12 mmol of trisodium citrate dihydrate were dissolved in 150 mL of deionized water, then 3 mmol of bismuth (III) nitrate pentahydrate were added into the solution and put into an ultrasonic bath for 10 min. Afterwards, the solution was stirred for 2 h, the pH was adjusted to 9 with ammonium hydroxide and was left under constant stirring for another 2 h. Finally, the solution was transferred to a Teflon-lined autoclave and was put into an oven at 180 °C for 24 h. Subsequently, the solution was filtered and washed with deionized water and anhydrous ethanol, and the precipitate was dried in a vacuum desiccator overnight. After drying, the powder was heated at 360° C for 3 h, with a

temperature ramp of 5° C/min in order to obtain the monoclinic phase of Bi₂O₃ [14,23]. Then, the sample was cooled down at room temperature.

2.3 Synthesis of graphene oxide (GO)

Graphene oxide was synthesized through a modified Hummer method. Briefly, 2 g of graphite were added to a mixture of sulfuric acid/nitric acid (3:1 v:v) and was put in an ultrasonic bath for 1.5 h. Then 0.05 mol of potassium permanganate were added to the solution, the temperature was raised to 40° C and stirred for 2.5 h. Afterwards, deionized water was added, the temperature was raised to 90° C and left under magnetic stirring for 24 h. Finally, more water was added and then a certain amount of hydrogen peroxide was added into the mixture until the color of the solution turned from dark brown to light brown. Then, the solution was washed with deionized water until a neutral pH was obtained. Once the solution was neutral, the sample was freeze-dried.

2.4 Synthesis of Bi₂O₃/rGO/MoO₃ (BGM) composite

Different amounts of GO were dissolved in 30 mL of deionized water in order to achieve different Bi₂O₃:GO weight ratios (100:1, 200:1, 300:1 and 400:1), where the amount of Bi₂O₃ was fixed at 300 mg. Once GO was completely dissolved, the solution was mixed with 30 mL of DMAc and put into a 3-necked flask under constant stirring until a homogeneous solution was obtained. In a separate beaker, 0.062 mmol of sodium molybdate dihydrate (Na₂MoO₄·2H₂O) and 0.063 mmol of thiourea were dissolved in 5 mL of deionized water; after a homogeneous solution was obtained, it was added dropwise into the GO/DMAc solution and kept under constant stirring for 10 min. Then, Bi₂O₃ was added into the solution and stirred for 5 min, followed by ultrasonication for 5 min. Next, the 3-necked flask was put into a preheated oil bath at 150° C and was left under reflux and constant stirring for 10 h. The solution was left to cool down naturally, and after that, it was filtered and washed with deionized water and absolute ethanol. Finally, the precipitate was left to dry in a vacuum desiccator at room temperature. The obtained composites were labeled as BGM 100:1, 200:1, 300:1, and 400:1 according to the Bi₂O₃:GO weight ratio used.

2.5 Characterization of Bi₂O₃ and BGM

Morphology of the BGM composite was studied using a Scanning Electron Microscope (Nova NanoSEM 200) with an acceleration voltage of 15 kV, and a Transmission Electron Microscope (JEM-2200FS+CS) with spherical aberration correctors operated at 200 kV. X-ray diffraction patterns recorded from 20° to 80° were obtained by an Empyrean (PANalytical, USA) X-ray diffractometer

using Cu-K α radiation ($\lambda = 1.5406 \text{ \AA}$). X-ray photoelectron spectroscopy (XPS) analysis was performed on an ESCALAB 250Xi (Thermo Scientific, USA) X-ray photoelectron spectroscope using monochromatic AlK α radiation ($h\nu = 1486.7 \text{ eV}$). Deconvolution of the XPS spectra was done with the AAnalyzer 1.20 software, performing a Voigt peak fit and a Shirley-Sherwood background subtraction; all binding energies for elements of interest were calibrated with reference to adventitious carbon (C1s = 284.6 eV).

The optical properties of the powder samples were studied using an Ultraviolet visible Lambda 365 spectrophotometer with an integrating sphere attachment for diffused reflectance (UV-vis-DRS). The scan speed was 1 nm/s using a white standard. Specific surface area and porous structure were characterized by nitrogen adsorption-desorption isotherms using the Autosorb-1 (Quantachrome) at 77 K. Surface area was determined from the Brunauer-Emmett-Teller (BET) equation, and pore size distribution was analyzed by using the Barrett-Joyner-Halenda (BJH) method.

2.6 Photocatalytic activity test

The photocatalytic activities of Bi₂O₃ and BGM composites were evaluated by degradation of Rhodamine B (RhB) under visible (λ from 390-600 nm) and UV (λ from 300-380 nm) light irradiation. The photocatalytic system included a 300 W Xe light source (MAX-303, Asahi Spectra) with an illumination area of 16x16 mm. The nominal power of the lamp was used without attenuation (100% power). In a typical photocatalytic experiment, 40 mg of the photocatalyst were dispersed in 80 mL of a 10 mg/L RhB solution and put into an ultrasonic bath for 2 min. Before irradiation, the suspension was magnetically stirred in the dark for 30 min to complete the adsorption-desorption equilibrium between the photocatalyst and the dye. Then, the solution was exposed to either visible or UV light irradiation under magnetic stirring. For degradation analysis, 0.5 ml aliquots of the suspension were removed from the reaction at given time intervals during the process and centrifuged at 13,500 rpm for 5 min. Then the UV-vis spectra of the centrifuged solution were recorded. All photodegradation experiments were carried out at 25° C.

Reusability tests were carried out using the same experimental conditions of the photocatalytic experiments under visible light irradiation. After photocatalytic treatment, the composite BGM(300:1) was recovered by filtration, washed several times with a maximum of 30 mL of water and 25 mL of ethanol, and dried overnight. Then, the recovered dry powder was used in a new catalytic cycle. The solution volume was adjusted each cycle in order to maintain the

same composite concentration. The process was repeated for 6 consecutive cycles and the last cycle was carried out with the minimal working volume (50mL).

2.7 Active species trapping experiments

To determine the active species involved in the photocatalytic degradation of organic pollutants, radical scavenger experiments were conducted. The experiments were carried out similarly to the photocatalytic activity test, but isopropanol (IPA), ammonium oxalate (AOx), and benzoquinone (BQ) were used as hydroxyl radical ($\cdot\text{OH}$), holes (h^+) and superoxide free radical ($\cdot\text{O}_2^-$) scavenger agents, respectively. The concentration of the scavenger used was 1 mM.

2.8 Photocatalytic activity in groundwater samples

The photocatalytic activity of BGM towards BPA and AMP was determined using groundwater (GW) samples as a real matrix. The GW samples were obtained from several aquifers located in Nuevo Leon, a state located in northeastern Mexico. The pH in GW samples varied between 6.77 and 7.88, indicating neutral to slightly alkaline water conditions within the studied area. Prior to the photocatalytic tests, GW samples were filtered with 0.45 μm regenerated cellulose membrane filters. The photocatalytic activity tests were carried out following the methodology mentioned in Section 2.6, substituting ultra-pure water for GW and using BPA and AMP in concentrations of 10 mg/L instead of RhB. For the degradation of BPA and AMP, 0.5 mL aliquots were withdrawn from the reaction solution at different time intervals and centrifuged at 13,500 rpm. The supernatant was filtered with a 0.2 μm regenerated cellulose syringe filter and analyzed by high-performance liquid chromatography (HPLC). Chromatographic analysis was carried out with a ZORBAX Eclipse XDB C18 (150mmx4.6mm, 5 μ) column using an Agilent 1200 series with a UV visible detector. Chromatographic conditions used for the detection are listed in Table 1.

Table 1. HPLC parameter for analysis of Bisphenol A and acetaminophen.

	Bisphenol A	Acetaminophen
Eluents	A: Acetonitrile B: Phosphate buffer 10 mM pH 3.5	A: Acetonitrile B: Phosphate buffer 25 mM pH 3
Elution mode	Gradient 0 min: 5% A, 95% B	Gradient 0 min: 10% A, 90% B

	2 min: 35% A, 65% B	8 min: 90% A, 10% B
	12.5 min: 70% A, 30% B	12 min: 10% A, 90% B
	18 min: 5% A, 95% B	
Analysis conditions	Flux: 1 ml/min	Flux: 1 ml/min
	Time: 23 min	Time: 12 min
	Injection: 20 μ L	Injection: 20 μ L
	$\lambda = 230$ nm	$\lambda = 230$ nm

3. Results and discussion

3.1 Characterization of the as-prepared materials

The SEM and STEM images of the BGM(300:1) are shown in Figure 1 (a, b), respectively. As observed in Figure 1a, the composite material does not have a defined morphology and varies in sizes between 1 and 4 μ m. In addition, a Bi_2O_3 core is observed surrounded by rGO sheets, as the ripples in the surface of the composite can only be formed by incorporating rGO. This becomes more evident via STEM analysis (Figure 1b), where the rGO sheets are surrounding the Bi_2O_3 particles (dark spots). This is a desirable feature in a Z-scheme system since the rGO sheets need to be in contact with the two metal oxides to have effective electron percolation. See supplementary material S3 for a detailed scheme of the crystal structure rearrangement.

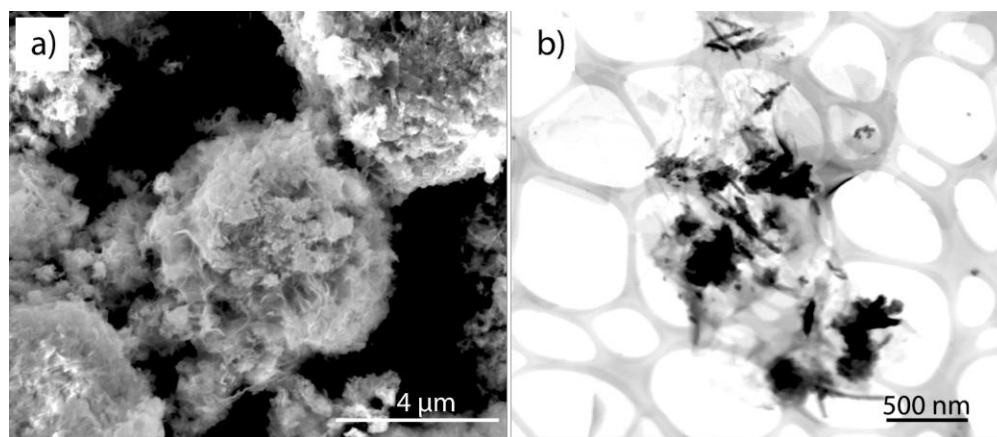


Figure 1. a) SEM and b) STEM representative images of the as-prepared BGM(300:1) composite.

Figure 2 shows a TEM image of the BGM(300:1) composite, where the analyzed zone is composed of two different crystal structures corresponding to monoclinic Bi_2O_3 and a Mo_xO_y non-stoichiometric phase. The presence of a Mo_xO_y non-

stoichiometric phase can be explained by the distortion of the MoO_3 phase by the removal of oxygen anions creating vacancies, causing the crystal to reorder by crystallographic shear planes [24,25]. The best-known crystal shear structures are called the Magnéli phases $(\text{Mo}, \text{W})\text{nO}_{3n-1}$ ($n= 8, 9, 10, 11, 12, 13, 14$) where the shear planes are regularly spaced [24]. The molybdenum oxide structures consist of MoO_6 octahedra as their basic crystal structural unit and it has been noted that upon the removal of oxygen anions, this unit undergoes considerable structural rearrangements. One of the ways in which its structure can accommodate these rearrangements is via crystallographic shear defects. In such a case, the planes of anion vacancies are eliminated by the formation of shear from corner edge-sharing of octahedra and the crystal collapse of the oxide, generating extended crystal shear plane defects [26].

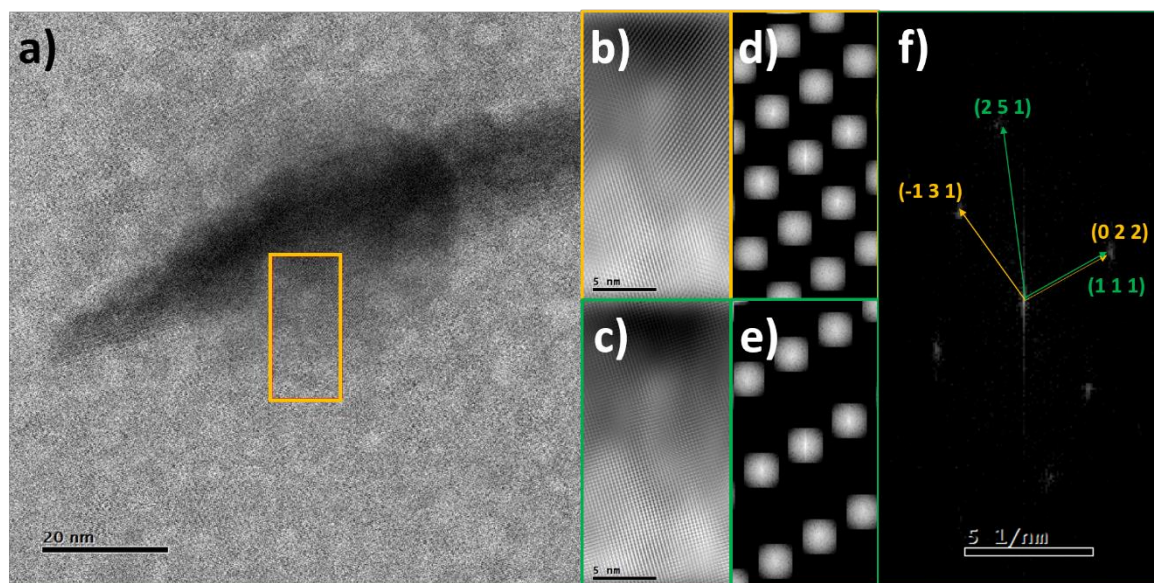


Figure 2. TEM image of the BGM(300:1) composite showing two different crystal structures corresponding to Bi_2O_3 (yellow) and $\text{Mo}_n\text{O}_{3n-1}$ (green) phases. The Fourier Transform Function was used to obtain atomic arrangements.

Figure 3 shows the XRD patterns of a) Bi_2O_3 and b) BGM(300:1). The Bi_2O_3 material shows well-defined peaks and high crystallinity (Figure 3a). Pattern matching was performed using the PDF card 01-071-0465 for Bi_2O_3 with spatial group P21/c (14). The obtained cell parameters are $a= 5.849 \text{ \AA}$, $b= 8.164 \text{ \AA}$, $c= 7.510 \text{ \AA}$, $\alpha = \gamma = 90^\circ$ and $\beta = 112.97^\circ$, corresponding to a monoclinic crystal structure. The pattern from Figure 3b can be indexed to spatial group P21/c (14), ascribed to monoclinic Bi_2O_3 , and spatial group C2/c (PDF card 01-084-1466). Calculated cell parameters were: $a= 29.194 \text{ \AA}$, $b= 8.083 \text{ \AA}$, $c= 16.816 \text{ \AA}$, $\alpha = \gamma = 90^\circ$,

and $\beta = 95.47^\circ$ which correspond to monoclinic Mo_9O_{26} that is a MoO_3 phase with oxygen vacancies ($\text{MoO}_{2.88}$) consistent with the so-called Magnéli phase $\text{Mo}_n\text{O}_{3n-1}$ [27,28]. This is in agreement with the results obtained by TEM.

The observed and calculated XRD data, as well as the difference between those profiles, were obtained by pattern matching analysis. Lattice parameters, unit cell volume, and the goodness of fitting parameter (χ^2) are listed in Table 2. The fit between observed and calculated profiles was found to be relatively good, which confirms the structural stability. Also, the crystallite size of the synthesized materials were calculated by using the Scherrer equation, $t = K\lambda/B\cos k$, where λ is the X-ray wavelength (\AA), B is the full width at half maximum, k is Bragg angle, K is a factor depending on crystallite shape and t is the crystallite size (\AA).

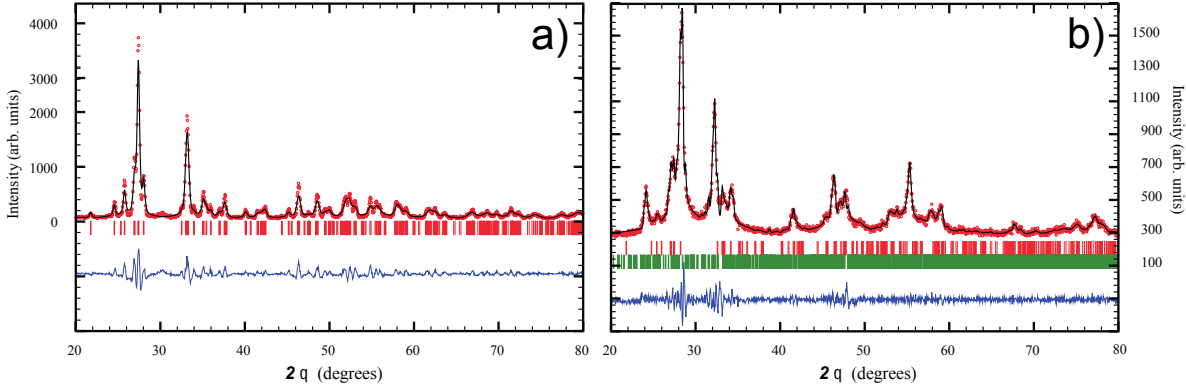


Figure 3. a) Pattern matching from X-Ray diffraction data of the as-obtained Bi_2O_3 and b) BGM(300:1). Experimental data (Red dots), calculated for Bi_2O_3 in (a), and for Bi_2O_3 and Mo_9O_{26} in (b) (Black continuous line). Differences (Blue line), Bragg positions of $\text{P}2_1/\text{c}$ structure (Red lines), and Bragg positions of $\text{C}2/\text{c}$ structure (Green lines).

Table 2. XRD data obtained by pattern matching analysis for pure Bi_2O_3 and composite BGM(300:1). Lattice parameters, unit cell volume of $\text{P}2_1/\text{c}$ and $\text{C}2/\text{c}$ phases, crystallite size, and the goodness of fitting parameter (χ^2).

Material	Spatial group	a (\AA)	b (\AA)	c (\AA)	V (\AA^3)	α ($^\circ$)	β ($^\circ$)	γ ($^\circ$)	χ^2
Pure Bi_2O_3	$\text{P}2_1/\text{c}$	5.849	8.164	7.510	330.57	90.0	112.9	90.0	8.4
					7	0	7	0	0
BGM (300:1)	$\text{P}2_1/\text{c}$	5.837	8.158	7.446	326.89	90.0	112.9	90.0	1.4
	$\text{C}2/\text{c}$	29.194	8.083	16.81	3915.6	90.0	95.47	90.0	6
				6	95	0		0	

To further investigate the chemical nature of the BGM(300:1) composite, X-ray photoelectron spectroscopy (XPS) analysis was performed. Figure 4a shows the corresponding C1s XPS spectra of pristine GO, where the binding energies (B.E.) of 284.6, 285.64, 287.57, 288.57, and 289.42 eV correspond to C-C/C=C, C-O, C-OH, C=O, and HO-C=O respectively [29,30]. Figure 4b shows the corresponding C1s B.E. found in BGM(300:1), where it can be observed that the intensity of the B.E. corresponding to the C-C/C=C bonds increased (284.6 eV), while the B.E. of C-O (285.96 eV) and C-OH (287.61 eV) significantly decreased; also the intensity of carbonyl groups (288.11 eV) is increased with respect to the carboxylic groups (289.1 eV) indicating that GO was partially reduced during BGM(300:1) synthesis. Additionally, we see the appearance of a small peak with B.E. of 283.76 eV which can be attributed to the formation of C-Bi bonds [31], indicating that the Bi₂O₃ particles are being chemically functionalized by the rGO sheets. This reduction process is favorable for the fabrication of a Z-scheme system because the sp² hybridization of carbon bonds is partially restored and the percolation process is enhanced. As a consequence, the separation between e⁻/h⁺ pairs is promoted, thus optimizing the photocatalytic process [32].

The degree of GO reduction was monitored by obtaining the oxygen-bound carbon content, which can be calculated using equation 1, where AC-C, AC-O, and AC=O are the peak areas for graphitic (C-C) and O-bound (C-O and C=O) carbon, respectively [33]:

$$\%O_{bound} C = \frac{A_{C-o} + A_{C=o}}{A_{C=c} + A_{C-o} + A_{C=o}} \times 100 \quad (1)$$

The O-bound carbon percentage in pristine GO was of 87.56%, and the O-bound carbon percentage in BGM(300:1) was of 61.25%. These results corroborate that GO was partially reduced during the synthesis of BGM(300:1).

Figure 4c shows the corresponding Bi4f XPS spectra, which was deconvoluted into two pairs of doublets. The B.E. at 158.83 and 164.13 eV correspond to Bi4f_{7/2} and Bi4f_{5/2}, respectively, assigned to Bi(III) present in Bi₂O₃. The small peaks with B.E. at 159.68 and 164.93 eV can be ascribed to the Bi(V) center formed from the decomposition of Bi₂O₂CO₃ during the calcination process. It has been suggested [34,35] that during the annealing process Bi₂O₂CO₃ reacts with O₂, partially oxidizing some of the Bi(III) centers to Bi(V) as indicated by equation 2:

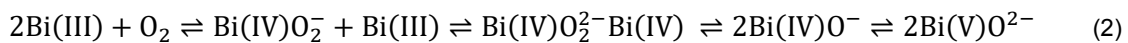


Figure 4d shows the corresponding Mo3d XPS spectra. The B.E. at 231.78 and 234.88 eV are assigned to Mo3d_{5/2} and Mo3d_{3/2} present in Mo⁵⁺ oxidation state [36,37]. It's worth noting that the intensity of the deconvoluted Mo_{3d}_{5/2} and Mo_{3d}_{3/2} doublets satisfies the theoretical ratios of their corresponding spin-orbit splitting (3:2). The presence of Mo⁵⁺ valence states corroborates the results obtained by XRD, in which the phase obtained for the molybdenum oxide is MoO_{2.88} having oxygen vacancies. The Mo⁵⁺ is attributed to oxides that have the presence of oxygen vacancies with a single positive charge [38].

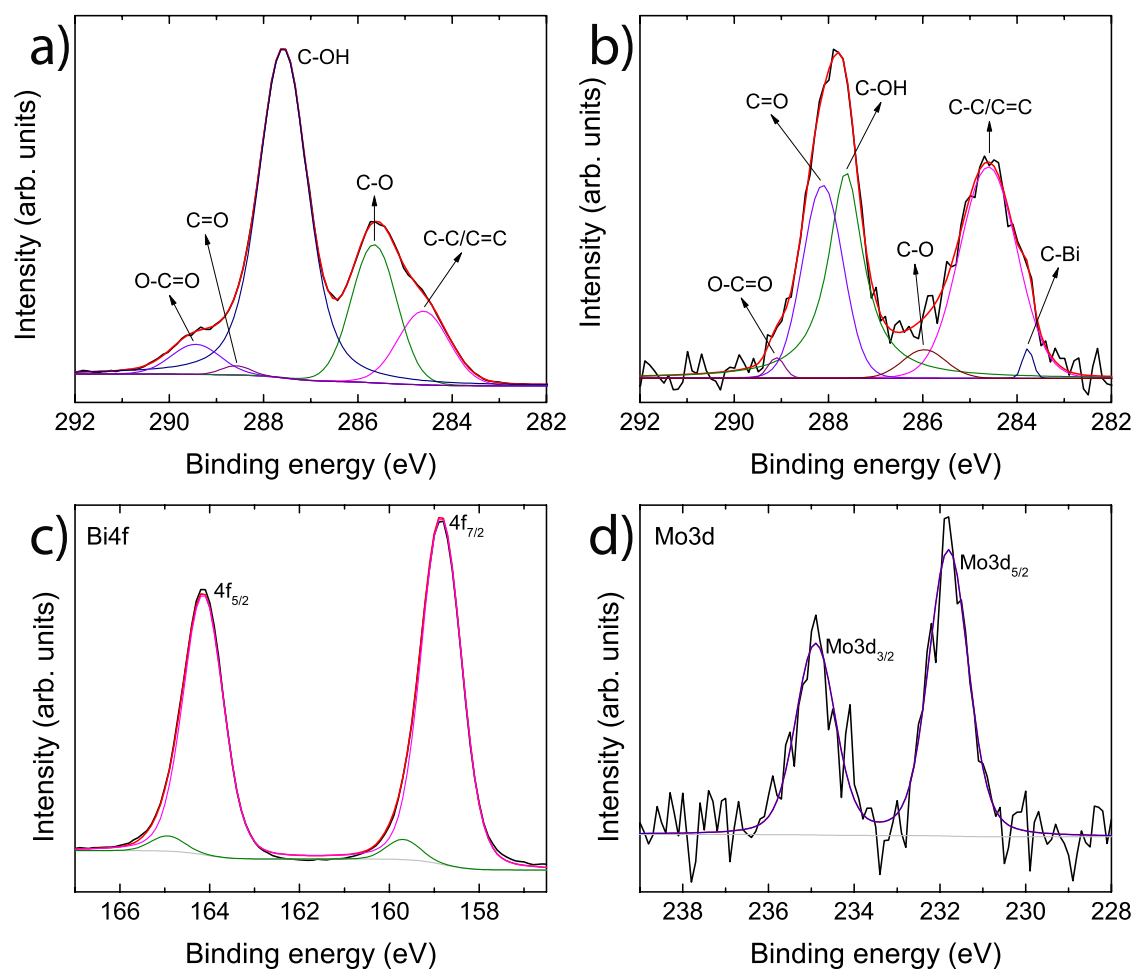


Figure 4. XPS spectra of GO and BGM(300:1). Results of a) the C1s spectra fitting into C chemical groups present in pristine GO, b) results of the C1s spectra fitting into C chemical groups from BGM(300:1), c) the Bi4f spectra fitting into Bi chemical groups and d) results of the Mo3d spectra fitting into Mo chemical groups from BGM(300:1).

Diffuse reflectance spectra and Kubelka-Munk graphs for Bi₂O₃ and BGM(300:1) at room temperature are presented in Figure 5 (a, b), respectively. Generally,

the zone comprised of 700-800 nm, is a straight line representing the incident light that passes through the sample, this region is called transmission or optical transmittance. As can be seen in Figure 5a, this region or straight line, in 450 nm for Bi₂O₃ and approximately 425 nm for BGM(300:1), a fast and abrupt ascent is observed, associated with the electron transition of the valence band to the conduction band. This means that, up to 450 nm, absorption occurs. If the Kubelka-Munk function and equations 3 and 4 are applied to the graph, the absorbance versus the wavelength graph can be obtained.

$$FKM = F(R_{\infty}) = (1 - R_{\infty})^2 / 2R_{\infty} = k/s \quad (3)$$

$$R_{\infty} = R_{\infty(\text{sample})} / R_{\infty(\text{standard})} \quad (4)$$

Where $F(R_{\infty})$ is a remission function. FKM (Kubelk-Munk Function) is known as the remission function of Kubelka-Munk, R_{∞} is the reflectance of the infinitely thick layer and k and s are the absorption and dispersion constant, respectively. This function of the diffuse reflectance for optically coarse samples keeps a linear dependence with the absorption coefficient of the material. The Kubelka-Munk function is calculated from the absorption data measured by diffuse reflectance and allows us to estimate the value of the band gap of a sample.

To calculate the band gap value E_g , the Kubelka-Munk remission function was plotted by the photon energy squared for the Y-axis and the energy of the incident light in eV for the X-axis as shown in Figure 5 b. The band gap energy was obtained by extrapolating the linear part of the graph of the Kubelka-Munk function to the abscissa axis (photon energy); results are shown in Table 3.

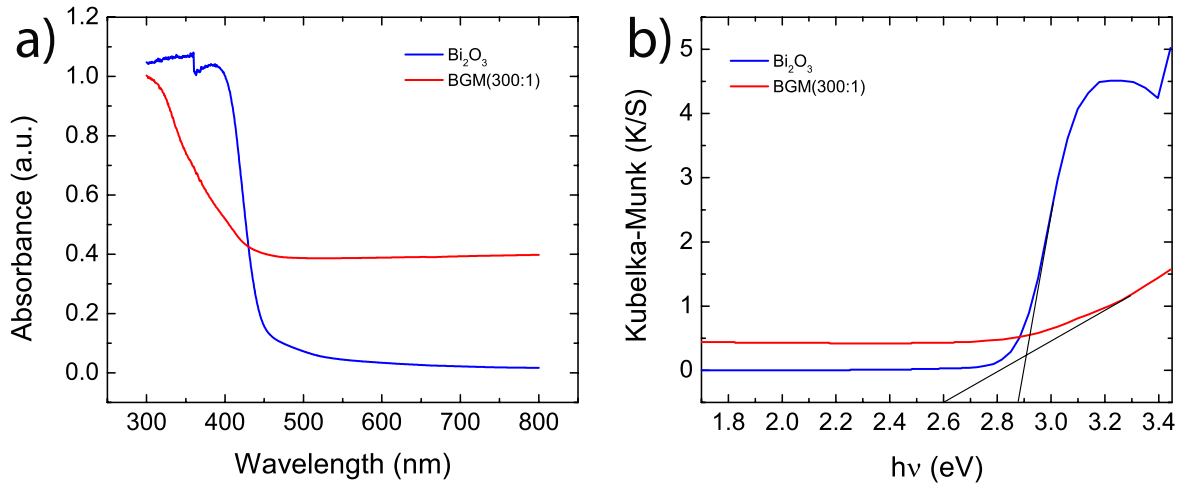


Figure 5. a) UV-Vis diffuse reflectance spectroscopy of Bi₂O₃ and BGM(300:1); b) Kubelka-Munk plot of Bi₂O₃ and BGM(300:1).

Table 3. Energy band gap obtained by DRS for Bi₂O₃ and BGM(300:1).

Material	Band Gap (eV)
Bi ₂ O ₃	2.88
BGM(300:1)	2.6

N₂ adsorption-desorption isotherms were used to determine the specific surface area (SBET) of pristine Bi₂O₃ and BGM(300:1). The obtained SBET for Bi₂O₃ is of 4.31 m²/g, with an average pore diameter of 152 nm. In the case of BGM(300:1), the obtained SBET is 11.15 m²/g with an average pore diameter of 167 nm. Upon the addition of rGO, the surface area of BGM(300:1) was greatly increased, which is expected to influence the composite performance. The adsorption-desorption isotherms of Bi₂O₃ and BGM(300:1) shown in Figure 6 exhibited a type III isotherm [39] which is associated with the formation of slit-shaped pores in the aggregates of the nano or microparticles [40]. Furthermore, the presence of macropores (>50 nm) can be confirmed by the absence of an adsorption plateau at relative pressure near unity [41].

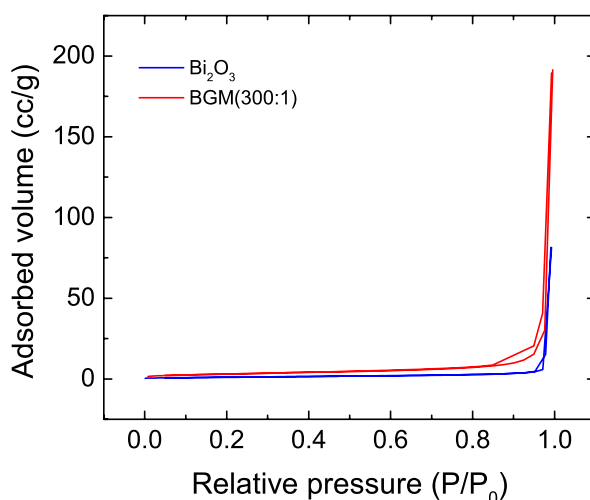


Figure 6. N₂ adsorption-desorption isotherms of Bi₂O₃ (blue) and BGM(300:1) (red).

3.2 Photocatalytic activity tests

In order to determine the effect of different Bi₂O₃:rGO weight ratios on the photocatalytic activity, degradation of RhB under visible and UV light was carried out with the different composites. Figure 7a shows the degradation of RhB under visible light, where the best photocatalytic activity was achieved with

the BGM(300:1) composite, which was able to degrade 70% of the initial concentration after 260 min of irradiation. It is also important to note that the degradation efficiency of the composites tended to increase when the Bi_2O_3 :rGO ratios decreased. This may be attributed to the increased average distance between Bi_2O_3 and MoO_3 at high rGO concentrations (ratios of 100:1 and 200:1), which hinders the percolation of photogenerated electrons between the two materials, consequently affecting the photocatalytic activity.

In a study conducted by Gao et al. [42], it was suggested that the functional groups present in GO could act as an anchoring point for the molybdenum precursor used to synthesize MoS_2 quantum dots. Although this cannot be corroborated in this study due to the low concentration ratios used for BGM synthesis, the approach of Gao et al. [42] could help to understand the interaction between the components in BGM. Accordingly, if the amount of GO used is too high, contact between the three constituents of the composite may not be suitable to generate an effective Z-scheme. In that case, the overall photocatalytic activity would be hindered. In the same context, if the ratio between Bi_2O_3 and rGO is too small, as it is for the synthesized composite BGM(400:1), there will probably not be enough anchoring sites due to the low concentration of rGO. This would affect the growth of MoO_3 nanoparticles, which would also affect the photocatalytic activity of the compound.

Figure 7b shows the degradation of RhB under UV light irradiation. It is observed that the photocatalytic activities of the composites are enhanced when the Bi_2O_3 and rGO ratios are low. In this case, the BGM(300:1) and BGM(400:1) composites were able to completely degrade RhB after 120 min of irradiation.

In order to determine the importance of each constituent of the composite, photocatalytic experiments were conducted including only two components instead of three. The synthesis was carried out similarly to the BGM composites but excluding one of the precursors (GO or $\text{Na}_2\text{MoO}_4 \cdot 2\text{H}_2\text{O}$) from the reaction. As can be seen in Figure 7c for the photocatalytic degradation of RhB under visible light, the best performance was achieved with composite BGM(300:1), followed by the composite where only rGO was added. From these results it can be concluded that the addition of rGO helps to delay the recombination time of photogenerated e^-/h^+ pairs, enhancing the photocatalytic activity of Bi_2O_3 . Another important feature of rGO is the enhanced RhB adsorption during the dark stirring stage, resulting in better contact between RhB molecules and the surface of the composites. Similar behaviors, where the rate of recombination of

e^-/h^+ pairs is decreased, have been observed when Bi_2O_3 nanoparticles are doped with $\text{Ce}^{3+}/\text{Ce}^{4+}$, resulting in enhanced photocatalytic activity of the material [43].

In the case of UV light irradiation, the removal of one constituent of the composite did not cause a negative effect in the photocatalytic activity. As observed in Figure 7d, all composites were able to completely degrade RhB after 120 min of irradiation. This can be attributed to the higher energy of UV light that promotes the generation of e^-/h^+ pairs, ultimately reflecting in the enhancement of photocatalytic activity. It is important to highlight that although the photocatalytic activity of the composite was slightly higher under UV light than under visible light irradiation, the composite was able to greatly enhance its photocatalytic performance when it is irradiated with visible light, compared to the pristine Bi_2O_3 or $\text{Bi}_2\text{O}_3/\text{rGO}$ material. This is highly valuable since visible-light-driven photocatalysts could be implemented in advanced oxidation processes without the need to use external sources of UV radiation but rather visible light that is readily available from the sun.

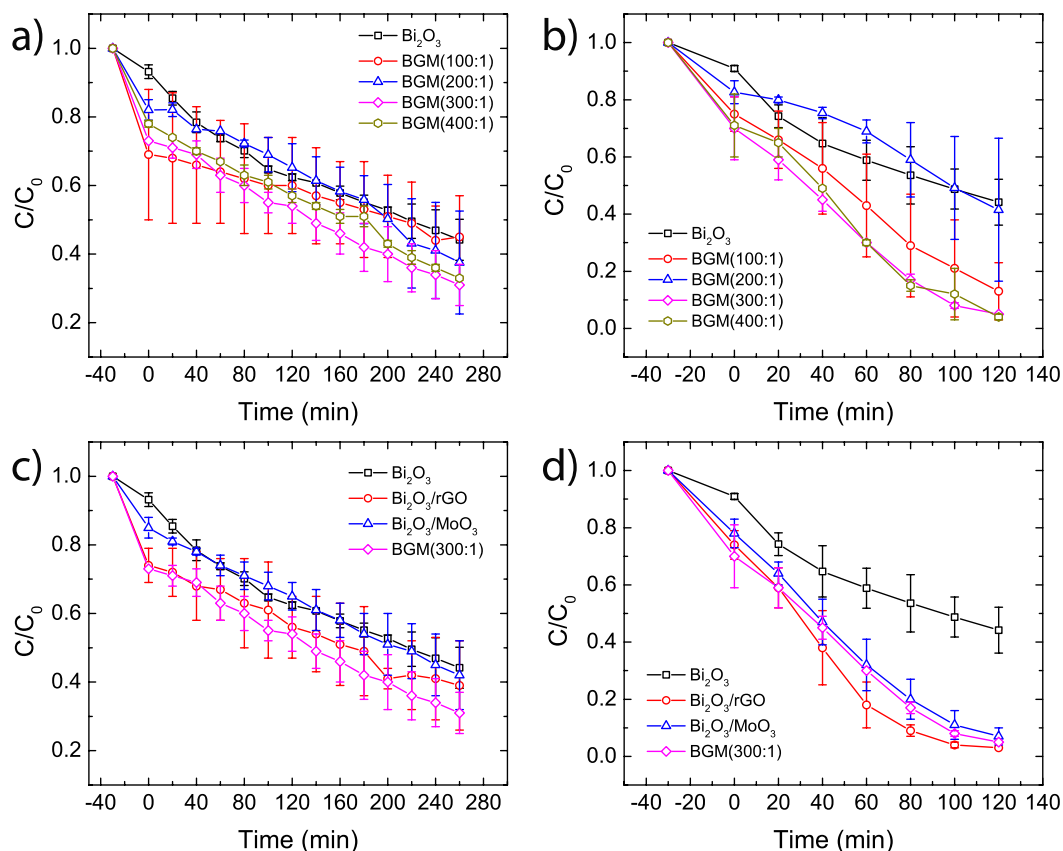


Figure 7. Degradation of RhB with composites BGM(100:1), BGM(200:1), BGM(300:1), BGM(400:1) and Bi_2O_3 under a) visible and b) UV light

irradiation. Degradation of RhB with composites BGM(300:1), Bi₂O₃/rGO, Bi₂O₃/MoO₃, and Bi₂O₃ under c) visible and d) UV light irradiation.

Figure 8 shows the variation of C/C₀ of RhB as a function of visible light irradiation time for the BGM(300:1) composite in the presence of active species scavengers. The role of active species was determined by comparing the C/C₀ variation of a system with the presence of scavengers to the normal system without scavengers. When AOX was added to the system, only 15% of RhB was degraded after 260 min, compared to 75% RhB degradation without the addition of scavengers. When IPA was added, the degradation of RhB was slightly hindered, achieving 65% degradation after 260 min. When BQ was added, the degradation of RhB was suppressed the first 120 min, but afterwards it was slightly enhanced reaching 80% degradation after 260 min.

These results indicate that a large number of h⁺ sites are being generated and that the main degradation mechanism is by direct oxidation of the adsorbed organic molecules by h⁺. Hence, it can be concluded that h⁺ have a greater affinity to react with adsorbed organic molecules rather than with water molecules to produce ·OH radical, as the degradation of RhB in the presence of IPA had little effect and was only reduced by 10%. In the case of RhB degradation in the presence of BQ, at the beginning of irradiation, the BQ molecules captures ·O₂⁻ radicals, hindering RhB degradation. Then, the observed increase in catalytic activity after 120 min irradiation could be attributed to the ability of BQ to be reduced by radicals following a one-electron transfer mechanism [44], generating a reactive BQ radical that can later react with RhB molecules promoting its degradation. See supplementary material S4 for the possible mechanism for photogenerated e⁻/h⁺ pairs separation and transport at the interface of the BGM composite.

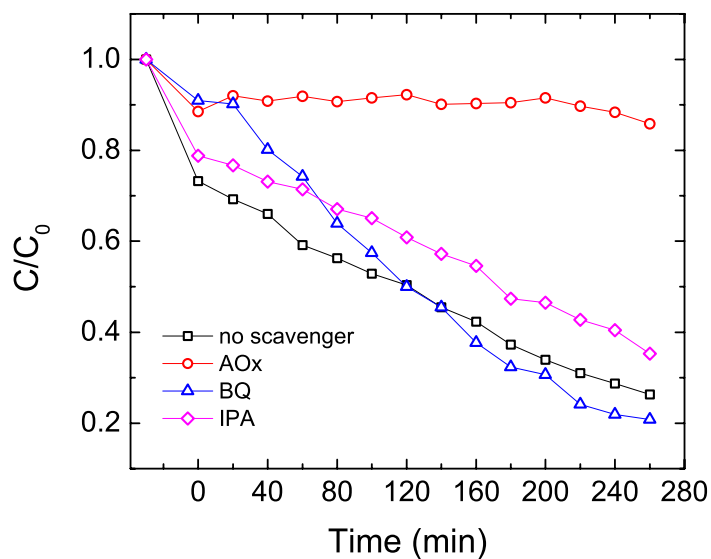


Figure 8. Degradation of RhB by BGM(300:1) composite under visible light irradiation in the presence of AOx, IPA, and BQ as h^+ , $\cdot OH$, and $\cdot O_2^-$ scavengers, respectively.

Stability of the BGM(300:1) composite was investigated through reusability tests in which the photocatalyst was recovered and washed several times to be used in consecutive cycles. The results are shown in Figure 9 and revealed that the composite maintained about 90% of the total efficiency from cycle 2 to 6, which suggests that the composite material remains stable after several photocatalytic cycles. BGM(300:1) stability was corroborated through STEM micrographs (see supplementary material S5). By comparing the micrographs (Figures 1a, 1b and S8) it was observed that the structure and morphology were not modified, and the composite material remained dispersed on the rGO sheets after completing the 6th photocatalytic cycle.

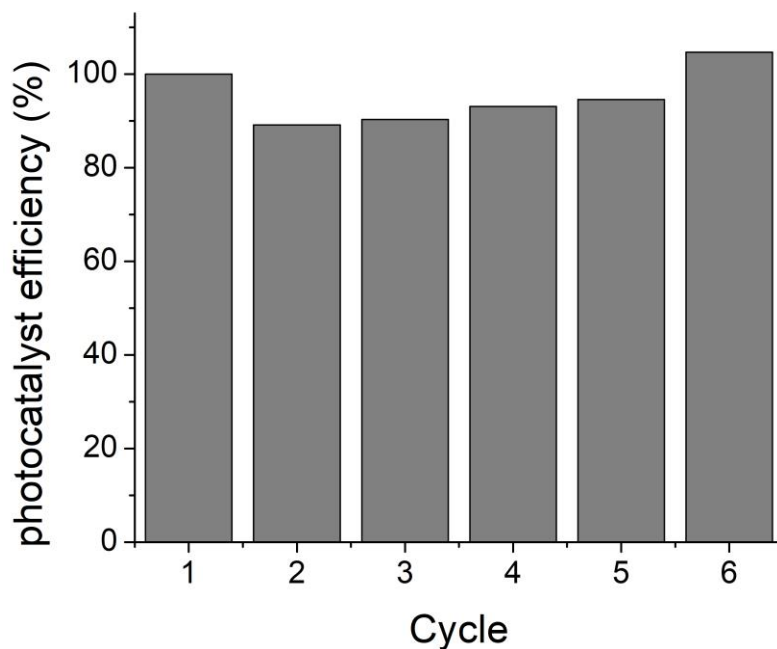


Figure 9. BGM(300:1) reusability test for RhB degradation under Visible light irradiation. (photocatalyst dose 0.5 g/L).

3.3 Photocatalytic degradation of Bisphenol A and Acetaminophen in groundwater

The presence of emerging contaminants in the environment is a major concern due to their adverse effects on wildlife and human health. Bisphenol A (flame retardant) and acetaminophen (pharmaceutical) are considered emerging pollutants and have been detected in both surface water bodies and groundwater [45,46]. Photocatalytic degradation of BPA and AMP under visible light irradiation was studied in pure water as well as in the groundwater matrix.

Figure 10 shows the photocatalytic degradation efficiencies for BPA and AMP in pure water, which were 51.33% and 76.5% after 360 min of irradiation, respectively. Also, when the photocatalytic degradation was carried out in a groundwater matrix, the efficiency slightly decreased. This can be related to the presence of dissolved ions such as Na^+ , K^+ , Ca^{2+} , Mg^{2+} , Cl^- , SO_4^{2-} , NO_3^- , and HCO_3^- in groundwater due to the water-rock interactions. These ions could potentially interfere during redox reactions and also occupy a site onto the photocatalyst surface during the adsorption process, leading to lower efficiencies when compared with pure water samples.

Although groundwater is a more complex matrix than pure water, 45 % and 76.9 % degradation were achieved for BPA and AMP respectively, after 6 hours (Figure 10). Thus, it was proven that BGM (300:1) can be used efficiently for the degradation of organic pollutants such as Bisphenol A and Acetaminophen in groundwater.

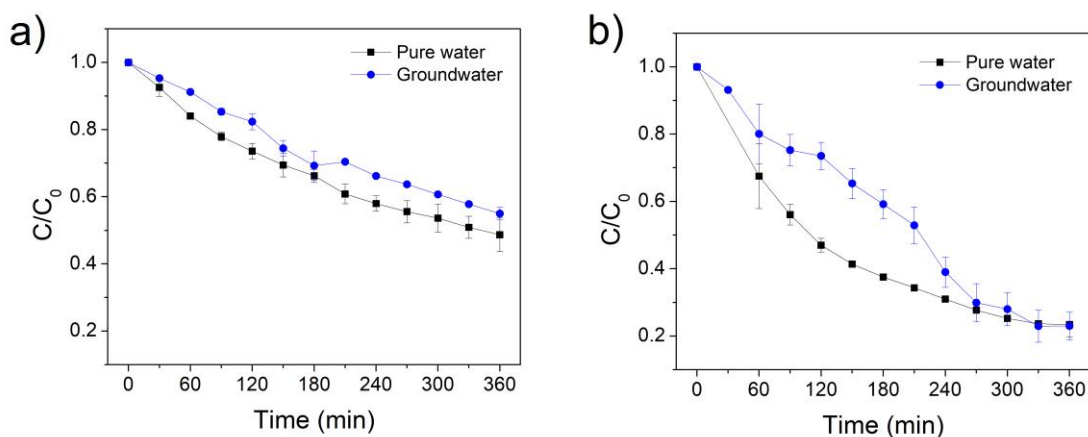


Figure 10. Degradation of BPA (a) and AMP (b) by BGM (300:1) composite in pure water and groundwater under visible light irradiation.

4. Conclusion

A composite material (BGM) with an optimal Bi_2O_3 :rGO ratio of 300:1 was obtained and successfully applied for the photocatalytic degradation of organic compounds under visible light irradiation. It was observed that the main function of rGO was delaying the recombination time of the photogenerated electron-hole pair, hence improving the photocatalytic activity of the composite. Through SEM and TEM it was demonstrated that the BGM composite is composed of the three different materials where the Bi_2O_3 nanoparticles are surrounded by rGO sheets that are decorated with MnO_{3n-1} nanoparticles. The active species trapping experiments demonstrated that h^+ are the major active species in the BGM photocatalytic reaction system. The photocatalytic material synthesized in this study was successfully used to efficiently degrade AMP and BPA in groundwater samples under visible light irradiation, achieving degradation percentages of 77 and 51% respectively.

5. References

- [1] J. Luo, Z. Yan, R. Liu, J. Xu, X. Wang, Synthesis and excellent visible light photocatalysis performance of magnetic reduced graphene oxide/ZnO/ZnFe₂O₄ composites, *RSC Adv.* 7 (2017) 23246–23254.
- [2] D. Zhang, F. Zeng, Visible light-activated cadmium-doped ZnO nanostructured photocatalyst for the treatment of methylene blue dye, *J. Mater. Sci.* 47 (2012) 2155–2161.
- [3] A. Serrà, Y. Zhang, B. Sepúlveda, E. Gómez, J. Nogués, J. Michler, L. Philippe, Highly active ZnO-based biomimetic fern-like microleaves for photocatalytic water decontamination using sunlight, *Appl. Catal. B Environ.* 248 (2019) 129–146. doi:10.1016/j.apcatb.2019.02.017.
- [4] E. Brillas, C.A. Martínez-Huitle, Decontamination of wastewaters containing synthetic organic dyes by electrochemical methods. An updated review, Elsevier, 2015. doi:10.1016/j.apcatb.2014.11.016.
- [5] Y. Wang, Q. Wang, X. Zhan, F. Wang, M. Safdar, J. He, Visible light driven type II heterostructures and their enhanced photocatalysis properties: a review, *Nanoscale.* 5 (2013) 8326. doi:10.1039/c3nr01577g.
- [6] C. Santhosh, V. Velmurugan, G. Jacob, S.K. Jeong, A.N. Grace, A. Bhatnagar, Role of nanomaterials in water treatment applications: A review, *Chem. Eng. J.* 306 (2016) 1116–1137. doi:10.1016/J.CEJ.2016.08.053.
- [7] W. Raza, M.M. Haque, M. Muneer, T. Harada, M. Matsumura, Synthesis, characterization and photocatalytic performance of visible light induced bismuth oxide nanoparticle, *J. Alloys Compd.* 648 (2015) 641–650. doi:10.1016/j.jallcom.2015.06.245.
- [8] K. Kasinathan, J. Kennedy, M. Elayaperumal, M. Henini, M. Malik, Photodegradation of organic pollutants RhB dye using UV simulated sunlight on ceria based TiO₂ nanomaterials for antibacterial applications, *Sci. Rep.* 6 (2016) 38064. doi:10.1038/srep38064.
- [9] Y. Shi, L. Luo, Y. Zhang, Y. Chen, S. Wang, L. Li, Y. Long, F. Jiang, Synthesis and characterization of porous platelet-shaped α -Bi₂O₃ with enhanced photocatalytic activity for 17 α -ethynylestradiol, *Ceram. Int.* 43 (2017) 7627–7635.

- [10] A. Kubacka, M. Fernández-García, G. Colón, Nanostructured Ti–M mixed-metal oxides: Toward a visible light-driven photocatalyst, *J. Catal.* 254 (2008) 272–284. doi:10.1016/J.JCAT.2008.01.005.
- [11] R. He, S. Cao, P. Zhou, J. Yu, Recent advances in visible light Bi-based photocatalysts, *Chinese J. Catal.* 35 (2014) 989–1007. doi:10.1016/s1872-2067(14)60075-9.
- [12] M. Jalalah, M. Faisal, H. Bouzid, J.-G. Park, S.A. Al-Sayari, A.A. Ismail, Comparative study on photocatalytic performances of crystalline α - and β -Bi₂O₃ nanoparticles under visible light, *J. Ind. Eng. Chem.* 30 (2015) 183–189. doi:10.1016/J.JIEC.2015.05.020.
- [13] G. Liu, S. Li, Y. Lu, J. Zhang, Z. Feng, C. Li, Controllable synthesis of α -Bi₂O₃ and γ -Bi₂O₃ with high photocatalytic activity by α -Bi₂O₃→ γ -Bi₂O₃→ α -Bi₂O₃ transformation in a facile precipitati, *J. Alloys Compd.* 689 (2016) 787–799. doi:10.1016/J.JALLCOM.2016.08.047.
- [14] J. Chen, J. Zhan, Q. Li, Exploration and crystal phase engineering from bismuthinite ore to visible-light responsive photocatalyst of Bi₂O₃, *J. Environ. Chem. Eng.* 7 (2019) 103375. doi:10.1016/J.JECE.2019.103375.
- [15] Z. Hu, J. Zhou, Y. Zhang, W. Liu, J. Zhou, W. Cai, The formation of a direct Z-scheme Bi₂O₃/MoO₃ composite nanocatalyst with improved photocatalytic activity under visible light, *Chem. Phys. Lett.* 706 (2018) 208–214. doi:10.1016/J.CPLETT.2018.06.006.
- [16] B. Feng, Z. Wu, J. Liu, K. Zhu, Z. Li, X. Jin, Y. Hou, Q. Xi, M. Cong, P. Liu, Q. Gu, Combination of ultrafast dye-sensitized-assisted electron transfer process and novel Z-scheme system: AgBr nanoparticles interspersed MoO₃ nanobelts for enhancing photocatalytic performance of RhB, *Appl. Catal. B Environ.* 206 (2017) 242–251. doi:10.1016/j.apcatb.2017.01.029.
- [17] M. Tahir, N.S. Amin, Performance analysis of nanostructured NiO–In₂O₃/TiO₂ catalyst for CO₂ photoreduction with H₂ in a monolith photoreactor, *Chem. Eng. J.* 285 (2016) 635–649. doi:10.1016/J.CEJ.2015.10.033.
- [18] J. Zhang, S. Zhang Qiao, L. Qi, J. Yu, Fabrication of NiS modified CdS nanorod p–n junction photocatalysts with enhanced visible-light photocatalytic H₂-production activity, *Phys. Chem. Chem. Phys.* 15 (2013) 12088–12094. doi:10.1039/c3cp50734c.

- [19] T. Di, B. Zhu, B. Cheng, J. Yu, J. Xu, A direct Z-scheme g-C₃N₄/SnS₂ photocatalyst with superior visible-light CO₂ reduction performance, *J. Catal.* 352 (2017) 532–541. doi:10.1016/J.JCAT.2017.06.006.
- [20] X. Li, J. Yu, S. Wageh, A.A. Al-Ghamdi, J. Xie, Graphene in Photocatalysis: A Review, *Small.* 12 (2016) 6640–6696. doi:10.1002/sml.201600382.
- [21] J. Xian, D. Li, J. Chen, X. Li, M. He, Y. Shao, L. Yu, J. Fang, TiO₂ Nanotube Array-Graphene-CdS Quantum Dots Composite Film in Z-Scheme with Enhanced Photoactivity and Photostability, *ACS Appl. Mater. Interfaces.* 6 (2014) 13157–13166. doi:10.1021/am5029999.
- [22] K. Iwashina, A. Iwase, Y.H. Ng, R. Amal, A. Kudo, Z-Schematic Water Splitting into H₂ and O₂ Using Metal Sulfide as a Hydrogen-Evolving Photocatalyst and Reduced Graphene Oxide as a Solid-State Electron Mediator, *J. Am. Chem. Soc.* 137 (2015) 604–607. doi:10.1021/ja511615s.
- [23] K. Valencia G., A. López, A. Hernández-Gordillo, R. Zanella, S.E. Rodil, Stabilized β-Bi₂O₃ nanoparticles from (BiO)₄CO₃(OH)₂ precursor and their photocatalytic properties under blue light, *Ceram. Int.* 44 (2018) 22329–22338. doi:10.1016/j.ceramint.2018.08.358.
- [24] L.A. Bursill, Crystallographic Shear in Molybdenum Trioxide, *Proc. R. Soc. A Math. Phys. Eng. Sci.* 311 (1969) 267–290. doi:10.1098/rspa.1969.0118.
- [25] R.L. Smith, G.S. Rohrer, Scanning Probe Microscopy of Cleaved Molybdates: α-MoO₃(010), Mo₁₈O₅₂(100), Mo₈O₂₃(010), and η-Mo₄O₁₁(100), *J. Solid State Chem.* 124 (1996) 104–115. doi:10.1006/jssc.1996.0213.
- [26] D. Wang, D. Su, R. Schlögl, Crystallographic shear defect in molybdenum oxides: Structure and TEM of molybdenum sub-oxides Mo₁₈O₅₂ and Mo₈O₂₃, *Cryst. Res. Technol.* 38 (2003) 153–159. doi:10.1002/crat.200310018.
- [27] A. Magnéli, The Crystal Structure of Mo₉O₂₆ (β'-Molybdenum Oxide) and Mo₈O₂₃ (β-Molybdenum Oxide), *Acta Chem. Scand.* 2 (1948) 501–517.
- [28] M. Sato, M. Onoda, Y. Matsuda, Structural transitions in Mo_nO_{3n-1} (n=9 and 10), *J. Phys. C Solid State Phys.* 20 (1987) 4763–4771. doi:10.1088/0022-3719/20/29/013.
- [29] L. Stobinski, B. Lesiak, A. Malolepszy, M. Mazurkiewicz, B. Mierzwa, J. Zemek, P. Jiricek, I. Bieloshapka, Graphene oxide and reduced graphene oxide studied by the XRD, TEM and electron spectroscopy methods, *J. Electron*

Spectros. Relat. Phenomena. 195 (2014) 145–154.
doi:10.1016/J.ELSPEC.2014.07.003.

[30] D. Yang, A. Velamakanni, G. Bozoklu, S. Park, M. Stoller, R.D. Piner, S. Stankovich, I. Jung, D.A. Field, C.A. Ventrice, R.S. Ruoff, Chemical analysis of graphene oxide films after heat and chemical treatments by X-ray photoelectron and Micro-Raman spectroscopy, *Carbon N. Y.* 47 (2009) 145–152.

[31] J. Sun, W. Tu, C. Chen, A. Plewa, H. Ye, J.A. Sam Oh, L. He, T. Wu, K. Zeng, L. Lu, Chemical Bonding Construction of Reduced Graphene Oxide-Anchored Few-Layer Bismuth Oxychloride for Synergistically Improving Sodium-Ion Storage, *Chem. Mater.* 31 (2019) 7311–7319.
doi:10.1021/acs.chemmater.9b01828.

[32] G. Žerjav, M.S. Arshad, P. Djinović, I. Junkar, J. Kovač, J. Zavašnik, A. Pintar, Improved electron–hole separation and migration in anatase TiO₂ nanorod/reduced graphene oxide composites and their influence on photocatalytic performance, *Nanoscale.* 9 (2017) 4578–4592.
doi:10.1039/C7NR00704C.

[33] A. Iwase, Y.H. Ng, Y. Ishiguro, A. Kudo, R. Amal, Reduced Graphene Oxide as a Solid-State Electron Mediator in Z-Scheme Photocatalytic Water Splitting under Visible Light, *J. Am. Chem. Soc.* 133 (2011).
doi:10.1021/ja203296z.

[34] J.W. MEDERNACH, R.L. SNYDER, Powder Diffraction Patterns and Structures of the Bismuth Oxides, *J. Am. Ceram. Soc.* 61 (1978) 494–497.
doi:10.1111/j.1151-2916.1978.tb16125.x.

[35] D. Barreca, F. Morazzoni, G.A. Rizzi, R. Scotti, E. Tondello, Molecular oxygen interaction with a spectroscopic and Bi₂O₃: Spectromagnetic investigation, *Phys. Chem. Chem. Phys.* 3 (2001) 1743–1749.
doi:10.1039/b009482j.

[36] M. Rouhani, Y.L. Foo, J. Hobley, J. Pan, G.S. Subramanian, X. Yu, A. Rusydi, S. Gorelik, Photochromism of amorphous molybdenum oxide films with different initial Mo⁵⁺ relative concentrations, *Appl. Surf. Sci.* 273 (2013) 150–158. doi:10.1016/J.APSUSC.2013.01.218.

[37] M. Vasilopoulou, A.M. Douvas, D.G. Georgiadou, L.C. Palilis, S. Kennou, L. Sygellou, A. Soultati, I. Kostis, G. Papadimitropoulos, D. Davazoglou, P. Argitis, The Influence of Hydrogenation and Oxygen Vacancies on Molybdenum Oxides Work Function and Gap States for Application in Organic

Optoelectronics, *J. Am. Chem. Soc.* 134 (2012) 16178–16187. doi:10.1021/ja3026906.

[38] R. Kashfi-Sadabad, S. Yazdani, T.D. Huan, Z. Cai, M.T. Pettes, Role of Oxygen Vacancy Defects in the Electrocatalytic Activity of Substoichiometric Molybdenum Oxide, *J. Phys. Chem. C.* 122 (2018) 18212–18222. doi:10.1021/acs.jpcc.8b03536.

[39] K.S.W. Sing, D.H. Everett, R.A.W. Haul, L. Moscou, R.A. Pierotti, J. Rouquerol, T. Siemieniewska, Reporting Physisorption Data for Gas/Solid Systems with Special Reference to the Determination of Surface Area and Porosity., *Pure Appl. Chem.* 57 (1985) 603–619.

[40] H. Jiang, H. Dai, X. Meng, K. Ji, L. Zhang, J. Deng, Porous olive-like BiVO₄: Alchohydrothermal preparation and excellent visible-light-driven photocatalytic performance for the degradation of phenol, *Appl. Catal. B Environ.* 105 (2011) 326–334. doi:10.1016/j.apcatb.2011.04.026.

[41] Z. Zhao, H. Dai, J. Deng, Y. Liu, C.T. Au, Effect of sulfur doping on the photocatalytic performance of BiVO₄ under visible light illumination, *Cuihua Xuebao/Chinese J. Catal.* 34 (2013) 1617–1626. doi:10.1016/S1872-2067(12)60632-9.

[42] W. Gao, M. Wang, C. Ran, L. Li, Facile one-pot synthesis of MoS₂ quantum dots–graphene–TiO₂ composites for highly enhanced photocatalytic properties, *Chem. Commun.* 51 (2015) 1709–1712. doi:10.1039/C4CC08984G.

[43] S. Akshatha, S. Sreenivasa, L. Parashuram, V.U. Kumar, S.C. Sharma, H. Nagabhushana, S. Kumar, T. Maiyalagan, Synergistic effect of hybrid Ce³⁺/Ce⁴⁺ doped Bi₂O₃ nano-sphere photocatalyst for enhanced photocatalytic degradation of alizarin red S dye and its NUV excited photoluminescence studies, *J. Environ. Chem. Eng.* 7 (2019) 103053. doi:10.1016/j.jece.2019.103053.

[44] A. Maroz, O. Brede, Reaction of radicals with benzoquinone - Addition or electron transfer?, *Radiat. Phys. Chem.* 67 (2003) 275–278. doi:10.1016/S0969-806X(03)00051-3.

[45] D.J. Lapworth, N. Baran, M.E. Stuart, R.S. Ward, Emerging organic contaminants in groundwater: A review of sources, fate and occurrence, *Environ. Pollut.* 163 (2012) 287–303. doi:10.1016/j.envpol.2011.12.034.

[46] D. Barceló, Emerging pollutants in water analysis, *Trends Anal. Chem.* 22 (2003). doi:10.1016/S0165-9936(03)01106-3.

Chapter 4

Gd³⁺ doped BiVO₄ and visible light-emitting diodes (LED) for photocatalytic decomposition of bisphenol A, bisphenol S, and bisphenol AF in water

1. Introduction

The presence of emerging contaminants in the environment has become a critical issue worldwide. A large amount of persistent organic pollutants such as pharmaceuticals, personal care products, pesticides, flame retardants, and industrial additives, among others, are released into the environment every day. These pollutants are easily dispersed once they have entered the ecosystems [1,2]. Conventional treatment processes are not able to completely eliminate these contaminants, which are usually present in low concentrations (mg L^{-1} or ng L^{-1}) in the aquatic environment. It has been found that these organic pollutants cause a highly negative impact on the environment. Specifically, endocrine disruptive compounds (EDCs), because of its estrogenic and/or antiandrogenic activity, have been identified as potential threats to wildlife and human health causing, for instance, reproductive disorders, and increased chance of getting breast, testicular, or prostate cancer. [3–5]. Bisphenol A (BPA) is considered a type of EDCs. It is mainly used in the plastic industry as a stabilizer in the production of epoxy resins and polycarbonates, and is also a constituent in many commercial products such as baby toys, drinking water bottles, medical equipment, and thermal receipt papers, among others [6–8]. The concern about the effects of BPA has raised in some countries of North America and the European Union to take action in regulations related to the production and use of this compound [3,9]. Consequently, analogs of BPA, such as bisphenol S (BPS), bisphenol F (BPF), and bisphenol AF (BPAF), started to be used more frequently as substituents of BPA. However, it has been proven that these BPA analogs, due to its similar molecular structure, may trigger negative effects of equal or even greater magnitude than those caused by BPA [3,10,11]. Up to now, BPA has been detected in water bodies all over the world in concentrations ranging between 9.9 to 2700 ng L^{-1} [7]. Likewise, the presence of BPS and BPAF in wastewater treatment plants has been reported at concentration levels up to 109 and 16.5 ng L^{-1} , respectively [11].

Heterogeneous photocatalysis has been studied as a promising alternative for the degradation of organic persistent pollutants, such as bisphenols, from water and wastewater [12,13]. Titanium dioxide (TiO_2) is the most commonly used photocatalyst, especially because it has desirable characteristics like chemical stability, non-toxicity, and low costs [14]. However, due to its wide band gap (3.2 eV), this material is activated only under UV light irradiation ($\lambda < 400 \text{ nm}$) which represents about 3 to 5% of the solar spectrum [15]. So far, ultraviolet light sources have been used to activate photocatalysts such as TiO_2 , but nowadays researchers are looking to make a transition to more efficient and inexpensive

light sources. Therefore, taking full advantage of sunlight, which mostly emits visible light, is an expected approach for the development of new technologies [16,17]. Alongside solar light, the incorporation of light-emitting diodes (LED) as visible-light sources in photocatalytic processes seems to be promising. LED lamps have been considered as an environmental-friendly technology that additionally presents several advantages over conventional UV-light sources, such as compact configuration, relatively long-life span (50,000 h), better resistance to mechanical impact. Moreover, they are more energy efficient and do not contain toxic elements [18–20]. Whether the light source comes directly from the sun or an LED lamp, the development of efficient visible-light-driven photocatalysts is essential.

Hence, special attention has been paid to bismuth-based materials as suitable materials for photocatalytic degradation of organic compounds under visible light radiation ($400 >\lambda < 700$ nm) [21–23]. Specifically, monoclinic bismuth vanadate (BiVO_4) has shown high visible light absorption, and because of its narrow band gap energy (2.4 eV) has been reported as an efficient photocatalyst [24–26]. However, the photocatalytic efficiency of BiVO_4 can still be improved for avoiding rapid electron-hole recombination and slow charge transportation [25]. Different strategies have been followed for this purpose, among them, doping with metals [27,28], non-metals [29,30], or rare-earths [31–33].

There are only a couple of studies that have investigated the photocatalytic performance of Gd^{3+} doped BiVO_4 . Those studies showed contradictory results regarding the influence of Gd^{3+} on photocatalyst response to visible light irradiation. On the one hand, Xu et al. [34] stated that the presence of Gd^{3+} promotes the separation and transfer of electrons and holes for efficient degradation of methylene blue under visible light irradiation. On the other hand, Luo et al. [35] found that Gd^{3+} doping favored photocatalytic activity under UV light but impaired performance under visible light irradiation in Rhodamine b degradation. Both studies used a dye as test molecules. However, experts claim that dyes are not suitable molecules for use in the study of visible-light-driven photocatalysts, since these can absorb light in that range of the spectrum and sensitize the photocatalysts [25,36].

In the present work, bisphenol A was used as a test molecule to study the effect of Gd^{3+} content on photocatalytic efficiency of BiVO_4 using an LED lamp as a light source. The decomposition of BPS and BPAF was also assessed. Moreover, the main reactive species were identified, and a decomposition pathway was proposed.

2. Materials and Methods

2.1 Chemicals

All chemicals used were analytical grade reagents. Bismuth (III) nitrate pentahydrate, ammonium metavanadate, ethylene glycol, bisphenol A, bisphenol S, bisphenol AF, α -D-Glucose, Gadolinium (III) chloride hexahydrate, ammonium oxalate and 1,4-benzoquinone were purchased from Sigma-Aldrich and were used without further purification. HPLC grade solvents were used for chromatographic analysis.

2.2 Synthesis of Photocatalysts

Gd³⁺ doped photocatalysts were prepared through a modified method of the thermal synthesis proposed by W. Yin et al. [37]. Briefly, 3 mmol of Bi(NO₃)₃·5H₂O and 3 mmol of NH₄VO₃ were dissolved in 30 ml of ethylene glycol in an oil bath at 60°C. Once a clarifying solution was formed, different concentrations of GdCl₃·6H₂O were added to obtain 1%, 2%, 4%, and 6% of Gadolinium in molar mass. After 30 minutes of vigorous stirring, 400 mg of as-prepared carbonaceous template spheres were dispersed in order to favor the metal ions precipitation at templates surface promoting a gradual interaction with dopants and the settling of the terminal products [37]. The solution was kept in the oven at 60°C for 12 hours, then the temperature was raised to 100°C and kept for another 12 hours. Afterward, the precipitate was collected, washed several times with distilled water and ethanol, and dried at 80°C in an oven overnight. The dried powder was calcinated for 2 hours at 550°C using a ramp of 10°C min⁻¹. The prepared Gd³⁺ doped photocatalysts by loading of a different molar mass of Gd³⁺ were denoted as BV-Gd-1%, BV-Gd-2%, BV-Gd-4%, and BV-Gd-6%. Undoped BiVO₄ was synthesized in the same manner without the addition of GdCl₃·6H₂O and was denoted as BV.

Carbonaceous template spheres were prepared by a hydrothermal method as follows: 0.5 M of α -D-Glucose was dissolved in 80 ml of pure water. The solution was placed in a 100 ml autoclave and heat at 180°C for 4.5 hours. After being cooled at room temperature, the precipitated was collected and washed with water and ethanol several times. Finally, the product was dried at 80°C for 12 hours [38].

2.3 Characterization techniques

X-ray diffraction (XRD) patterns and crystallographic information were obtained using a diffractometer (PANalytical Empyrean) with Co K α radiation source

($\lambda=1.7809 \text{ \AA}$) at 40 kV and 30 mA. The morphology and particle size of photocatalysts were observed using a scanning electron microscope (SEM, Hitachi S-4800) and transmission electron microscope (TEM, Hitachi HT7700). N_2 sorption experiments were carried out in a TriStar II Plus and specific surface area was estimated using the Brunauer-Emmett-Teller (BET) method. The UV-Vis diffuse reflectance spectra (DRS) was determined on a UV-Vis spectrometer (Agilent Cary 5000) in the wavelength range of 250 to 800 nm using spectralon standard as reference. X-ray photoelectron spectroscopy (XPS) was performed on an ESCALAB 250Xi (Thermo Fisher Scientific) spectrophotometer with monochromatic Al-K α (1486.6 eV) X-ray source. Raman spectra were acquired with a Renishaw inVia Micro Raman spectrometer. Sample excitation was carried out with a 514 nm green laser.

2.4 Photocatalytic activity

The photocatalytic activity of doped and un-doped BiVO_4 materials was evaluated through the degradation of Bisphenol A in water under visible light irradiation. An LED lamp with 36 W power consumption and 730 lm luminous intensity was used. The photocatalytic reaction was carried out in a 50 ml quartz flask. 1 g L^{-1} of the photocatalyst was added to a BPA solution with a concentration of 10 mg L^{-1} . To ensure the adsorption-desorption equilibrium between photocatalyst and contaminant, the mixture solution was stirred for 30 min in the dark. Once the solution was placed under visible LED light irradiation, aliquots were withdrawn according to fixed irradiation intervals. To remove the photocatalyst, all samples were filtered through regenerated cellulose syringe filters ($0.22 \mu\text{m}$).

The photocatalyst with the highest efficiency in the degradation of BPA (BV-Gd-4%) was chosen among the doped and undoped synthesized materials to perform the degradation of BPS and BPAF. The same experimental conditions used for BPA tests were used for BPS and BPAF experiments. Raw and remaining pollutant concentrations before and after the treatment were analyzed by high-performance liquid chromatography (HPLC, Shimadzu) equipped with a UV-Vis detector at a wavelength of 270 and 240 nm using a C18 column (Kinetex, $5 \mu\text{m}$, $150 \times 4.6 \text{ mm}$). Analyses were performed using methanol and water (30:70) v/v as a mobile phase in the isocratic mode with a flow rate of 0.5 ml min^{-1} for the total 12 min.

The stability of the BV-Gd-4% was investigated by measuring dissolved metal ions before and after photocatalytic treatment by means of Inductively Coupled Plasma – Optical Emission Spectrometry (ICP-OES Agilent 5100) to ensure that

the photocatalyst is not releasing toxic metals in the water matrix during treatment. Also, reusability tests were performed as follows: the BV-Gd-4% photocatalyst was recovered by centrifugation and rinsed several times with water and ethanol. After that, the photocatalyst was dried at 60°C overnight, and the recovered dry powder was used in a new reaction with adjusted volume to keep the same conditions in all the experiments. Moreover, isopropyl alcohol (IPA), ammonium oxalate (AO), and 4-benzoquinone (BQ) were used as scavengers of hydroxyl free radicals $^{\circ}\text{OH}$, photo-generated holes h^+ , and superoxide radicals O_2^- respectively during scavenging tests in order to determine the main reactive species. The experiments were conducted similarly to the above-mentioned photocatalytic experiments, except that 1 mmol of different radical scavengers was added to the reaction system.

3. Results and Discussion

3.1 Photocatalysts characterization

XRD measurements were performed to characterize the crystal structure of all synthesized materials. Figure 1a shows the diffraction patterns of the compositions 0, 1, 2, 4, and 6 % in molar mass of Gd^{3+} doped BiVO_4 system. The XRD pattern for BV, BV-Gd-1%, and BV-Gd- 2% can be indexed as a monoclinic Clinobisvanite structure (JCPDS file 98-010-0602). The undoped BiVO_4 (BV) only shows the planes that correspond to the Clinobisvanite BiVO_4 (C 1 2/c 1 space group). Interestingly, a second tetragonal bismuth oxide phase (JCPDS file 01-078-1793) is present in a minor proportion in all doped samples. This can be corroborated by the appearance of distinct peaks for (110), (200), and (112) planes at 28 and 38° in 2θ scale. It can be observed in Figure 1c that the increase in gadolinium concentration leads to a phase transformation of monoclinic BiVO_4 to tetragonal BiVO_4 , this phase change has already been reported previously in doped BiVO_4 structures [35,39,40]. Thus, for BV-Gd-4% and BV-Gd-6%, a good fitting with tetragonal dreyerite BiVO_4 structure (JCPDS file 00-014-0133) was observed, and in addition to the slight presence of Tetragonal Bi_2O_3 phase, monoclinic Bismuth Gadolinium Vanadium Oxide $\text{Bi}_{0.95}\text{Gd}_{0.05}\text{VO}_4$ (JCPDS file 00-033-0123) was formed in these two materials. The BiVO_4 and $\text{Bi}_{0.95}\text{Gd}_{0.05}\text{VO}_4$ phases can be differentiated for the broad peak splitting behavior ($2\theta^{\circ}\sim 33.64$) that indicates the distortion of the monoclinic structure (Figure 1b). The structural distortion may be due to the incorporation of Gd^{3+} ions into the BiVO_4 structure. Interestingly it was found that, compared to undoped material, the unit cell of the monoclinic BiVO_4 phase slightly expands after the addition of gadolinium (Figure 1c), probably because of Gd^{3+} has been incorporated as an

interstitial defect. In contrast, a decrease in the unit cell volume is observed as the concentration of Gd^{3+} increases in BV-Gd-4% and BV-Gd-6% that present the tetragonal $BiVO_4$ phase (Figure 1c). In this case, it can be inferred that Gd^{3+} is substituting Bi^{3+} sites in the structure, and because of the smaller ionic size of Gd^{3+} (0.0938 nm) compared with Bi^{3+} (0.103 nm), a change in the length of the B-O links, as well as a decrease in the unit cell volume is expected.

The difference between the observed and calculated XRD profile data has been obtained by pattern matching analysis for all the studied samples (supplementary information S2, Figures S1-S5.). In the same way, lattice parameters, unit cell volume, and the goodness of chi-square (χ^2) fitting parameter were calculated and are shown in Table 1. Also, the crystallite sizes of the synthesized materials were calculated by using the Scherrer equation, $t = K\lambda/B\cos k$, where λ is the X-ray wavelength (\AA), B is the full width at half maximum, k is Bragg angle, K is a factor depending on crystallite shape and t is the crystallite size (\AA).

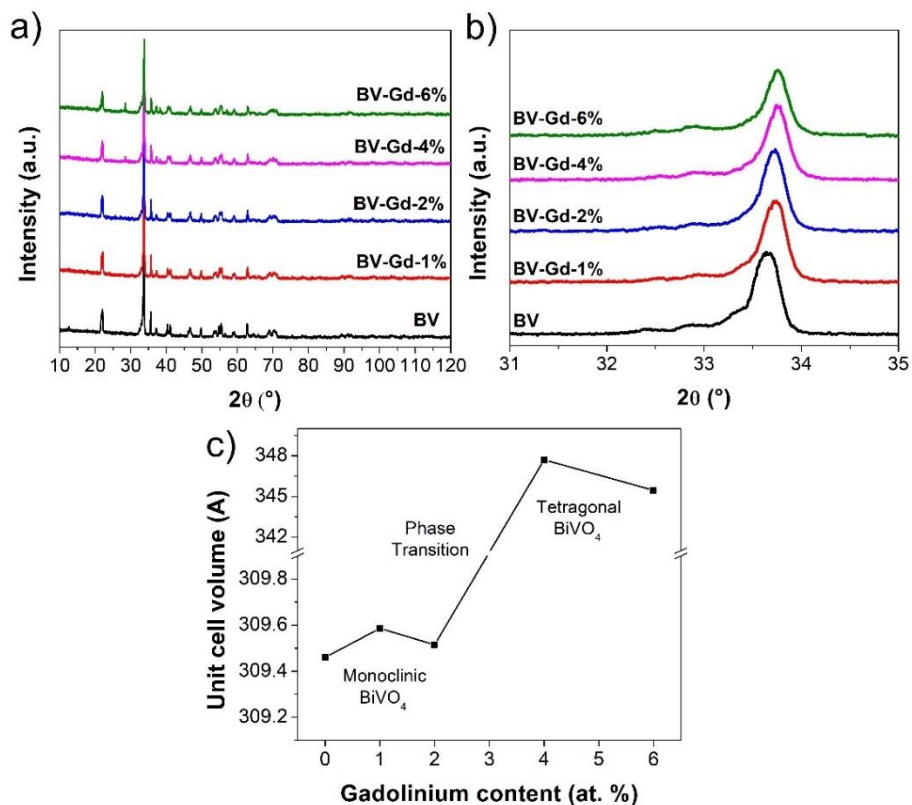


Figure 1. a) X-ray diffraction patterns of the composition 0, 1, 2, 4, and 6 % in molar mass of Gd^{3+} doped $BiVO_4$ system. b) Amplification of 33.64 peaks. c) Unit cell volume and crystalline phase at different Gd^{3+} content.

Table 1. Crystallographic parameters of studied samples.

Material	Phases	Spatial group	Lattice Parameters			Unit cell volume (Å ³)	Chi-square (χ ²)	Crystallite size (nm)
			a (Å)	B (Å)	C (Å)			
BV	m*-BiVO ₄	I2/a	5.18981	11.69854	5.09713	309.460	1.575	81
BV-Gd-1%	m-BiVO ₄	I2/a	5.18573	11.69390	5.10522	309.586	0.940	92
	t*-Bi ₂ O ₃	P-421c	7.66341	7.66341	5.61061	327.782		
BV-Gd-2%	m-BiVO ₄	I2/a	5.17985	11.69933	5.10748	309.515	0.987	60
	t-Bi ₂ O ₃	P-421c	7.68741	7.68741	5.61062	331.566		
BV-Gd-4%	Bi _{0.95} Gd _{0.05} VO ₄	P21/c	5.15209	5.15210	11.74611	311.789	1.203	89
	t-BiVO ₄	I41/amd	7.34745	7.34745	6.44067	347.700		
	t-Bi ₂ O ₃	P-421c	7.68477	7.68477	5.61992	331.889		
BV-Gd-6%	Bi _{0.95} Gd _{0.05} VO ₄	P21/c	5.14614	5.14612	11.68754	309.515	1.216	89
	t-BiVO ₄	I41/amd	7.32491	7.32491	6.43848	345.452		
	t-Bi ₂ O ₃	P-421c	7.65749	7.65749	5.61879	329.470		

*m = monoclinic, t = tetragonal

Figure 2 shows the Raman spectra of all the synthesized materials. Characteristic bands of BiVO₄ are observed at 203-211, 322-352, and 810-820 cm⁻¹. Specifically, the band at 203-211 corresponds to the BiVO₄ structural formation. Likewise, weak vibration peaks at 322-352 cm⁻¹ are assigned to symmetric and asymmetric deformation mode of VO₄³⁻, whereas the higher band at 810-820 cm⁻¹ corresponds to symmetric V-O bond vibration [41,42]. The peak intensity dramatically decreased as Gd³⁺ content was increasing. This suggests, in accordance with XRD analysis, that the presence of dopant has influenced structural properties causing internal stress in the crystalline structure and probably inhibition of lattice vibration [43,44].

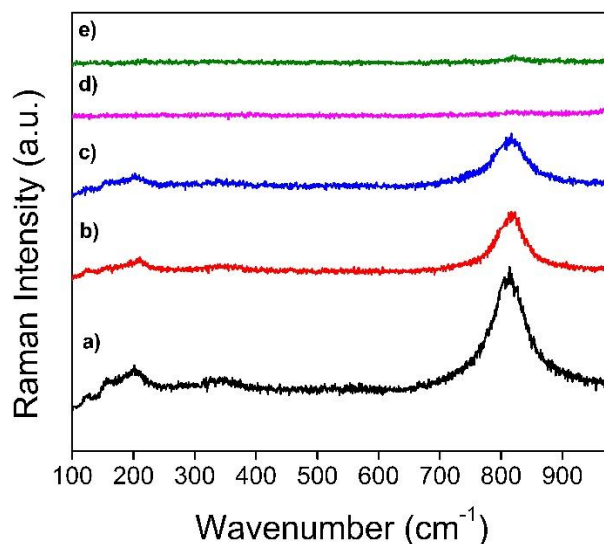


Figure 2. Raman spectra of a) BV, b) BV-Gd-1%, c) BV-Gd-2%, d) BV-Gd-4%, and e) BV-Gd-6%.

TEM and SEM images of the synthesized materials are shown in Figure 3. Since the synthesis conditions were the same for all the as prepared photocatalyst materials, it can be inferred that an increase in the concentration of Gd^{3+} influences the obtained morphology. Micrographs of un-doped $BiVO_4$ show agglomerated sphere-like shape particles. In Gd^{3+} doped particles deformation of spherical shape is observed, this may be occurring as a consequence of the sintering of particles. The average particle size of 60 to 90 nm is observed and confirmed by XRD analysis (Table 1).

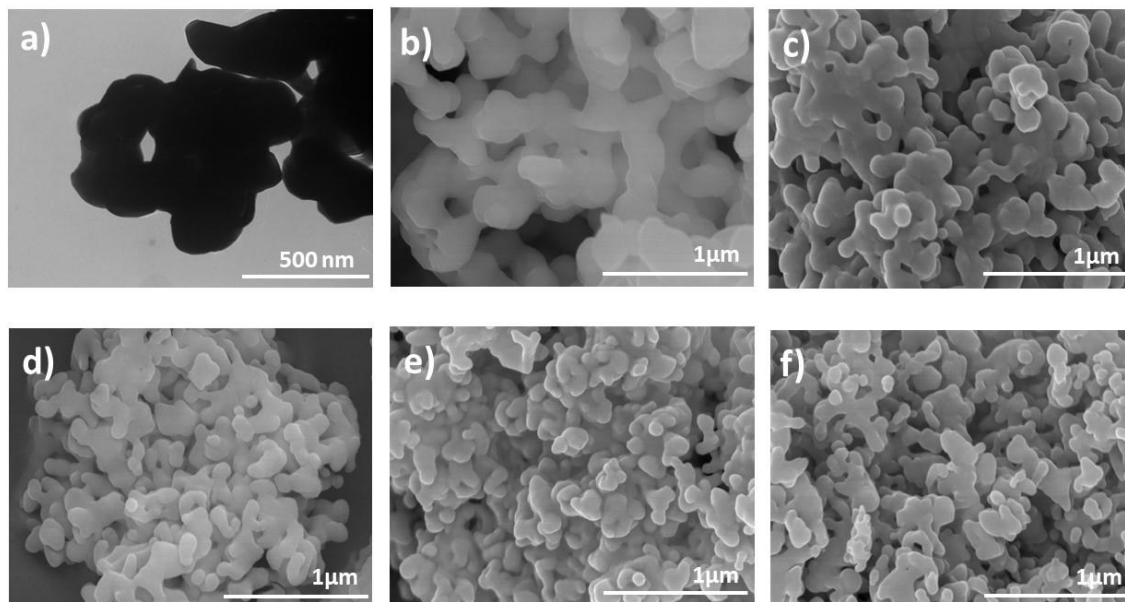


Figure 3. a) TEM and b) SEM images of undoped BiVO₄ (BV); and SEM images of Gd³⁺ doped BiVO₄ materials: c) BV-Gd-1%, d) BV-Gd-2%, e) BV-Gd-4%, and f) BV-Gd-6%.

The BET surface area of the synthesized photocatalysts is presented in Table 2. It is known that BiVO₄ normally has a low surface area. Though, it is noted that as gadolinium concentration increases, the surface area does, too. According to Obregon and Colón [45] surface area may show a slight increment when the tetragonal phase is present in the BiVO₄ systems, which is the case of BV-Gd-4% and BV-Gd-6%. An increase in the photocatalyst's surface area can positively influence its performance by increasing the number of active sites, and the reachable area to harvest visible light [26,46].

Table 2. BET surface area and band gap of the synthesized materials.

Material	BET surface area (m ² /g)	Band gap (eV)
BV	2.64	2.44
BV-Gd-1%	4.08	2.46
BV-Gd-2%	4.84	2.45
BV-Gd-4%	5.64	2.46
BV-Gd-6%	6.13	2.47

The band gap of the as-prepared materials was estimated from the absorption data obtained by diffuse reflectance. The Kubelka-Munk Function (KMF), expressed in Equation 1, multiplied by photon energy to the power of 0.5 was plotted in axis Y vs energy of the incident light in axis X (Figure 4). Then, the extrapolation of the linear region towards the x-axis intercept of each graph provided the indirect band gap of doped and undoped BiVO₄ materials.

$$KMF = F(R_{\infty}) = (1 - R_{\infty})^2 / 2R_{\infty} = K/S \quad \text{Eq. (1)}$$

Where R_{∞} is the absolute reflectance of a layer with an infinite thickness, K is the absorption coefficient, and S is the scattering coefficient.

According to diffuse reflectance UV-vis spectra, all samples showed strong adsorption in the visible region. Specifically, the adsorption band edge was around 520 nm for doped and un-doped photocatalysts. This suggests that the presence of gadolinium doesn't lead to a significant shift in the adsorption edge. Previous reports have determined a band gap of 2.44 eV and 2.9 eV for pure monoclinic and tetragonal BiVO₄ respectively [47,48]. Herein, the band gap obtained for undoped BiVO₄ was 2.44 eV. Likewise, a very similar band gap was

obtained for the doped materials (Table 2), including the ones having a tetragonal BiVO_4 phase. This is not surprising since it is well known that the presence of dopants and the formation of heterostructures may strongly influence the band gap structure [49,50]. Therefore, the presence of Gd^{3+} and the formation of Bi_2O_3 and $\text{Bi}_{0.95}\text{Gd}_{0.05}\text{VO}_4$ heterostructures in BV-Gd-4% and BV-Gd-6% kept a narrower band gap of 2.46 and 2.47 eV respectively.

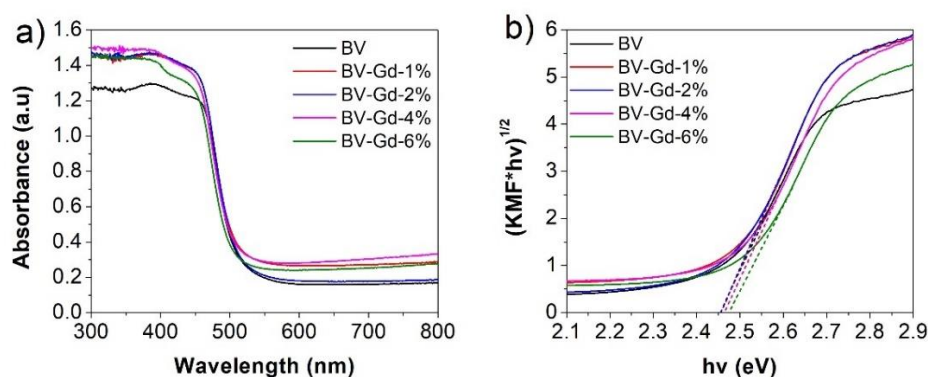


Figure 4. a) Diffuse reflectance UV-Vis spectra. b) Kubelka-Munk plot.

As discussed in the next section (3.2) the most efficient photocatalyst was the one doped with 4% of Gd^{3+} (BV-Gd-4%), therefore XPS analysis were carried out to determine the chemical states of BV and BV-Gd-4%. Figure 5e depicts the survey spectra of the two analyzed samples, both of them showed the expected peaks for all the constituent elements, Bi (5d, 4f, 4d, 4p) V (2p and 2s), O 1s, and in the case of doped photocatalyst, the Gd (4f, 4d, and 3d) peaks were present as well. Therefore, it can be assumed that Gd^{3+} was successfully doped into the BiVO_4 structure, which is in accordance with the high-resolution XPS spectra of Gd 4d with a binding energy of 142 eV (Figure 5d) and with the obtained XRD and Raman analysis. The high-resolution XPS spectra of O 1s are shown in Figure 5b where the peaks are located at 529.7 and 529.8 eV of binding energy for BV and BV-Gd-4% respectively and can be related to the presence of O_2^- anions. In Figure 5a two symmetric peaks are shown for Bi $4f_{5/2}$ and Bi $4f_{7/2}$ in both materials at binding energies around 164 and 159 eV respectively, which correspond to Bi^{3+} chemical state [51]. Furthermore, V $2p_{1/2}$ and V $2p_{3/2}$ orbitals at 516 and 524 eV showed in Figure 5c, indicate the presence of vanadium as a V^{5+} oxidation state [52].

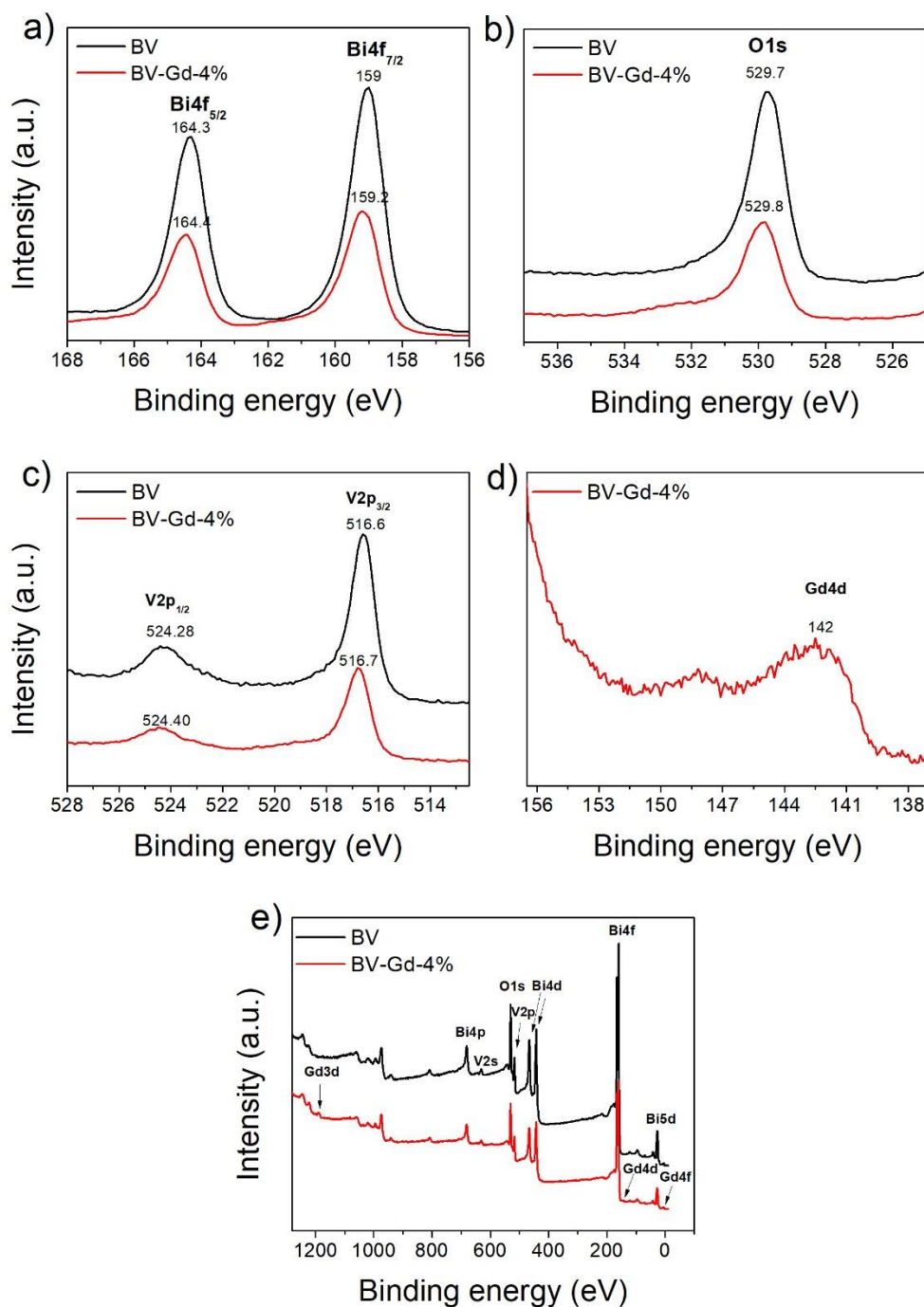


Figure 5. XPS spectra of BV and BV-Gd-4% photocatalyst: (a) survey, (b) O 1s peaks, (c) V 2p peaks, (d) Bi 4f peaks, and (e) Gd 4d peak.

3.2 Photocatalytic activity

The photocatalytic performance of the synthesized materials was studied using BPA as a test molecule. Specifically, the effect of Gd³⁺ content on the doped materials was evaluated through photocatalytic experiments that were performed by using an LED visible light lamp as the irradiation source.

Photolysis of BPA was neglected since no significant changes in BPA concentration was observed after 3 hours of irradiation. Figure 6, shows that the performance of the doped materials was better than the pristine BiVO_4 . After 3 hours of irradiation, the initial concentration of BPA was efficiently degraded up to $58.6\% \pm 1.19$, $51.43\% \pm 1.54$, $77.02\% \pm 2.16$, and $72.16\% \pm 0.34$ for BV-Gd-1%, BV-Gd-2%, BV-Gd-4%, and BV-Gd-6% respectively, whereas BV only reached $42.12\% \pm 0.90$. A greater increase in photocatalytic efficiency was achieved when Gd^{3+} concentration exceeds 2% in molar mass. This can be related to the results obtained by XRD analysis, which showed that a transformation phase from monoclinic to tetragonal occurs in the BiVO_4 structure when Gd^{3+} content is higher than 2% in molar mass. Also, Bi_2O_3 and $\text{Bi}_{0.95}\text{Gd}_{0.05}\text{VO}_4$ phases were detected in BV-Gd-4% and BV-Gd-6% which is related to their high efficiency compared to the synthesized photocatalysts loaded with less than 4% of Gd^{3+} . It has been previously reported that heterostructured materials may promote the separation of charge carriers (electron-hole pairs) as well as their diffusion towards photocatalyst's surface, enhancing its photocatalytic activity [53,54]. For instance, Mao et al. [55] described the p-n heterojunction formed by Bi_2O_3 and BiVO_4 in which a direct z-scheme could be formed under visible light irradiation fostering that holes on the valence band of Bi_2O_3 and the electrons on the conduction band of BiVO_4 recombine directly at their interfacial region. The migration of electrons from CB of Bi_2O_3 could be capture by the O_2 chemisorbed at the surface to generate superoxide radicals ($\cdot\text{O}_2$) while the remaining holes in BiVO_4 directly oxidize the organic compounds. According to the authors, the photoactivity was dramatically improved based on this charge transfer mode.

BV-Gd-6% was slightly less efficient than BV-Gd-4% and this can be explained by the classical doping theory in which increasing the dopant concentration will gradually improve photocatalytic efficiency until a certain point in which dopant incites recombination, instead of promoting charge carriers separation [39]. Furthermore, gadolinium doping, compared to other rare earth, has been shown to have a positive influence on improving photocatalytic efficiency of other materials such as SnO_2 [56], TiO_2 [57], and Bi_2O_3 [32] under visible light. This is due to the particular characteristics of Gd^{3+} ion that has an electronic structure with a partially occupied d and f orbitals which promote the formation of complexes that may facilitate the adsorption of contaminants on the surface of the photocatalyst [58].

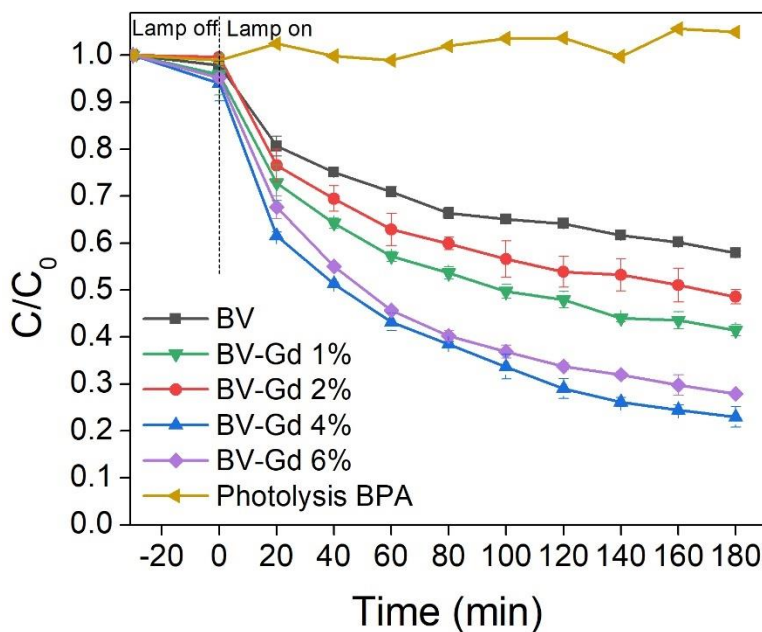


Figure 6. Effect of Gd^{3+} content onto $BiVO_4$ photocatalyst for degradation of BPA under LED visible-light irradiation.

There are a couple of studies about Gd^{3+} doped $BiVO_4$ for photocatalytic degradation of dyes. For instance, Y. Luo et. al. found for degradation of Rhodamine b that after doping the $BiVO_4$, the material became active in the UV range but poorly active under visible light, probably because of the blue-shifted adsorption edge caused for crystalline phase transformation that led to a wider band gap (2.9 eV) [35]. On the contrary, H. Xu, et. al. reported successfully photocatalytic degradation of methylene blue under visible light using $Gd-BiVO_4$ [34]. However, studies using dyes as test molecules in the examination of visible-light photocatalysts does not give conclusive arguments on intrinsic visible-light response of the photocatalysts, mainly because dyes may adsorb visible light and sensitize the photocatalyst [25,36]. Herein, bisphenol A is being used as a test molecule and BV-Gd-4% clearly showed the best photocatalytic performance over BPA decomposition under LED visible light irradiation. Therefore, BV-Gd-4% was used as the photocatalyst for studying the decomposition of BPS and BPAF as well. Figure 7a depicts the photocatalytic decomposition of BPA, BPS, and BPAF after 3 hours reaction, showing degradation efficiencies of $77.02\% \pm 2.16$, $44.36\% \pm 2.74$, and $74.11\% \pm 5.09$ respectively. In addition, the initial disappearance rates using 1 g L^{-1} of BV-Gd-4% were calculated considering the first 25 min of photocatalytic reaction (Figure 7b), in which the linearity indicates zero-order kinetics. BPS showed the fastest

disappearance rate ($0.35 \mu\text{mol L}^{-1} \text{min}^{-1}$) while the lowest one was for BPAF ($0.46 \mu\text{mol L}^{-1} \text{min}^{-1}$).

The degradation efficiency of BPA and its analogs (BPS and BPAF) using BV-Gd-4% can not be directly compared with other studies because the experimental conditions differ from one study to another. However, BV-Gd-4% could be considered a competitive photocatalyst when compared to other bismuth-based photocatalysts for the removal of the same contaminants. For instance, BPA photodegradation has been extensively studied and some authors assessed better photocatalytic efficiency whereas others obtained lower efficiency than the reported herein. Tateishi et al. [59] reported an outstanding degradation performance using AgI/Bi₇O₉I₃ which degraded 100% of BPA after 30 min using a 300 W Xe lamp. On the other hand, relatively low photocatalytic efficiency in the degradation of BPA was reported using Bi₅O₇I that achieved 90% degradation after 4 h with a 500 W iodine tungsten lamp [60]. Similarly, BiOI/Bi₂MoO₆ assessed 95% of BPA degradation after 4 h using a 300 W Xe lamp [61].

The photocatalytic degradation of BPS has been less investigated than BPA. In a recent review about BPS remediation in water, only four photocatalysts were mentioned. Within them, BiOCl-g- C₃N₄ ultrathin heterostructure reached 72% of BPS degradation after 120 min under visible light irradiation [62]. BPAF degradation through photocatalysis has not been investigated in depth yet. As far as we know no studies are reporting BPAF decomposition using bismuth-based photocatalysis.

To complement photocatalytic studies, the photocatalytic degradation of a multi-component solution containing simultaneously 10 mg/L of BPA, BPS, and BPAF was performed. This provides insight into how photocatalyst efficiency might be affected in a real matrix where more than one contaminant is present. As it is shown in Figure 7c the efficiency and disappearance rate decreased for some of the pollutants, with respect to their performance in the mono-component system. Even though BPA still has the highest degradation efficiency, its disappearance rate ($0.79 \mu\text{mol L}^{-1} \text{min}^{-1}$) was decreased by 47% in the multicomponent medium. For BPS and BPAF the efficiency dropped by 57 and 69% respectively, and so were its disappearance rates (Figure 7d). These results were expected since in a multicomponent system there is more competition to acquire the active sites, consequently, the efficiency and speed of the photocatalytic reactions are affected.

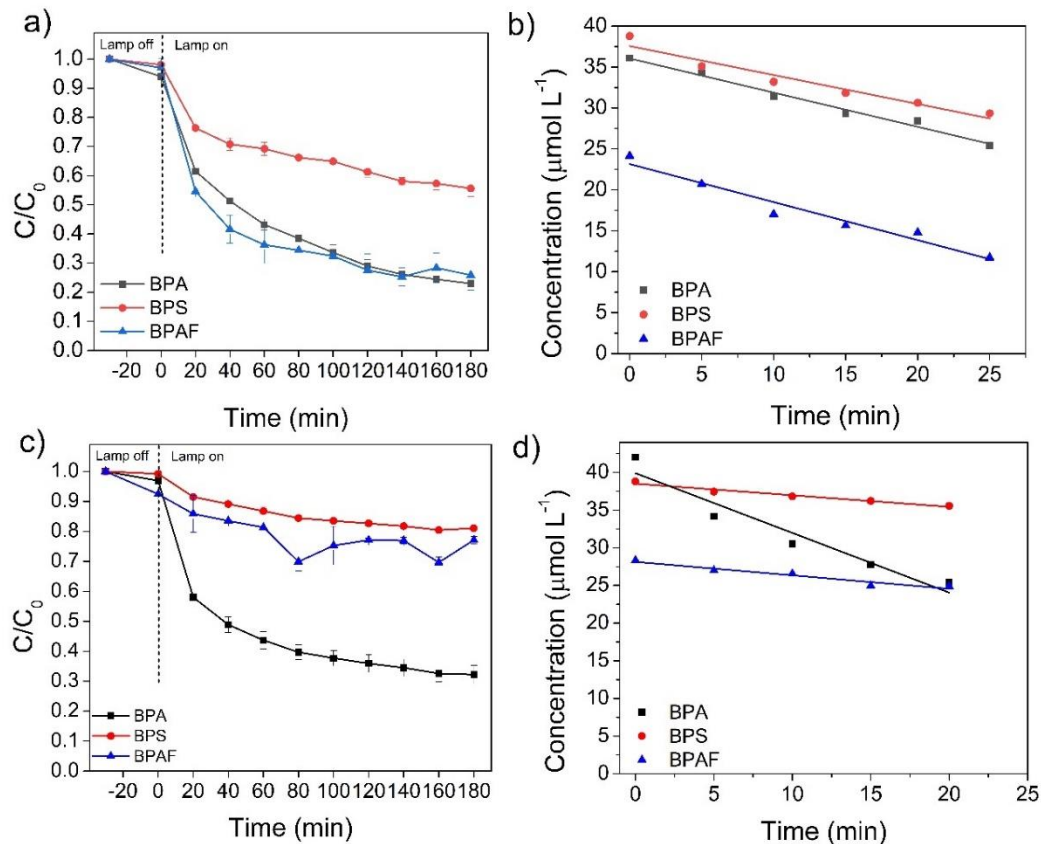


Figure 7. a) Photocatalytic degradation of BPA, BPS and BPAF, b) Initial disappearance rate of BPA, BPS and BPAF, c) photocatalytic degradation of BPA, BPS and BPAF in a multi-component solution, and d) Initial disappearance rate of BPA, BPS and BPAF in a multi-component solution. The concentration of BV-Gd-4% was 1 g L^{-1} and LED visible light irradiation was applied in all the experiments.

The stability of BV-Gd-4% was evaluated through reusability tests in which the photocatalyst was recovered and washed to be used several times consecutively. Figure 8 displays the photocatalyst degradation performance for BPA decomposition under LED visible light irradiation. As can be observed the photocatalyst efficiency on BPA decomposition decreased 29.5% after the second cycle and 48.4% after the third one. Finally, after four cycles the photocatalyst showed an efficiency of 42.15% in BPA removal. It is important to mention that the recovery of the photocatalyst was difficult, probably due to the small amount used (1 g L^{-1}). The photocatalyst loss was estimated to be $\sim 20\%$ in each cycle, which could have impacted the photocatalytic efficiency obtained [63,64]. It is also possible that the saturation of active sites on the material's surface may have contributed to the decrease in the photocatalyst efficiency [65,66]. In addition to reusability tests, the stability of the photocatalyst (BV-Gd-4%) was

assessed by measuring the concentration of dissolved metals (V, Bi, Gd) before and after photocatalytic treatment by means of ICP-OES. None of the metals analyzed were detected either before or after the photocatalytic treatment indicating that there was no leaching of metals from the BV-Gd-4%. Hence, the stability of the photocatalysts during the photocatalytic reaction was demonstrated.

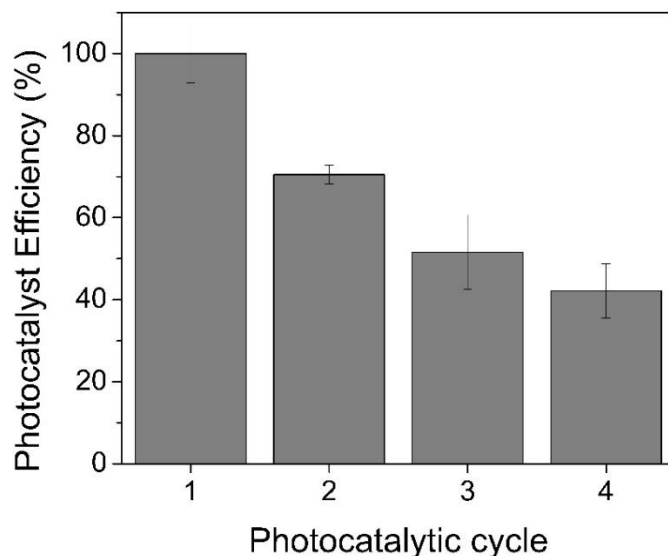


Figure 8. BV-Gd-4% reusability tests for BPA decomposition under LED visible light irradiation.

3.3 Identification of reactive species

To elucidate the photodegradation mechanism, the main reactive species involved in the photocatalytic reaction were identified by means of trapping tests. Isopropyl alcohol (IPA), Ammonium oxalate (AO), and 4-benzoquinone (BQ) were used as scavengers of hydroxyl free radicals $\cdot\text{OH}$, photo-generated holes h^+ , and superoxide radicals $\cdot\text{O}_2^-$ respectively. Figure 9 shows the BPA, BPS, and BPAF behavior in the presence of the three different scavengers. From results, it can be seen that the presence of IPA did not disturb the photolytic performance of BPA, BPS, or BPAF. Therefore, it can be inferred that $\cdot\text{OH}$ free radicals do not have an important role in the decomposition of any of the studied pollutants. Likewise, there was no significant effect on BPAF decomposition when the ammonium oxalate (AO) was added suggesting that the photo-generated h^+ does not have an important role during its decomposition. In contrast, a faster degradation was observed for BPA and BPS in the presence of AO. This suggests that the recombination of electron-hole pairs was restrained when the AO was added to the system as a scavenger to capture holes, leading to the generation of a large number of superoxide radicals ($\cdot\text{O}_2^-$) [67].

On the other hand, the inhibition of BPA and BPAF degradation in the presence of benzoquinone (BQ), indicates that superoxide radicals ($\cdot\text{O}_2$) are the main reactive species involved in photodegradation of BPA and BPAF under LED visible light irradiation. Even though benzoquinone experiments could not be performed for BPS, $\cdot\text{O}_2$ may be considered as the main reactive species as well since the BPS behavior was very similar to BPA in the presence of the other two scavengers (IPA and AO).

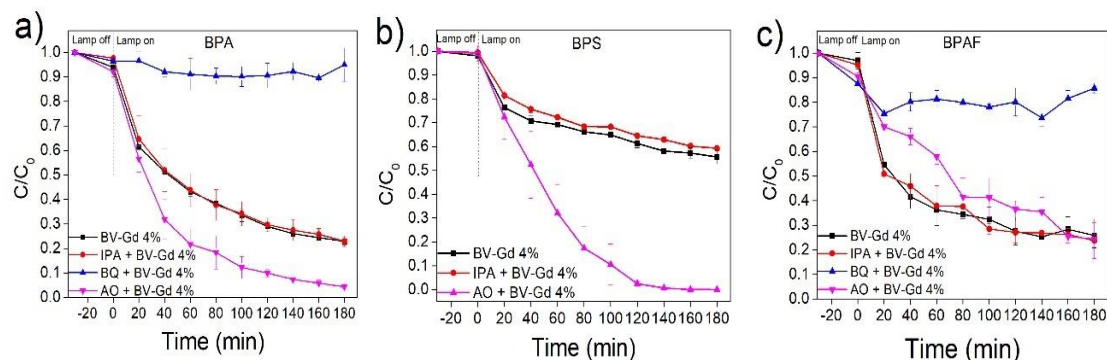
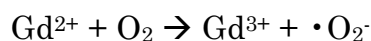
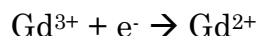


Figure 9. Trapping tests of photocatalytic decomposition of a) BPA, b) BPS, and c) BPAF in the presence of different scavengers.

3.4 Proposed mechanism

The LED visible-light irradiation promotes the generation of electron-hole pairs, during this process, Gd^{3+} positive anions present in the photocatalyst may play a role in hindering the recombination of electron-holes and increasing the efficiency of charge transfer [34,58]. This happens through a trapping-detraping mechanism in which Gd^{3+} ions trap electrons to be transferred to the oxygen molecules adsorbed onto the surface of the photocatalyst. Then, Gadolinium ions release those electrons to return to the initial state as follows:



Scavenging tests revealed that the main reactive species participating in the decomposition of BPA, BPS, and BPAF using BV-Gd-4% as a photocatalyst under visible LED light, are the superoxide radicals ($\cdot\text{O}_2$). In photocatalytic processes, these radicals are generated by means of electrons reacting with adsorbed oxygen at photocatalyst's surface as follows: $e^- + \text{O}_2 \rightarrow \cdot\text{O}_2^-$.

Considering that superoxide radicals are the main reactive species, that the three pollutants have a similar molecular structure, and taking into account previous studies, the proposed mechanism is shown in Figure 10.

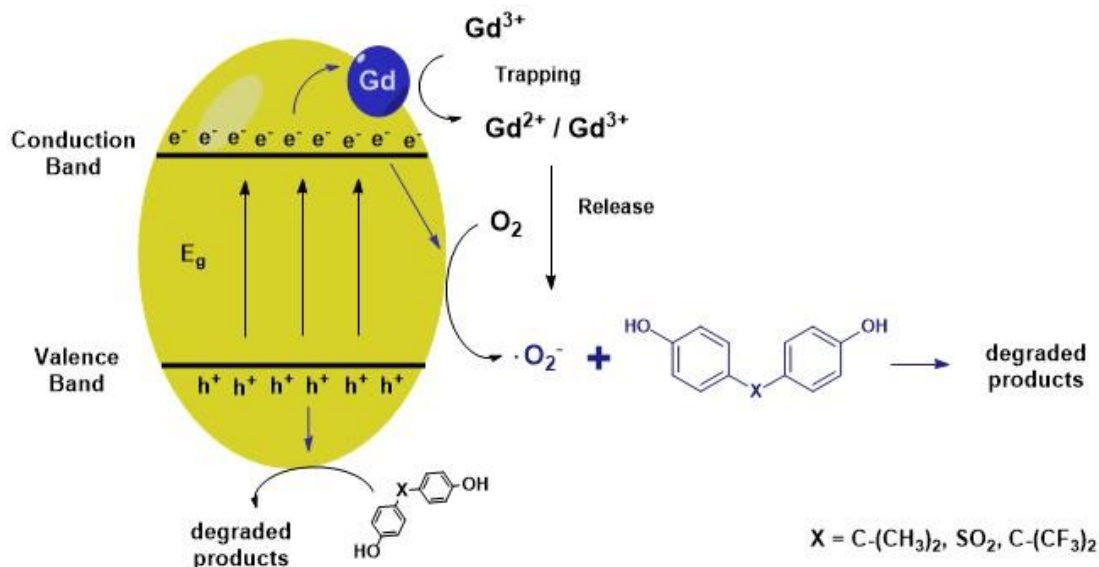


Figure 10. Proposed decomposition mechanism of BPA, BPS, and BPAF over BV-Gd-4% under LED visible light irradiation.

As it is shown in Figure 11 five main reactions have been considered in the decomposition path of the studied pollutants: (I) oxidation, (II) hydroxylation, (III) β -scission, (IV) ring cleavage, and (V) mineralization [68,69]. After the compounds (BPA, BPS, and BPAF) have formed phenoxy radicals, probably in any of their different resonance forms (R1, R2, and R3), the hydroxylation products (P1) could be generated through oxygen transfer process [70]. Afterwards, the β -scission process could be started from radicals with high electron density at para-position, and the formed radical compounds (P2, P3, P4, P5) would lead to ring-cleavage products [68]. Only if complete mineralization is achieved, CO_2 and H_2O could be obtained as final products.

Different approaches have been used to explain the two oxidative decomposition of BPA, BPS, and BPAF. Most of the studies have found similar intermediates formed during photocatalytic oxidation, for instance, phenol, p-benzoquinone, 4-isopropenylphenol, and 4-hydroxyacetophenone have been commonly reported as main BPA intermediates [13,69]. According to other studies the main by-product of BPS degradation is p-hydroxybenzenesulfonic [62,71]. On the other hand, the BPAF degradation mechanism is not being deeply studied, and as far as the authors know, there are no previous reports of BPAF removal using visible-light-driven photocatalysis.

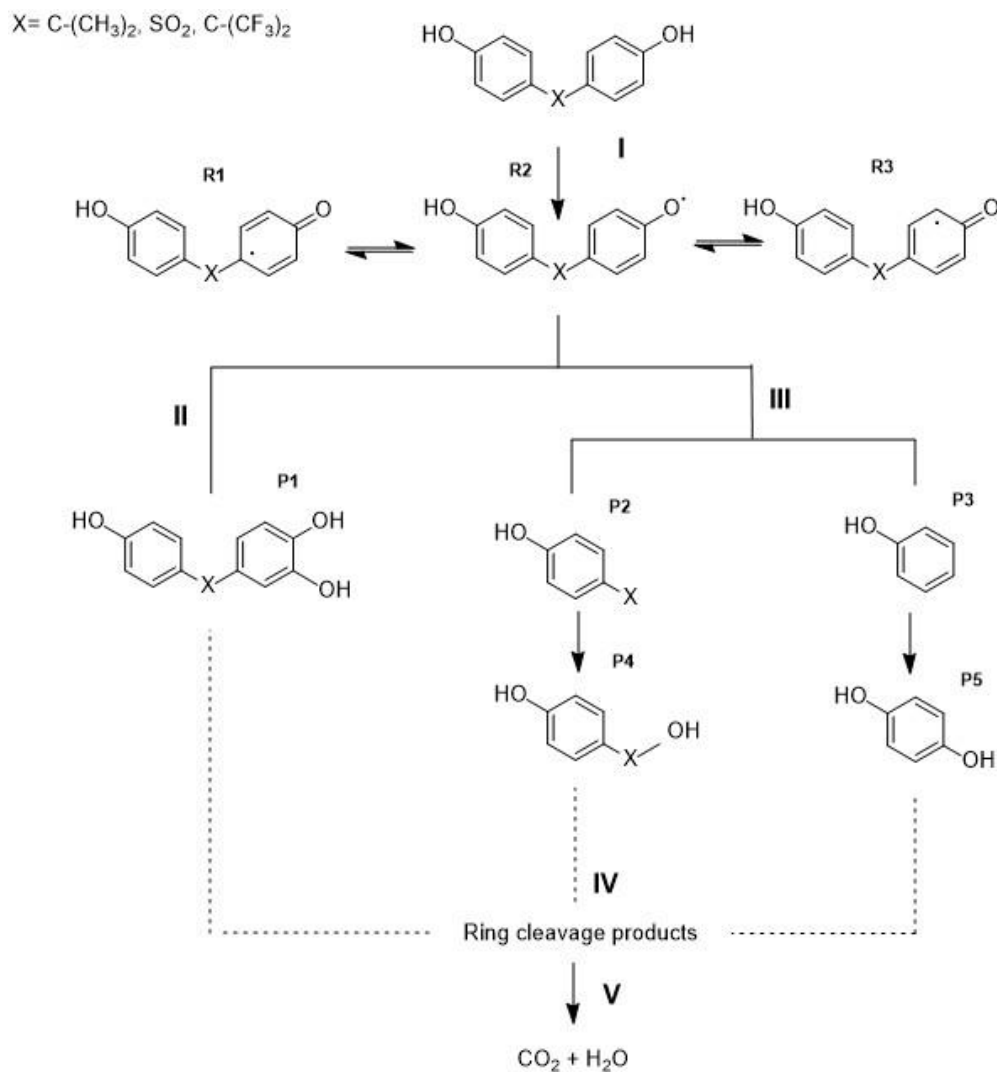


Figure 11. Proposed decomposition path of BPA, BPS, and BPAF in the presence of BV-Gd-4% under LED visible light irradiation.

4. Conclusions

Effective visible-active Gd³⁺ doped BiVO₄ was prepared by thermal synthesis. This photocatalyst was successfully used for the decomposition of organic pollutants in water under visible LED light irradiation. Concluding remarks can be summarized as follows:

- Characterization results of XRD, XPS, and Raman revealed that the BiVO₄ was successfully doped into its crystalline structure by the substitution of Gd³⁺ instead of Bi³⁺ when a high concentration of Gd³⁺ was used. Furthermore, three crystalline structures were identified in the

photocatalysts with higher Gd^{3+} content (BV-Gd-4% and BV-Gd-6%) forming a heterostructure that may promote the separation of charge carriers.

- Photocatalytic activity of the as-prepared materials was initially evaluated using bisphenol A as a test molecule. BiVO_4 doped with 4% of Gd^{3+} in molar mass proved to be the most efficient photocatalyst, reaching decomposition percentages of $77.02\% \pm 2.16$, $44.36\% \pm 2.74$, and $74.11\% \pm 5.09$ for bisphenol A, bisphenol S and Bisphenol AF, respectively (180 min, 1 g L^{-1} of photocatalyst, Vis-LED light)
- The photocatalytic efficiency was successfully improved by Gd^{3+} doping. The presence of Gd^{3+} in the photocatalyst may play a role in hindering the recombination of electron-holes and increasing the efficiency of charge transfer.
- Superoxide radicals ($\cdot\text{O}_2^-$) were found to be the main reactive species involved in photodegradation of BPA, BPS, and BPAF.
- No dissolved metals (Bi, V, or Gd) were detected either before or after photocatalytic experiments. This suggests that BV-Gd-4% has good stability and that there will be no leaching of toxic metals.
- Based on obtained results it can be inferred that BV-Gd-4% is a promising alternative for photocatalytic treatment using visible LED lamps for the removal of organic pollutants from water.

5. References

- [1] N.H. Tran, M. Reinhard, K.Y.-H. Gin, Occurrence and fate of emerging contaminants in municipal wastewater treatment plants from different geographical regions-a review, *Water Res.* 133 (2018) 182–207. doi:10.1016/J.WATRES.2017.12.029.
- [2] R. Naidu, V.A. Arias Espana, Y. Liu, J. Jit, Emerging contaminants in the environment: Risk-based analysis for better management, *Chemosphere.* 154 (2016) 350–357. doi:10.1016/j.chemosphere.2016.03.068.
- [3] D. Chen, K. Kannan, H. Tan, Z. Zheng, Y.-L. Feng, Y. Wu, M. Widelka, Bisphenol Analogues Other Than BPA: Environmental Occurrence, Human Exposure, and Toxicity-A Review, *Environ. Sci. Technol.* 50 (2016) 5438–5453. doi:10.1021/acs.est.5b05387.
- [4] S. Esplugas, D.M. Bila, L.G.T. Krause, M. Dezotti, Ozonation and advanced oxidation technologies to remove endocrine disrupting chemicals (EDCs) and pharmaceuticals and personal care products (PPCPs) in water effluents., *J. Hazard. Mater.* 149 (2007) 631–42. doi:10.1016/j.jhazmat.2007.07.073.
- [5] N. Bolong, A.F. Ismail, M.R. Salim, T. Matsuura, A review of the effects of emerging contaminants in wastewater and options for their removal, *Desalination.* 239 (2009) 229–246. doi:10.1016/j.desal.2008.03.020.
- [6] K. Pivnenko, G.A. Pedersen, E. Eriksson, T.F. Astrup, Bisphenol A and its structural analogues in household waste paper, *Waste Manag.* 44 (2015) 39–47. doi:10.1016/J.WASMAN.2015.07.017.
- [7] I.Y. López-Pacheco, A. Silva-Núñez, C. Salinas-Salazar, A. Arévalo-Gallegos, L.A. Lizarazo-Holguin, D. Barceló, H.M.N. Iqbal, R. Parra-Saldívar, Anthropogenic contaminants of high concern: Existence in water resources and their adverse effects, *Sci. Total Environ.* 690 (2019) 1068–1088. doi:10.1016/j.scitotenv.2019.07.052.
- [8] H.R. Dhaini, R.M. Nassif, Exposure assessment of endocrine disruptors in bottled drinking water of Lebanon, *Environ. Monit. Assess.* 186 (2014) 5655–5662. doi:10.1007/s10661-014-3810-x.
- [9] S.A. Baluka, W.K. Rumbeiha, Bisphenol A and food safety: Lessons from developed to developing countries, *Food Chem. Toxicol.* 92 (2016) 58–63. doi:10.1016/j.fct.2016.03.025.
- [10] D.G. Skledar, A. Carino, J. Trontelj, J. Troberg, E. Distrutti, S. Marchianò, T. Tomašič, A. Zega, M. Finel, S. Fiorucci, L.P. Mašič, Endocrine activities and

adipogenic effects of bisphenol AF and its main metabolite, *Chemosphere*. 215 (2019) 870–880. doi:10.1016/j.chemosphere.2018.10.129.

[11] Y. Hu, Q. Zhu, X. Yan, C. Liao, G. Jiang, Occurrence, fate and risk assessment of BPA and its substituents in wastewater treatment plant: A review, *Environ. Res.* 178 (2019). doi:10.1016/j.envres.2019.108732.

[12] M.R.D. Khaki, M.S. Shafeeyan, A.A.A. Raman, W.M.A.W. Daud, Application of doped photocatalysts for organic pollutant degradation - A review, *J. Environ. Manage.* 198 (2017) 78–94. doi:10.1016/J.JENVMAN.2017.04.099.

[13] P.V.L. Reddy, K.-H. Kim, B. Kavitha, V. Kumar, N. Raza, S. Kalagara, Photocatalytic degradation of bisphenol A in aqueous media: A review, *J. Environ. Manage.* 213 (2018) 189–205. doi:10.1016/J.JENVMAN.2018.02.059.

[14] B. Tryba, S. Jafari, M. Sillanpää, A. Nitta, B. Ohtani, A.W. Morawski, Influence of TiO₂ structure on its photocatalytic activity towards acetaldehyde decomposition, *Appl. Surf. Sci.* 470 (2019) 376–385. doi:10.1016/j.apsusc.2018.11.137.

[15] L. V. Bora, R.K. Mewada, Visible/solar light active photocatalysts for organic effluent treatment: Fundamentals, mechanisms and parametric review, *Renew. Sustain. Energy Rev.* 76 (2017) 1393–1421. doi:10.1016/j.rser.2017.01.130.

[16] R.B.P. Marcelino, C.C. Amorim, Towards visible-light photocatalysis for environmental applications: band-gap engineering versus photons absorption-a review, *Environ. Sci. Pollut. Res.* 26 (2019) 4155–4170. doi:10.1007/s11356-018-3117-5.

[17] S. Malato, P. Fernández-Ibáñez, M.I. Maldonado, J. Blanco, W. Gernjak, Decontamination and disinfection of water by solar photocatalysis: Recent overview and trends, *Catal. Today.* 147 (2009) 1–59. doi:10.1016/j.cattod.2009.06.018.

[18] W. Jo, R.J. Tayade, New Generation Energy-Efficient Light Source for Photocatalysis: LEDs for Environmental Applications, *Ind. Eng. Chemistry Res.* 53 (2014) 2073–2084.

[19] I. Levchuk, J.J. Rueda-Márquez, S. Suihkonen, M.A. Manzano, M. Sillanpää, Application of UVA-LED based photocatalysis for plywood mill wastewater treatment, *Sep. Purif. Technol.* 143 (2015) 1–5. doi:10.1016/J.SEPPUR.2015.01.007.

[20] Z. Wang, G. Nguyen Song Thuy Thuy, V. Srivastava, I. Ambat, M. Sillanpää, Photocatalytic degradation of an artificial sweetener (Acesulfame-K)

from synthetic wastewater under UV-LED controlled illumination, *Process Saf. Environ. Prot.* 123 (2019) 206–214. doi:10.1016/j.psep.2019.01.018.

[21] E.M. Siedlecka, Application of Bismuth-Based Photocatalysts in Environmental Protection, in: Inamuddin, A. Asiri, E. Lichtfouse (Eds.), *Nanophotocatalysis Environ. Appl. Environ. Chem. a Sustain. World*, Springer Cham, Switzerland, 2020: pp. 87–118. doi:10.1007/978-3-030-12619-3_4.

[22] X. Meng, Z. Zhang, Bismuth-based photocatalytic semiconductors: Introduction, challenges and possible approaches, *J. Mol. Catal. A Chem.* 423 (2016) 533–549. doi:10.1016/j.molcata.2016.07.030.

[23] R. He, S. Cao, P. Zhou, J. Yu, Recent advances in visible light Bi-based photocatalysts, *Chinese J. Catal.* 35 (2014) 989–1007. doi:10.1016/s1872-2067(14)60075-9.

[24] A. Malathi, J. Madhavan, M. Ashokkumar, P. Arunachalam, A review on BiVO₄ photocatalyst: Activity enhancement methods for solar photocatalytic applications, *Appl. Catal. A Gen.* 555 (2018) 47–74. doi:10.1016/j.apcata.2018.02.010.

[25] O. Monfort, G. Plesch, Bismuth vanadate-based semiconductor photocatalysts: a short critical review on the efficiency and the mechanism of photodegradation of organic pollutants, *Environ. Sci. Pollut. Res.* 25 (2018) 19362–19379.

[26] K. Zhang, J. Deng, Y. Liu, S. Xie, H. Dai, Photocatalytic Removal of Organics over BiVO₄-Based Photocatalysts, in: *Semicond. Photocatal. - Mater. Mech. Appl.*, InTech, 2016. doi:10.5772/62745.

[27] H. bin LI, J. ZHANG, G. you HUANG, S. hao FU, C. MA, B. yu WANG, Q. ru HUANG, H. wei LIAO, Hydrothermal synthesis and enhanced photocatalytic activity of hierarchical flower-like Fe-doped BiVO₄, *Trans. Nonferrous Met. Soc. China (English Ed.)* 27 (2017) 868–875. doi:10.1016/S1003-6326(17)60102-X.

[28] C. Regmi, Y.K. Kshetri, R.P. Pandey, T.-H. Kim, G. Gyawali, S.W. Lee, Understanding the multifunctionality in Cu-doped BiVO₄ semiconductor photocatalyst, *J. Environ. Sci.* 75 (2019) 84–97. doi:10.1016/J.JES.2018.03.005.

[29] L.W. Shan, G.L. Wang, J. Suriyaprakash, D. Li, L.Z. Liu, L.M. Dong, Solar light driven pure water splitting of B-doped BiVO₄ synthesized via a sol-gel method, *J. Alloys Compd.* 636 (2015) 131–137. doi:10.1016/j.jallcom.2015.02.113.

[30] Z. Zhao, H. Dai, J. Deng, Y. Liu, C.T. Au, Effect of sulfur doping on the photocatalytic performance of BiVO₄ under visible light illumination, *Cuihua*

Xuebao/Chinese J. Catal. 34 (2013) 1617–1626. doi:10.1016/S1872-2067(12)60632-9.

[31] S. Obregón, G. Colón, On the origin of the photocatalytic activity improvement of BiVO₄ through rare earth tridoping, *Appl. Catal. A Gen.* 501 (2015) 56–62. doi:10.1016/j.apcata.2015.04.032.

[32] X. Luo, G. Zhu, J. Peng, X. Wei, M. Hojamberdiev, L. Jin, P. Liu, Enhanced photocatalytic activity of Gd-doped porous β -Bi₂O₃ photocatalysts under visible light irradiation, *Appl. Surf. Sci.* 351 (2015) 260–269. doi:10.1016/j.apsusc.2015.05.137.

[33] X. Gao, Z. Wang, X. Zhai, F. Fu, W. Li, The synthesise of lanthanide doped BiVO₄ and its enhanced photocatalytic activity, *J. Mol. Liq.* 211 (2015) 25–30. doi:10.1016/J.MOLLIQ.2015.06.058.

[34] H. Xu, C. Wu, H. Li, J. Chu, G. Sun, Y. Xu, Y. Yan, Synthesis, characterization and photocatalytic activities of rare earth-loaded BiVO₄ catalysts, *Appl. Surf. Sci.* 256 (2009) 597–602. doi:10.1016/j.apsusc.2009.05.102.

[35] Y. Luo, G. Tan, G. Dong, H. Ren, A. Xia, A comprehensive investigation of tetragonal Gd-doped BiVO₄ with enhanced photocatalytic performance under sun-light, *Appl. Surf. Sci.* 364 (2016) 156–165. doi:10.1016/j.apsusc.2015.12.100.

[36] X. Yan, T. Ohno, K. Nishijima, R. Abe, B. Ohtani, Is methylene blue an appropriate substrate for a photocatalytic activity test? A study with visible-light responsive titania, *Chem. Phys. Lett.* 429 (2006) 606–610. doi:10.1016/J.CPLETT.2006.08.081.

[37] W. Yin, W. Wang, M. Shang, L. Zhou, S. Sun, L. Wang, BiVO₄ Hollow Nanospheres: Anchoring Synthesis, Growth Mechanism, and Their Application in Photocatalysis, *Eur. J. Inorg. Chem.* (2009) 4379–4384. doi:10.1002/ejic.200900614.

[38] M. Sevilla, A.B. Fuertes, Chemical and Structural Properties of Carbonaceous Products Obtained by Hydrothermal Carbonization of Saccharides, *Chem. - A Eur. J.* 15 (2009) 4195–4203. doi:10.1002/chem.200802097.

[39] S. Obregón, S.W. Lee, G. Colón, Exalted photocatalytic activity of tetragonal BiVO₄ by Er³⁺ doping through a luminescence cooperative mechanism, *Dalt. Trans.* 43 (2014) 311–316. doi:10.1039/c3dt51923f.

[40] Y. Luo, G. Tan, G. Dong, H. Ren, A. Xia, Effects of structure, morphology, and up-conversion on Nd-doped BiVO₄ system with high photocatalytic activity, *Ceram. Int.* 41 (2015) 3259–3268. doi:10.1016/j.ceramint.2014.11.016.

- [41] T. Kansaard, W. Pecharapa, Characterization of BiVO₄ nanoparticles prepared by sonochemical process, *Ferroelectrics*. 552 (2019) 140–147. doi:10.1080/00150193.2019.1653090.
- [42] S. Kunduz, G.S. Pozan Soylu, Highly active BiVO₄ nanoparticles: The enhanced photocatalytic properties under natural sunlight for removal of phenol from wastewater, *Sep. Purif. Technol.* 141 (2015) 221–228. doi:10.1016/J.SEPPUR.2014.11.036.
- [43] C.H. Yang, Z.Q. Ma, Raman spectral analysis of TiO₂ thin films doped with rare-earth samarium, *Appl. Opt.* 51 (2012) 5438–5441. doi:10.1364/AO.51.005438.
- [44] S.K. Lakhera, R. Venkataramana, G. Mathew, H.Y. Hafeez, B. Neppolian, Fabrication of high surface area AgI incorporated porous BiVO₄ heterojunction photocatalysts, *Mater. Sci. Semicond. Process.* 106 (2020). doi:10.1016/j.mssp.2019.104756.
- [45] S. Obregón, G. Colón, Heterostructured Er³⁺-doped BiVO₄ with exceptional photocatalytic performance by cooperative electronic and luminescence sensitization mechanism, *Appl. Catal. B Environ.* 158–159 (2014) 242–249. doi:10.1016/j.apcatb.2014.04.029.
- [46] P.H. Le, N.T. Kien, C.N. Van, Recent Advances in BiVO₄- and Bi₂Te₃-Based Materials for High Efficiency-Energy Applications, in: *Bismuth - Adv. Appl. Defects Charact.*, InTech, 2018. doi:10.5772/intechopen.75613.
- [47] M. V. Malashchonak, E.A. Streltsov, D.A. Kuliomin, A.I. Kulak, A. V. Mazanik, Monoclinic bismuth vanadate band gap determination by photoelectrochemical spectroscopy, *Mater. Chem. Phys.* 201 (2017) 189–193. doi:10.1016/J.MATCHEMPHYS.2017.08.053.
- [48] Y. Luo, G. Tan, G. Dong, L. Zhang, J. Huang, W. Yang, C. Zhao, H. Ren, Structural transformation of Sm³⁺-doped BiVO₄ with high photocatalytic activity under simulated sun-light, *Appl. Surf. Sci.* 324 (2015) 505–511. doi:10.1016/j.apsusc.2014.10.168.
- [49] L. Zong, P. Cui, F. Qin, K. Zhao, Z. Wang, R. Yu, Heterostructured bismuth vanadate multi-shell hollow spheres with high visible-light-driven photocatalytic activity, *Mater. Res. Bull.* 86 (2017) 44–50. doi:10.1016/J.MATERRESBULL.2016.09.031.
- [50] W. Shao, H. Wang, X. Zhang, Elemental doping for optimizing photocatalysis in semiconductors, *Dalt. Trans.* 47 (2018) 12642–12646. doi:10.1039/c8dt02613k.

- [51] M. Wang, H. Zheng, Q. Liu, C. Niu, Y. Che, M. Dang, High performance B doped BiVO₄ photocatalyst with visible light response by citric acid complex method, *Spectrochim. Acta Part A Mol. Biomol. Spectrosc.* 114 (2013) 74–79. doi:10.1016/J.SAA.2013.05.032.
- [52] C. Regmi, Y.K. Kshetri, R.P. Pandey, S.W. Lee, Visible-light-driven S and W co-doped dendritic BiVO₄ for efficient photocatalytic degradation of naproxen and its mechanistic analysis, *Mol. Catal.* 453 (2018) 149–160. doi:10.1016/j.mcat.2018.05.008.
- [53] Q. Yuan, L. Chen, M. Xiong, J. He, S.L. Luo, C.T. Au, S.F. Yin, Cu₂O/BiVO₄ heterostructures: Synthesis and application in simultaneous photocatalytic oxidation of organic dyes and reduction of Cr(VI) under visible light, *Chem. Eng. J.* 255 (2014) 394–402. doi:10.1016/j.cej.2014.06.031.
- [54] K. Zhong, H. Gao, J. Feng, Y. Zhang, K. Lai, Facile synthesis of Z-scheme Se/BiVO₄ heterojunction with enhanced visible-light-driven photocatalytic performance, *J. Mater. Sci.* 54 (2019) 10632–10643. doi:10.1007/s10853-019-03634-1.
- [55] M. Mao, F. Chen, C. Zheng, J. Ning, Y. Zhong, Y. Hu, Facile synthesis of porous Bi₂O₃-BiVO₄ p-n heterojunction composite microrods with highly efficient photocatalytic degradation of phenol, *J. Alloys Compd.* 688 (2016) 1080–1087. doi:10.1016/j.jallcom.2016.07.128.
- [56] A.M. Al-Hamdi, M. Sillanpää, J. Dutta, Gadolinium doped tin dioxide nanoparticles: an efficient visible light active photocatalyst, *J. Rare Earths.* 33 (2015) 1275–1283. doi:10.1016/S1002-0721(14)60557-3.
- [57] A.W. Xu, Y. Gao, H.Q. Liu, The preparation, characterization, and their photocatalytic activities of rare-earth-doped TiO₂ nanoparticles, *J. Catal.* 207 (2002) 151–157. doi:10.1006/jcat.2002.3539.
- [58] A.P. Reverberi, P.S. Varbanov, M. Vocciante, B. Fabiano, Bismuth oxide-related photocatalysts in green nanotechnology: A critical analysis, *Front. Chem. Sci. Eng.* 12 (2018) 878–892. doi:10.1007/s11705-018-1744-5.
- [59] I. Tateishi, H. Katsumata, T. Suzuki, S. Kaneco, Visible-Light-Induced AgI/Bi₇O₉I₃ Composites with Enhanced Photocatalytic Activity, *Catal. Letters.* 147 (2017) 1503–1509. doi:10.1007/s10562-017-2059-8.
- [60] G. Wu, Y. Zhao, Y. Li, F. Zhang, J. Zhao, Assembled and isolated Bi₅O₇I nanowires with good photocatalytic activities, *CrystEngComm.* 19 (2017) 2113–2125. doi:10.1039/c7ce00439g.

- [61] T. Yan, M. Sun, H. Liu, T. Wu, X. Liu, Q. Yan, W. Xu, B. Du, Fabrication of hierarchical BiOI/Bi₂MoO₆ heterojunction for degradation of bisphenol A and dye under visible light irradiation, *J. Alloys Compd.* 634 (2015) 223–231. doi:10.1016/j.jallcom.2015.02.064.
- [62] Z. Fang, Y. Gao, X. Wu, X. Xu, A.K. Sarmah, N. Bolan, B. Gao, S.M. Shaheen, J. Rinklebe, Y.S. Ok, S. Xu, H. Wang, A critical review on remediation of bisphenol S (BPS) contaminated water: Efficacy and mechanisms, *Crit. Rev. Environ. Sci. Technol.* (2019) 1–47. doi:10.1080/10643389.2019.1629802.
- [63] S.O. Ganiyu, M. Zhou, C.A. Martínez-Huitle, Heterogeneous electro-Fenton and photoelectro-Fenton processes: A critical review of fundamental principles and application for water/wastewater treatment, *Appl. Catal. B Environ.* 235 (2018) 103–129. doi:10.1016/J.APCATB.2018.04.044.
- [64] W.-D. Oh, L.-W. Lok, A. Veksha, A. Giannis, T.-T. Lim, Enhanced photocatalytic degradation of bisphenol A with Ag-decorated S-doped g-C₃N₄ under solar irradiation: Performance and mechanistic studies, *Chem. Eng. J.* 333 (2018) 739–749. doi:10.1016/J.CEJ.2017.09.182.
- [65] B.-M. Bresolin, S. Ben Hammouda, M. Sillanpää, Methylammonium iodo bismuthate perovskite (CH₃NH₃)₃Bi₂I₉ as new effective visible light-responsive photocatalyst for degradation of environment pollutants, *J. Photochem. Photobiol. A Chem.* 376 (2019) 116–126. doi:10.1016/J.JPHOTOCHEM.2019.03.009.
- [66] D. Hou, L. Feng, J. Zhang, S. Dong, D. Zhou, T.T. Lim, Preparation, characterization and performance of a novel visible light responsive spherical activated carbon-supported and Er³⁺:YFeO₃-doped TiO₂ photocatalyst, *J. Hazard. Mater.* 199–200 (2012) 301–308. doi:10.1016/j.jhazmat.2011.11.011.
- [67] T. Liu, L. Wang, X. Lu, J. Fan, X. Cai, B. Gao, R. Miao, J. Wang, Y. Lv, Comparative study of the photocatalytic performance for the degradation of different dyes by ZnIn₂S₄: adsorption, active species, and pathways, *RSC Adv.* 7 (2017) 12292–12300. doi:10.1039/C7RA00199A.
- [68] T. Yang, L. Wang, Y. Liu, Z. Huang, H. He, X. Wang, J. Jiang, D. Gao, J. Ma, Comparative study on ferrate oxidation of BPS and BPAF: Kinetics, reaction mechanism, and the improvement on their biodegradability, *Water Res.* 148 (2019) 115–125. doi:10.1016/j.watres.2018.10.018.
- [69] Y. Ding, P. Zhou, H. Tang, Visible-light photocatalytic degradation of bisphenol A on NaBiO₃ nanosheets in a wide pH range: A synergistic effect between photocatalytic oxidation and chemical oxidation, *Chem. Eng. J.* 291 (2016) 149–160. doi:10.1016/j.cej.2016.01.105.

[70] J. Li, S.Y. Pang, Y. Zhou, S. Sun, L. Wang, Z. Wang, Y. Gao, Y. Yang, J. Jiang, Transformation of bisphenol AF and bisphenol S by manganese dioxide and effect of iodide, *Water Res.* 143 (2018) 47–55. doi:10.1016/j.watres.2018.06.029.

[71] X. Wang, J. Ma, Z. Wang, R. Guo, X. Hu, Aqueous phototransformation of bisphenol S: the competitive radical-attack pathway to p-hydroxybenzenesulfonic acid, *Water Sci. Technol.* 70 (2014) 540–547. doi:10.2166/wst.2014.257.

Chapter 5

Removal of pharmaceutically active compounds and bacteria inactivation from urban wastewater effluents by UVA-LED photocatalysis with Gd³⁺ doped BiVO₄

This Chapter has been published as:

C. Orona-Návar, I. Levchuk, J. Moreno-Andrés, Y. Park, A. Mikola, J. Mahlknecht, M. Sillanpää, N. Ornelas-Soto, Removal of pharmaceutically active compounds (PhACs) and bacteria inactivation from urban wastewater effluents by UVA-LED photocatalysis with Gd³⁺ doped BiVO₄, *J. Environ. Chem. Eng.* 8 (2020). doi:10.1016/j.jece.2020.104540.

1. Introduction.

In the last few decades, the presence of pharmaceutically active compounds (PhACs) in the environment has gained attention due to the known negative effects that these chemical compounds may cause to ecosystems and human health. PhACs have been recurrently detected at low concentrations (ng L^{-1} - $\mu\text{g L}^{-1}$) in the effluents of wastewater treatment plants [1,2] as well as in recipient water bodies [3,4]. Potentially harmful contaminants such as macrolide antibiotics (e.g. erythromycin, clarithromycin, azithromycin), 17- α -ethinylestradiol, amoxicillin, and ciprofloxacin among others, are included in the surface water Watch List Directive 2018/840/EU to be carefully monitored by member states of the European Union [5]. The conventional wastewater treatment processes (e.g. activated sludge, filtration, and disinfection) are not efficient enough in PhACs removal [1,6]. Therefore, effluent discharges from wastewater treatment plants (WWTP) have been identified as important anthropogenic sources of PhACs [7,8]. In addition to effective PhACs removal, the efficient elimination of pathogens from water is very important in order to prevent the transmission of diseases by contaminated water. UV light, chlorination, and ozonation have been widely used as effective methods for water disinfection, however, the formation of toxic by-products is a major drawback [9].

The development and implementation of advanced treatment processes have arisen to complement the conventional treatment methods to achieve greater efficiency in the disinfection and elimination of PhACs from urban wastewater effluents. Advanced oxidation processes (AOPs) have proven to be an effective approach to this problem. Specifically, heterogeneous photocatalysis through the generation of reactive oxygen species (e.g. $\cdot\text{OH}$, $\cdot\text{O}_2^-$) achieves the degradation of PhACs [6,7,10]. The inactivation of bacteria using photocatalytic processes has also been widely demonstrated [9,11].

Different photocatalysts have been used for those purposes, among them, TiO_2 has been considered an excellent photocatalyst because it has desirable characteristics such as chemical stability, and low costs [12]. However, the wide band gap of TiO_2 (3.2 eV) limits its photocatalytic response to the UV region of the light spectrum, which represents about 3 to 5% of the solar spectrum [13]. Therefore, the need has arisen to study photocatalysts that, besides being effective under UV light ($100 < \lambda < 400 \text{ nm}$), show good photocatalytic activity under visible light ($\lambda > 400 \text{ nm}$) [13]. Such photocatalysts will lead to the implementation of more sustainable technologies that take advantage of most of the solar spectrum for both disinfection and removal of PhACs from water [14,15]. To overcome drawbacks of solar technologies, such as limitation of

daylight hours, large areas needed and high installation costs, the use of different types of lamps has been widely investigated and currently they are the most common light source used in photocatalytic processes instead of using direct solar irradiation [16,17]. Special attention has been directed to light-emitting diodes (LED) lamps since, from the green chemistry point of view, the use of conventional UV light sources constitutes an environmental problem arising at the step of the utilization of lamps containing hazardous mercury. Light-emitting diodes (LED) could be an eco-friendly alternative for traditional UV irradiation sources since they do not contain toxic elements such as mercury. It should be noted that in comparison with conventional UV lamps, high power LED are more expensive but show longer life time (up to 100,000 h) and better resistance to mechanical impact, also they are more energy efficient and have a compact size [16,18].

Among photocatalysts, bismuth vanadate (BiVO_4) has shown excellent visible and UVA (315 – 400 nm) adsorption [19,20]. This wide-range absorption makes it a photocatalyst with potential for use both in disinfection, taking advantage of UV absorption, as well as in the photocatalytic degradation of PhACs, taking advantage of the UV-Vis adsorption range, whether the radiation comes from a lamp or directly from the sun [15,21–23]. Moreover, it has been proved that BiVO_4 can significantly enhance its photocatalytic activity through rare-earths doping for both removal of organic pollutants and bacteria inactivation [24–26]. For instance, drastically greater photocatalytic performance of Er^{3+} and Y^{3+} doped BiVO_4 compared to pristine BiVO_4 for *Escherichia coli* inactivation and methanol oxidation in deionized water under UV-Vis irradiation have been reported [27]. Gadolinium (Gd^{3+}) has demonstrated superior results in improving the activity of various photocatalysts (e.g. SnO_2 , TiO_2 , and Bi_2O_3) [25,28,29]. This may be due to its electronic structure with a partially occupied “d” and “f” orbitals that facilitates the formation of complexes promoting the adsorption of the contaminants on the surface of the photocatalyst [30]. Despite the superior photocatalytic efficiencies reported for the rare earth doped BiVO_4 compared to un-doped BiVO_4 , their performance in real wastewater effluent for PhACs removal and bacteria inactivation has been scarcely studied [31]. In addition, recent studies highlight the critical importance of assessment of heterogeneous photocatalysis under realistic water matrices, which could avoid misleading conclusions of its applicability [32,33].

Herein, the photocatalytic efficiency of Gd^{3+} doped BiVO_4 was evaluated through the degradation of 22 different PhACs detected in real urban wastewater effluent. The effect of the photocatalyst load was also investigated. Moreover,

photocatalytic inactivation of Total coliforms, *Escherichia coli*, Enterococci, and *Klebsiella pneumoniae* that were naturally present in the wastewater effluent was assessed using a UVA-LED lamp as irradiation source.

2. Materials and Methods.

2.1. Chemicals

All chemicals used were analytical grade reagents. Bismuth (III) nitrate pentahydrate ($\text{Bi}(\text{NO}_3)_3 \cdot 5\text{H}_2\text{O}$), ammonium metavanadate (NH_4VO_3), Gadolinium (III) chloride hexahydrate ($\text{GdCl}_3 \cdot 6\text{H}_2\text{O}$), ethylene glycol, α -D-Glucose, and diclofenac were purchased from Sigma-Aldrich and were used without further purification. HPLC grade solvents were used for chromatographic analysis. The HPLC grade methanol was purchased from Scharlau (Spain). The cartridges for solid phase extraction (Oasis HLB 200 mg) were received from Waters Chromatography Europe BV. Analytical standards of measured pharmaceuticals were received from suppliers listed elsewhere [34].

2.2 Preparation of Gd^{3+} doped BiVO_4

Gd^{3+} doped Bismuth vanadate (BiVO_4) was prepared following a modified methodology of the thermal synthesis proposed by Yin et al. 2009 [35]. Briefly, 3 mmol of $\text{Bi}(\text{NO}_3)_3 \cdot 5\text{H}_2\text{O}$ and 3 mmol of NH_4VO_3 were dissolved in 30 mL of ethylene glycol at 60°C controlled in an oil bath. Once a clarifying solution was formed a certain amount of $\text{GdCl}_3 \cdot 6\text{H}_2\text{O}$ was added to obtain 4% of Gadolinium in molar mass. This was the optimal Gd^{3+} content according to our previous study about Gd^{3+} doped BiVO_4 in which photocatalysts using different dopant concentrations were tested through the degradation of bisphenol A in water. After the solution was vigorously stirred for 30 minutes, 400 mg of as-prepared carbonaceous template spheres were dispersed to promote the interaction of the dopant with the metal ions while they precipitated on the surface of the templates [35]. The solution was kept in the oven at 60°C for 12 hours, then the temperature was raised to 100°C and kept for another 12 hours. Afterward, the precipitate was collected, washed several times with distilled water and ethanol, and dried at 80°C overnight. The dried powder was calcined for 2 hours at 550°C using a ramp of $10^\circ\text{C min}^{-1}$. The prepared photocatalysts were denoted as 4%-Gd- BiVO_4 .

Carbonaceous template spheres were prepared by hydrothermal method as follows: 0.5 mol of α -D-Glucose was dissolved in 80 mL of pure water. The solution was placed in a 100 mL autoclave and heated at 180°C for 4.5 hours. After cooling down at room temperature, the precipitates were collected and

washed with water and ethanol several times. Finally, the product was dried at 80°C for 12 hours [36].

2.3 Characterization techniques

An X-ray powder diffractometer (PANalytical Empyrean) with Co K α radiation source ($\lambda=1.7809$ Å) at 40 kV and 30 mA was used to obtain X-ray diffraction (XRD) patterns and crystallographic information. The morphology and particle size of the as-prepared photocatalysts were observed using a scanning electron microscope (SEM, Hitachi S-4800). The N₂ sorption experiments were carried out in a TriStar II Plus and specific surface area was estimated using the Brunauer-Emmett-Teller (BET) method. The UV-Vis diffuse reflectance spectra (DRS) were determined using a UV-Vis spectrometer (Agilent Cary 5000) in the wavelength range of 250 to 800 nm using spectralon standard as reference. The surface composition and electronic states of elements present in the photocatalyst were obtained by X-ray photoelectron spectroscopy (XPS) performed on an ESCALAB 250Xi (Thermo Fisher Scientific) spectrophotometer with monochromatic Al-K α (1486.6 eV) X-ray source. Raman spectra were acquired with a Renishaw inVia Micro Raman spectrometer. Sample excitation was carried out with a 514 nm green laser. The presence of dissolved metals and rare earth (Bi, V, and Gd) was evaluated by analyzing the wastewater samples after photocatalytic tests using inductively coupled plasma optical emission spectroscopy (ICP-OES) on an Agilent 5110.

2.4 Photocatalytic experiments

2.4.1. Photocatalytic decomposition of diclofenac in ultra-pure water

In order to study the effect of 4%-Gd-BiVO₄ concentration on the rate of photocatalytic reaction, the experiments were conducted in ultra-pure water using diclofenac (DCF, initial concentration 10 mg L⁻¹) as a model contaminant. Nonsteroidal anti-inflammatory drug diclofenac was chosen as a model pollutant because it is widely used and frequently found in urban wastewater effluents [37]. All photocatalytic tests with DCF were performed in batch mode under constant stirring at ambient temperature (20 \pm 2°C) using PYREX glass Erlenmeyer flask (total volume 150 mL). Different concentrations of photocatalyst (from 0.25 to 2 g L⁻¹) were tested. Each experiment was repeated at least twice. Two identical flasks wrapped with aluminum foil (except the bottom of the flasks) were located on the top of the UVA-LED lamp ($\lambda=370$ nm, length 30 cm and widths 8 cm). The UVA LED intensity (46.5 \pm 0.6 W m⁻²) was measured on the reactor surface using UV AB Light Meter (General UV513AB).

The accumulated UVA dose (using LED) was calculated to facilitate the comparison of PhACs degradation kinetics when different experimental conditions are used in other studies. It is widely assumed that applied UV dose is obtained by multiplying the intensity by the time [6].

The volume of model DCF solution used in experiments was 100 mL. To ensure the adsorption-desorption equilibrium between photocatalyst and DCF, the model solution was stirred for 30 min in the dark. After that, the UVA-LED was turned on and samples were taken at desired time intervals. After sampling, filtration with regenerated cellulose syringe filters (0.22 μm) was performed in order to remove photocatalyst. Filtered samples were further analyzed by means of High Performance Liquid Chromatography (HPLC, UFLC Shimadzu) equipped with a UV-Vis detector (SPD-20AV) at a wavelength of 275 nm using a C-18 column (Kinetex, 5 μm , 150 x 4.6 mm). Methanol and water (0.1% formic acid) were used as a mobile phase in a volume ratio of 75:25. The isocratic mode was used with a flow rate of 1 mL min⁻¹. Adsorption (in absence of UVA LED) and photolysis (in absence of photocatalyst) experiments were conducted with DCF model solution as reference tests.

2.4.2. Photocatalytic degradation of PhACs in urban wastewater effluent

Photocatalytic experiments using wastewater effluent as a reaction medium were conducted in a volume of 110 mL. The optimal concentration of 4%-Gd-BiVO₄ photocatalyst for experiments with urban wastewater effluent was selected based on tests conducted with diclofenac in ultra-pure water (model solution). Real urban wastewater effluent was used for the following studies on photocatalytic decomposition of PhACs present in urban wastewater effluent and disinfection studies. The wastewater effluent was taken from the Viikinmäki Wastewater Treatment Plant (WWTP) located in Helsinki (Finland). This WWTP processes wastewater from Industry and households (85% of total influent) applying a method based on chemically enhanced pre-sedimentation and enhanced nitrogen removal in activated sludge and post-denitrifying filters. Samples were collected in amber glass flasks, preserved in the fridge at 4 °C, and used within the next day. The main physicochemical characteristics (Table 1) of used wastewater effluent were measured using standard methods [38]. Total Organic Carbon (TOC) measurements were performed in non-purgeable carbon (NPOC) mode by means of Shimadzu TOC-L analyzer.

Table 1. Physicochemical characterization of urban wastewater effluent.

Parameter	Concentration in effluent (unit)
BOD ₇	8.6 (mg L ⁻¹)
COD	57 (mg L ⁻¹)
TOC	22.2 (mg L ⁻¹)
Suspended Solids (SS)	6.2 (mg L ⁻¹)
Total P	0.07 (mg L ⁻¹)
Total N	6.3 (mg L ⁻¹)
NH ₄ -N	1.7 (mg L ⁻¹)
NO ₃ -N	2.0 (mg L ⁻¹)
Alkalinity	2.3 (mmol L ⁻¹)
SO ₄ ²⁻	100.6 (mg L ⁻¹)
Cl ⁻	80.6 (mg L ⁻¹)
Total iron	0.5 (mg L ⁻¹)
pH	7.2
Conductivity	70.1 (mS m ⁻¹)
Transmittance	79.2% (370 nm)

The concentration of PhACs in wastewater effluent was analysed before and after photocatalytic tests as well as after reaching adsorption equilibrium (30 min in dark before switching on the UVA LED lamp). Measurements were also performed after reference tests such as photolysis (180 min) and adsorption (210 min). Analysis of PhACs was performed as reported earlier [34]. Briefly, Solid Phase Extraction (SPE) was applied as a pretreatment method using HLB cartridges (Oasis, 200 mg). Conditioning of HLB cartridges was conducted with 8 mL of methanol and 8 mL of Milli-Q water. Consequently, samples (100 mL) were passed through cartridges. Finally, cartridges were washed with Milli-Q water (10 mL) and dried in air. Elution was performed using 10 mL of methanol. Extracts were evaporated under a nitrogen stream and reconstructed in a mixture of water and methanol (75:25). Qualification and quantification of

PhACs were conducted using Bruker EVOQ Elite (Bruker, Billerica, MA) Ultra Performance Liquid Chromatography – Triple Quadrupole Mass Spectrometry (UPLC-QqQ-MS/MS) with C-18 column (100 x 2.1 mm; particle size 2 μm) and electrospray interface. The injection volume was 10 μL and the flow rate was 0.4 mL min^{-1} in positive and negative ionization modes. The aqueous mobile phases used for measurements conducted in positive ionization mode were a mixture of 10 mmol formic acid and ammonium formate (pH 3.2), while 100% methanol was used as organic mobile phase. Aqueous mobile phases applied for analysis performed in negative ionization mode were 5 mmol ammonium acetate/ammonia (pH 8), while organic mobile phase consisted of 100% methanol. Multiple reaction monitoring (MRM) was used for data acquisition. Obtained data were processed with Bruker MS Workstation 8.1 Software.

2.4.3. Photocatalytic disinfection tests

Wild microorganisms naturally present in wastewater were selected as target bacteria. Thus, quantification of Total coliforms, *Escherichia coli* (*E. coli*), and *Enterococci* were carried out by standard plating on commercial media: Chromogenic Collinstant Agar (Scharlab) and Slanetz & Bartley Agar (Panreac). Likewise, TCBS Thiosulfate Citrate Bile Salts Sucrose Agar (Pronadisa, Condalab) was used as solid media for *Klebsiella pneumoniae* (99.6%) which was identified by the amplification and sequencing of a fragment of 16S rDNA, as explained in previous studies [39]. The plates were incubated at 30 ± 2 $^{\circ}\text{C}$ for 24 - 48 h according to the specific bacteria.

For UVA-LED based photocatalytic disinfection experiments an optimal concentration of 4%-Gd-BiVO₄ (1 g L^{-1}) was chosen based on experiments of DCF decomposition (Section 2.4.1). The volume of wastewater was 75 mL. The solution was kept in the dark for 30 min to reach adsorption-desorption equilibrium and after that, the UVA-LED lamp was turned on. Samples were withdrawn at set time intervals and the total duration of disinfection experiments was 1 h.

The analysis of surviving organisms was enumerated by the spread-plate method. At longer exposure times, larger volumes of wastewater were plated by the membrane filtration method (gridded membranes of 0.45 μm). Colony-Forming Units (CFU) concentrations from samples measured by spread-plate as well as membrane filtration techniques were in good agreement. Results were expressed as the mean microbiological concentration of each sample (three replicates), in CFU mL^{-1} . The disinfection efficiency was determined according to time–response curves where the logarithmic reduction of the survival of

microorganisms is represented. In order to quantify the disinfection performance, kinetic modeling was applied to experimental data. Log-linear approach $\text{Log}(N/N_0) = -k \cdot t$, was suitable ($R^2 \geq 0.78$ in all cases) for describing microbial inactivation curves.

3. Results and discussion.

3.1 Characterization of 4%-Gd-BiVO₄

The crystalline structure of the synthesized 4%-Gd-BiVO₄ was determined by XRD analysis. The diffraction patterns (Figure 1) showed a good fitting with the Tetragonal dreyerite BiVO₄ structure (JCPDS file 00-014-0133). Additionally, pattern matching analysis revealed the slight presence of two additional crystalline structures: monoclinic Bi_{0.95}Gd_{0.05}VO₄ (JCPDS file 00-033-0123) and Tetragonal Bi₂O₃ phase (JCPDS file 01-078-1793). The detailed XRD profile data obtained by pattern matching analysis for bare BiVO₄ and 4%-Gd-BiVO₄ have been included as supplementary information (S2, Figures S1 and S4). The presence of the three crystalline phases may induce the formation of heterostructures that promotes an efficient electron-hole pairs separation and an effective diffusion of these charge carriers towards photocatalyst's surface, improving its photocatalytic activity [40,41]. From XRD analysis it can also be inferred that the presence of Gd³⁺ ions influences the formation of the crystalline structure. Lattice parameters, unit cell volume, and the goodness of chi-square (χ^2) fitting parameter were calculated and are shown in Table 2.

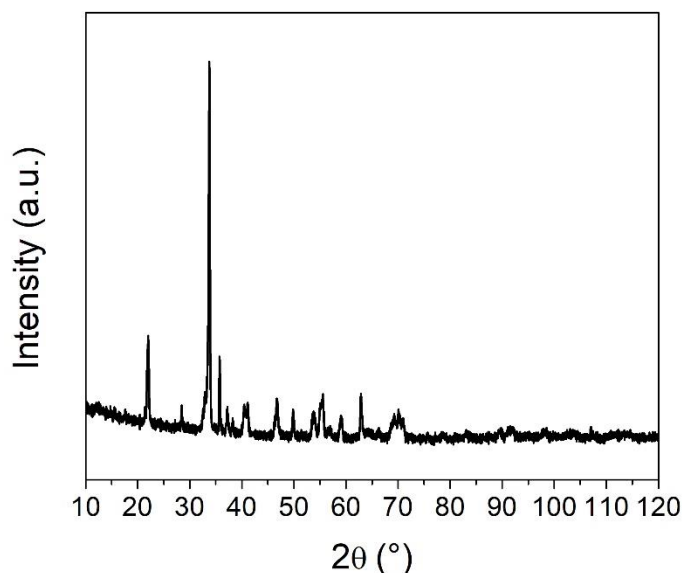


Figure 1. XRD pattern of the prepared 4%-Gd- BiVO₄

Table 2. Crystallographic parameters of 4%-Gd- BiVO₄

Material	Phases	Spatial group	Lattice Parameters			Unit cell volume (Å ³)	Chi-square (X ²)	Crystallite size (nm)
			a (Å)	B (Å)	C (Å)			
4%-Gd-BiVO ₄	*t-BiVO ₄	I41/amd	7.34745	7.34745	6.44067	347.700	1.203	89
	Bi _{0.95} Gd _{0.05} VO ₄	P21/c	5.15209	5.15210	11.74611	311.789		
	*t-Bi ₂ O ₃	P-421c	7.68477	7.68477	5.61992	331.889		

* t = tetragonal

Figure 2 shows the SEM micrograph of the as prepared photocatalyst obtained by a thermal method. Sphere and peanut-like nanoparticles randomly aggregated can be identified. It is observed that the nanoparticles were sintered during the calcination step. This particular morphology has been previously reported for pristine BiVO₄ [35,42], and most studies agree that the obtained morphology of BiVO₄ depends on the method and conditions used during the synthesis [15,43]. The average size of the nanoparticles is 89 nm, which is in agreement with the crystallite size obtained by XRD analysis.

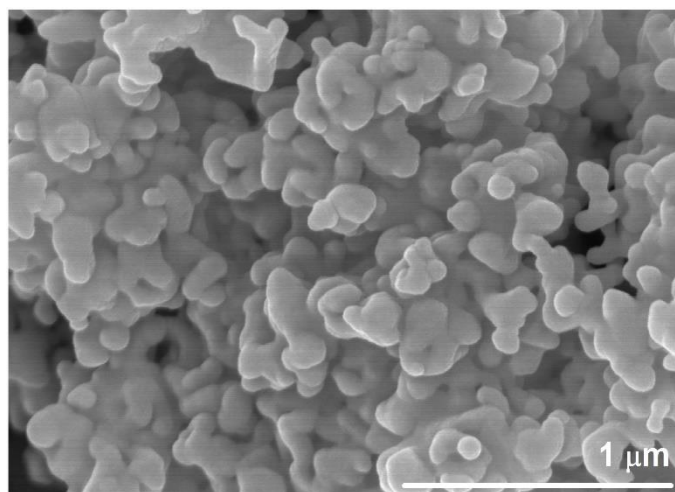


Figure 2. SEM image of the synthesized 4%-Gd-BiVO₄ photocatalyst

The surface area of pristine t-BiVO₄ has been previously reported to be in the range of 1.24 to 5 m² g⁻¹ [19]. It is known that this material generally presents a low surface area. The measured value of the BET surface area of 4%-Gd-BiVO₄ was 5.64 m² g⁻¹. Compared to pristine t-BiVO₄, the surface area of the photocatalyst surface area was not significantly increased or decreased after incorporation of Gd³⁺ ions. Therefore, the surface area may not have a significant effect on the photocatalyst performance.

The chemical species present on the synthesized photocatalyst were analyzed by means of X-ray photoelectron spectroscopy (XPS). The survey spectra are shown in Figure 3a where all the expected elements (Bi, V, O, and Gd) can be identified.

The incorporation of Gd^{3+} ions on the BiVO_4 crystalline structure was confirmed through the obtained high resolution XPS spectra of Gd 4d showing a peak at 142 eV (Figure 3e), as well as the presence of a Gd 4f and Gd 3d peaks at the survey spectra. Gadolinium probably incorporates by substitution on Bi^{3+} sites because of the smaller ionic size of Gd^{3+} (0.0938 nm) compared with Bi^{3+} (0.103 nm). The high-resolution XPS spectra of O 1s are shown in Figure 3b where the peak at 529.8 eV of binding energy can be related to the presence of O_2^- anions. Similarly, Figure 3c indicates the presence of V^{5+} according to the identified peaks at 516 and 524 eV that correspond to V $2p_{1/2}$ and V $2p_{3/2}$ orbitals respectively [44]. In Figure 3 d two symmetric peaks are shown for Bi $4f_{5/2}$ and Bi $4f_{7/2}$ at binding energies around 164 and 159 eV respectively, which are designated to Bi^{3+} chemical state [45].

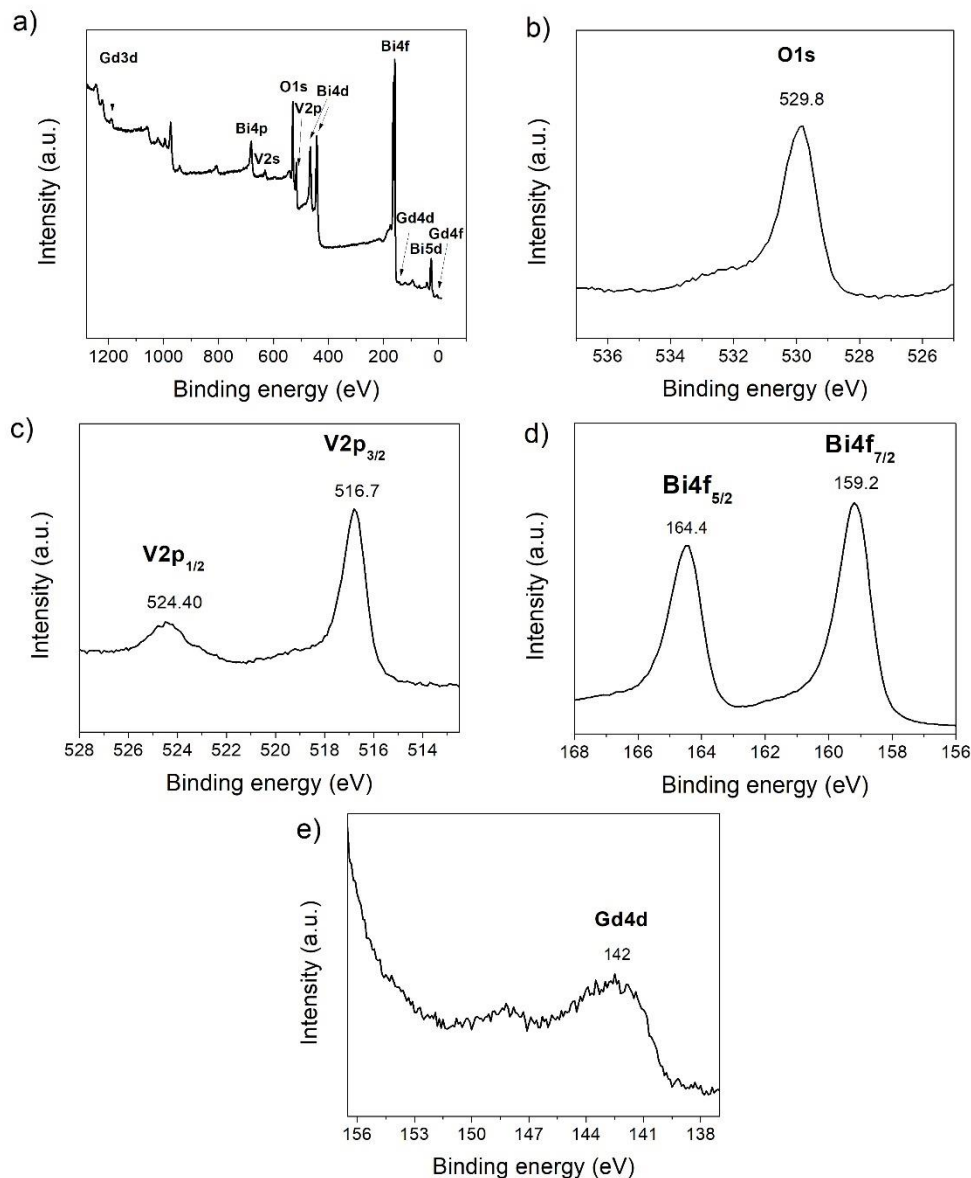


Figure 3. XPS spectra of 4%- Gd-BiVO₄ photocatalyst: (a) survey, (b) O 1s peak, (c) V 2p peaks, (d) Bi 4f peaks, and (e) Gd 4d peak

According to diffuse reflectance UV-vis spectra shown in Figure 4, 4%-Gd- BiVO₄ exhibited strong absorption in the UV-visible region. Band gap energy of the synthesized material was determined through Kubelka-Munk function (KMF), which can be expressed as shown in equation 1.

$$\text{KMF} = F(R_{\infty}) = (1 - R_{\infty})^2 / 2R_{\infty} = k/s \quad \text{Eq. (1)}$$

Where R_{∞} is the absolute reflectance of a layer with an infinite thickness, K is the absorption coefficient, and S is the scattering coefficient. KMF values were multiplied by photon energy to the power of 0.5 and plotted vs energy of the incident light. The extrapolation of the linear region (Figure 4, inset) provided a band gap of 2.46 eV for 4%-Gd-BiVO₄.

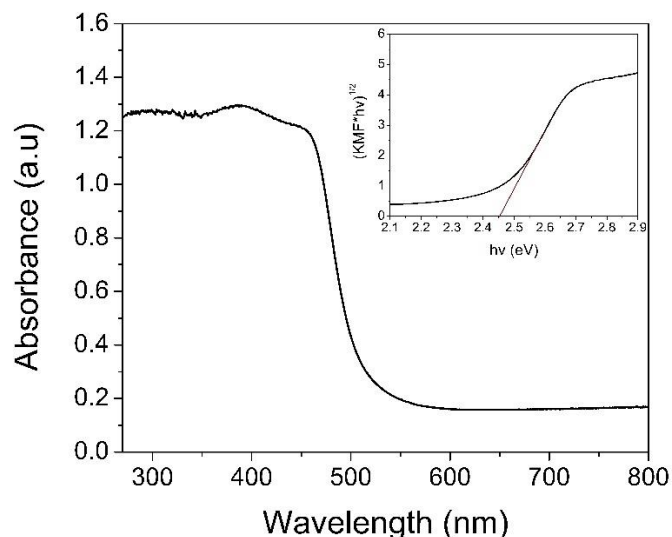


Figure 4. Diffuse reflectance UV-Vis spectra and Kubelka-Munk plot of 4%-Gd-BiVO₄.

3.2 Photocatalytic efficiency of 4%-Gd-BiVO₄

3.2.1 Effect of 4%-Gd-BiVO₄ concentration on diclofenac degradation

The effect of photocatalyst concentration on the rate of photocatalytic reaction was studied. Figure 5a shows DCF decomposition (as model compound) as a function of contact time with different 4%-Gd-BiVO₄ loadings. It is observed that the dependence of DCF concentration on the contact time follows a linear behavior in the studied time interval, indicating zero-order kinetics. The calculated initial disappearance rates for DCF degradation at different 4%-Gd-BiVO₄ loadings are shown in Figure 5b. As can be observed from Figure 5b, the photocatalyst load increases and so does the DCF initial disappearance rate. The most significant increment was observed from 0.25 g L⁻¹ to 0.5 g L⁻¹ where the initial disappearance rate was doubled from 0.256 to 0.511 $\mu\text{mol L}^{-1} \text{min}^{-1}$. Further increase of photocatalyst loading did not affect significantly the initial DCF degradation rate. It is important to notice that these tests have been done in a pure water DCF solution, however, loads as high as 2 g L⁻¹ in a real effluent could cause such turbidity that it would significantly reduce light transmission, in addition to increasing the cost. Hence, 1 g L⁻¹ was considered as an adequate

4%-Gd-BiVO₄ dose to ensure the effective absorption of photons. Also, other aspects were considered for choosing the optimal photocatalyst load, for instance, the fact that several authors have used the same photocatalyst load (1 g L⁻¹) for studying organic contaminants removal from water. This makes easier the comparison between different studies [15,43]. Moreover, it is desirable that the synthesized photocatalyst (4%-Gd-BiVO₄), in addition to removing PhACs, efficiently inactivate bacteria. Hence, studies in photocatalytic disinfection were consulted as well and considered as reference for choosing the optimal photocatalyst load. Thus, Booshehri et al., (2017) obtained the best inactivation kinetics for *E. coli*, *E. faecalis* and *F. solani* in distilled water (10 L reactor) using 1 g L⁻¹ of Ag/BiVO₄ under solar light. It is important to note that this parameter strongly depends on the type of bacteria and other experimental conditions. Finally, in accordance with the obtained results from tested conditions as well as revised literature, 1 g L⁻¹ of 4%-Gd-BiVO₄ was chosen as an optimal dose for both photocatalytic and disinfection experiments.

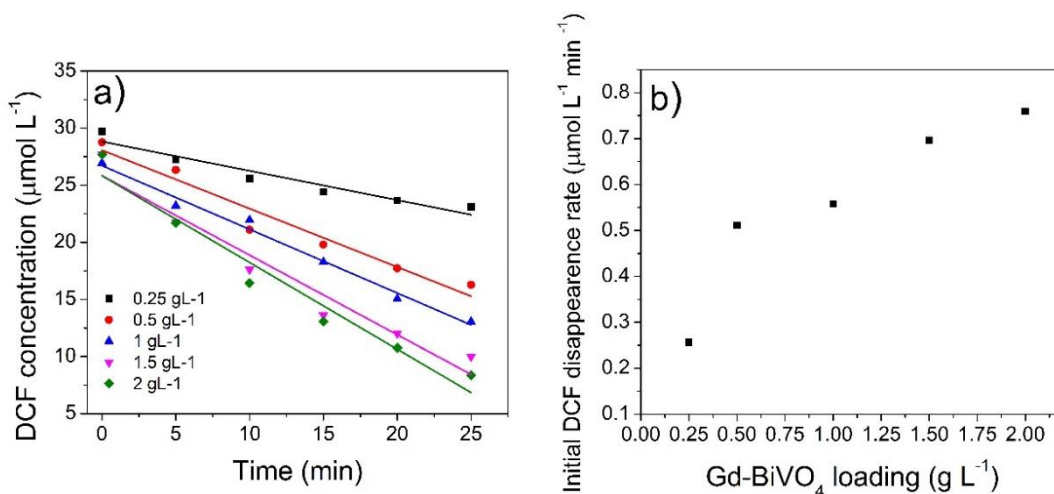


Figure 5. a) Results of DCF degradation with different loadings of 4%-Gd-BiVO₄. b) Influence of 4%-Gd-BiVO₄ loading on initial disappearance rate of DCF degradation

Figure 6 depicts the photocatalytic decomposition of DCF in model solution. Adsorption and photolysis effect can be neglected since no significant changes were observed on DCF concentration after 180 min (UVA dose = 139.5 Wh m⁻², $t_{30W} = 279 \text{ min}^{-1}$). In the presence of 4%-Gd-BiVO₄ and under UVA-LED irradiation, DCF concentration considerably decreased up to 50% in the first 20 minutes, then a slower decrease was observed until DCF disappeared almost completely (98.3%) after 120 min (UV dose: 93 Wh m⁻², $t_{30W} = 186 \text{ min}^{-1}$) using 1 g L⁻¹ of photocatalyst. Other studies are reporting similar behavior of DCF in

water [46]. For instance, Tbessi et al., (2019) achieved ~90% of DCF degradation (initial concentration of 10 mg L⁻¹) in distilled water within the first 120 min using Mn-Ag-TiO₂. Similarly, Sarasidis et al., (2014) reached 99.5% of DCF (initial concentration of 2.5 mg L⁻¹) degradation in spiked groundwater after 120 min using TiO₂. Both studies used a UVA lamp as radiation source.

Although the studies carried out in the diclofenac model solution gave us an idea of the efficiency of 4%-Gd-BiVO₄ in the degradation of organic pollutants, it cannot be assumed that the photocatalyst will behave in the same way when used in a more complex matrix. Therefore, it is important to carry out the photocatalytic study in real water matrices to have reliable evidence of photocatalysts applicability [49].

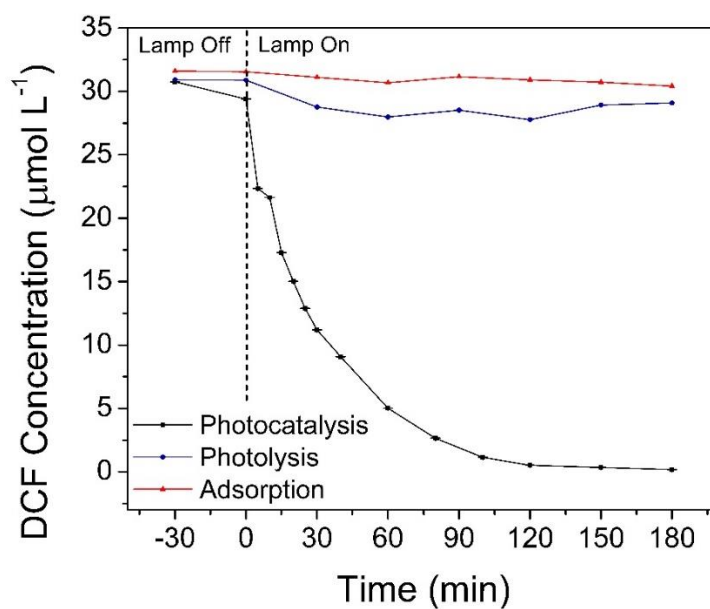


Figure 6. Photocatalytic degradation of DCF in ultra-pure water under UVA-LED irradiation (UVA dose = 139.5 Wh m⁻², t_{30W} = 279 min⁻¹) using 1 g L⁻¹ of 4%-Gd-BiVO₄.

3.2.2 Photocatalytic treatment in wastewater effluent for PhACs removal

It is of high importance to study the efficiency of novel photocatalytic materials not only using model solutions but also real wastewater [50]. Hence, photocatalytic tests were also performed using real urban wastewater effluent. Concentrations of 22 PhACs such as anti-inflammatory compounds (acetaminophen, salicylic acid, ibuprofen, naproxen, diclofenac, and ketoprofen), lipid regulator (gemfibrozil), diuretics (furosemide, hydrochlorothiazide), macrolides (azithromycin, clarithromycin), sulfonamides (sulfadiazine,

sulfamethoxazole), quinolones (ofloxacin, norfloxacin, ciprofloxacin), dihydrofolate (trimethoprim), beta-blockers (propranolol, atenolol), psychiatric

Type	Contaminant	Concentration in effluent (ng L ⁻¹)	LOD ¹ (ng L ⁻¹)	LOQ ² (ng L ⁻¹)
Anti-inflammatories	Acetaminophen	144.3 ± 29.9	0.5	1.8
	Salicylic Acid	60.6 ± 25.7	1.3	4.4
	Ibuprofen	13466.4 ± 1278.2	1	3.5
	Naproxen	2817.6 ± 75.8	0.3	0.9
	Diclofenac	2062.1 ± 201.7	0.1	0.2
	Ketoprofen	359.5 ± 21.2	0.1	0.3
Lipid Regulators	Gemfibrozil	51.0 ± 4.0	<0.1	<0.1
Diuretics	Furosemide	2291.4 ± 29.8	<0.1	<0.1
	Hydrochlorothiazide	629.9 ± 12.0	<0.1	<0.1
Macrolides	Azithromycin	892.0 ± 186.8	<0.1	<0.1
	Clarithromycin	196.4 ± 27.0	<0.1	<0.1
Sulfonamides	Sulfadiazine	33.5 ± 1.7	<0.1	<0.1
	Sulfamethoxazole	84.9 ± 2.4	<0.1	<0.1
Quinolones	Ofloxacin	967.8 ± 120.6	<0.1	<0.1
	Norfloxacin	76.1 ± 8.8	<0.1	0.1
	Ciprofloxacin	9687.2 ± 1147.6	0.1	0.2
Dihydrofolate	Trimethoprim	95.8 ± 2.2	<0.1	<0.1
Beta-blockers	Propranolol	104.5 ± 4.1	<0.1	0.1

	Atenolol	97.7 ± 3.0	<0.1	<0.1
Psychiatric drugs and stimulants	Carbamazepine	28.6 ± 0.1	<0.1	<0.1
	Caffeine	353359.8 ± 14343	0.1	0.3
To treat Asthma	Albuterol	11.8 ± 1.2	<0.1	0.1

drugs (carbamazepine, caffeine) and medicine for asthma treatment (albuterol) were measured in wastewater effluent before photocatalytic tests and results are shown in Table 3.

Table 3. A raw concentration of pharmaceutically active compounds presents in urban wastewater effluent before photocatalytic treatment.

¹ LOD = Limit of Detection

² LOQ = Limit of Quantification

Concentrations of 10 PhACs (ibuprofen, diclofenac, clarithromycin, ofloxacin, norfloxacin, propranolol, atenolol, carbamazepine, and caffeine) detected in the studied effluent were higher than the mean concentrations of these PhACs in wastewater effluents in European Union. Only four of the analyzed PhACs (acetaminophen, gemfibrozil, sulfadiazine, and sulfamethoxazole) were below mean concentration and the rest of the studied PhACs were not included in the list of the most commonly detected chemicals in European Union WWTP effluents [51].

Photocatalytic decomposition of PhACs detected in wastewater effluent was conducted using 1 g L⁻¹ of 4%-Gd- BiVO₄ according to experimental findings and literature review stated in section 3.2.1. The concentration of the 22 studied PhACs was measured before photocatalytic tests, after establishing adsorption equilibrium (30 min in the absence of UVA), and after 180 min of photocatalytic test (UVA dose = 139.5 Wh m⁻², t_{30W} = 279 min⁻¹). Moreover, a reference adsorption test was carried out in order to confirm the photocatalytic nature of pharmaceuticals decomposition. It should be stressed that some of the PhACs detected in wastewater effluent can be easily photodegraded under UVA irradiation (photolysis) [52]. Therefore, a reference photolysis test was conducted, and the decomposition of PhACs was measured. The results are shown in Figure 7.

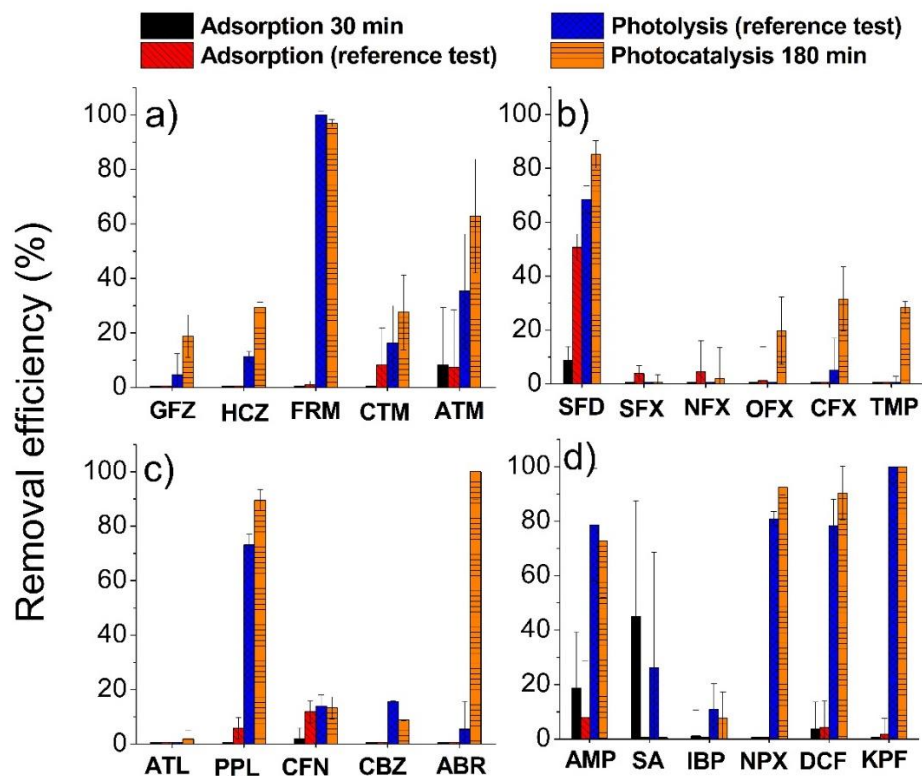


Figure 7. Removal of PhACs from urban wastewater effluent by photocatalysis (1 g L^{-1} of $4\% \text{-Gd-BiVO}_4$; UVA dose = 139.5 Wh m^{-2} , $t_{30\text{W}} = 279 \text{ min}^{-1}$), photolysis (180 min; UVA dose = 139.5 Wh m^{-2} , $t_{30\text{W}} = 279 \text{ min}^{-1}$), and adsorption (1 g L^{-1} of $4\% \text{-Gd-BiVO}_4$ in absence of light). a) Lipid regulators, diuretics and macrolides: Gemfibrozil (GFZ), Hydrochlorothiazide (HCZ), Furosemide (FRM), Clarithromycin (CTM), and Azithromycin (ATM). b) Sulfonamides, quinolones and dihydrofolate: Sulfadiazine (SFD), Sulfamethoxazole (SFX), Norfloxacin (NFX), Ofloxacin (OFX), Ciprofloxacin (CFX), and Trimethoprim (TMP). c) Beta-blockers, psychiatric drugs and stimulants to treat asthma: Atenolol (ATL), Propranolol (PPL), Caffeine (CFN), Carbamazepine (CBZ), and Albuterol (ABR). d) Anti-inflammatories: Acetaminophen (AMP), Salicylic Acid (SA), Ibuprofen (IBP), Naproxen (NPX), Diclofenac (DCF), and Ketoprofen (KPF).

The removal efficiencies of the studied PhACs varied from negative to 100% removal depending on the compound. The apparent negative removal efficiencies probably resulted from the transformation of the conjugated forms into the original parent compounds during treatment [1]. For the purpose of this study, all the negative efficiencies were considered as zero. As observed in Figure 7a poor photocatalytic removal efficiency was observed for lipid regulator gemfibrozil (18.9%), while negligible and null elimination was observed after photolysis and adsorption tests. Removal of diuretics did not follow a similar

pathway. Hence, high removal efficiency of furosemide was observed after photocatalysis (97%) and photolysis (100%), while hydrochlorothiazide showed poor removal after photocatalytic treatment (29.4%) and photolytic treatment (11.3%). Adsorption leads to negligible or null elimination of diuretics from wastewater effluent.

Macrolides detected in wastewater effluent, namely azithromycin and clarithromycin are compounds included to the second the Watch List (Directive 2018/840/EU). Under applied experimental conditions (180 min of contact time; UVA dose = 139.5 Wh m^{-2} , $t_{30W} = 279 \text{ min}^{-1}$), poor and moderate photocatalytic removal efficiencies were achieved for clarithromycin (27.5%) and azithromycin (62.9%). It should be mentioned that the removal efficiency of the two macrolides was about twice higher when photocatalysis was used as compared to photolysis.

Sulfonamides detected in wastewater effluent behaved in different ways during photocatalytic treatment (Figure 7b). High photocatalytic removal efficiency was observed for sulfadiazine (85.1%) while sulfamethoxazole showed 0% removal. Similarly, after photolysis moderate removal was achieved for sulfadiazine (68.5%) and 0% for sulfamethoxazole. Poor removal efficiencies were observed during photocatalysis for all detected quinolones, among which ciprofloxacin is a compound included in the second Watch List (Directive 2018/840/EU). Photolysis and adsorption led to negligible elimination of quinolones. Interestingly, complete photolytic elimination of ciprofloxacin was reported in earlier studies [52], while in this study about 5% of removal was observed. However, these results can be attributed to differences in irradiation sources and received UV doses. Trimethoprim also showed poor photocatalytic decomposition (28.3%) and negligible or null elimination after photolysis and adsorption.

As it is shown in Figure 7c, a difference in the behavior of detected beta-blockers was observed during photocatalytic tests. For instance, high photocatalytic removal efficacy was achieved for propranolol (89.5%), while this value was negligible for atenolol (2%). 0% removal was achieved after photolysis for atenolol and high removal was observed for propranolol (73.1%), which is in agreement with results reported by Baena-Nogueras et al., (2017). For such compounds as caffeine and carbamazepine poor removal efficiencies were achieved after photocatalytic treatment, while similar or slightly higher elimination was observed after photolysis. These results are in agreement with an earlier study [52], in which carbamazepine (initial concentration 100 ng L^{-1}) was not eliminated by photolysis. Complete removal of albuterol (asthma treatment) was observed after the photocatalytic test (180 min of contact time;

UVA dose = 139.5 Wh m⁻², t_{30W} = 279 min⁻¹), while photolysis and adsorption led to negligible and null elimination of this compound. These results are in agreement with a study by Baena-Nogueras et al., (2017), in which photolysis did not lead to the removal of albuterol from water.

As can be seen from the Figure 7d anti-inflammatories were removed with high (80 – 100 %; naproxen, diclofenac and ketoprofen), moderate (40 – 70 %; acetaminophen), poor (< 30 %; ibuprofen) and null (0%; salicylic acid) efficiency by photocatalysis (180 min of contact time; UVA dose = 139.5 Wh m⁻², t_{30W} = 279 min⁻¹). It is important to mention that moderate and high removal efficiencies were achieved by UVA-LED photolysis for acetaminophen, naproxen, diclofenac, and ketoprofen. The obtained results are in agreement with an earlier study, in which very high (99%) removal of diclofenac (initial concentration of 100 ng L⁻¹) was reported by photolysis under simulated solar irradiation [52]. A moderate removal efficiency was obtained for acetaminophen by photocatalysis (72.7%) and UVA-LED photolysis (78.7%). For the elimination of naproxen, photolysis was slightly less efficient (81%) in comparison with photocatalysis, while ketoprofen achieved complete elimination by both photolytic and photocatalytic processes. Also, another study reported almost complete elimination of naproxen (initial concentration similar to that in our study) and diclofenac (initial concentration about twice as high as in our study) during solar photocatalysis with TiO₂ at t_{30W} below 150 and 300 min, respectively [6]. The elimination of ibuprofen and salicylic acid during photolysis was poor. It should be noted that adsorption of studied anti-inflammatories onto photocatalyst was poor or negative except for salicylic acid. Moderate adsorption removal of salicylic acid (45%) was achieved after 30 min of contact time, while 0% removal was observed after the adsorption reference test (210 min of contact time), which suggests possible desorption of salicylic acid from the photocatalysts.

It should be mentioned that TOC and COD values were monitored during photocatalysis with 4%-Gd- BiVO₄ (1 g L⁻¹) and photolysis (results are not shown for the sake of brevity). However, no reduction of TOC or COD was detected during 3 h of photocatalysis and photolysis, indicating relatively low photocatalytic activity. The obtained results are in agreement with an earlier study [31], where no reduction of TOC in secondary effluent was reported after 5h of solar photocatalysis with Ag/BiVO₄ (dose 0.5 and 1 g L⁻¹). Moreover, the concentration of dissolved metals and rare earth (Bi, V, and Gd) was measured before and after photocatalytic treatment by means of ICP-OES to evaluate the physicochemical stability of 4%-Gd- BiVO₄ and to ensure that the photocatalyst does not release toxic metals to the effluent during photocatalysis. None of the

three analysed elements were detected in the effluent either before or after the photocatalytic treatment. Hence, it can be assumed that 4%-Gd-BiVO₄ photocatalyst has good stability.

3.3 Photocatalytic efficiency of 4%-Gd-BiVO₄ for bacterial inactivation.

Photocatalytic efficiency was also addressed for bacterial inactivation. As discussed in section 3.2.1, photocatalytic inactivation of bacteria detected in wastewater effluent was conducted using 1 g L⁻¹ of 4%-Gd-BiVO₄, which agrees with available literature [31]. Selected examples of inactivation profiles belonging to *Enterococci* and *K. pneumoniae* species are depicted in Figure 8 a-b where the different processes, namely photolysis, 4%-Gd-BiVO₄ photocatalysis, and adsorption showed different inactivation routes. Firstly, adsorption onto the photocatalyst (in absence of UVA-LED light) reached slight inactivation on the different bacteria, i.e. 0.11, 0.15, 0.19, and 0.91 Log-removal values (LRV) were obtained for *T. coliforms*, *K. pneumoniae*, *E. coli*, and *Enterococci*, respectively. In the case of photolysis and 4%-Gd-BiVO₄-photocatalysis, notably major rates of inactivation were obtained. Kinetic rate constants for these two processes are represented in Figure 8 c.

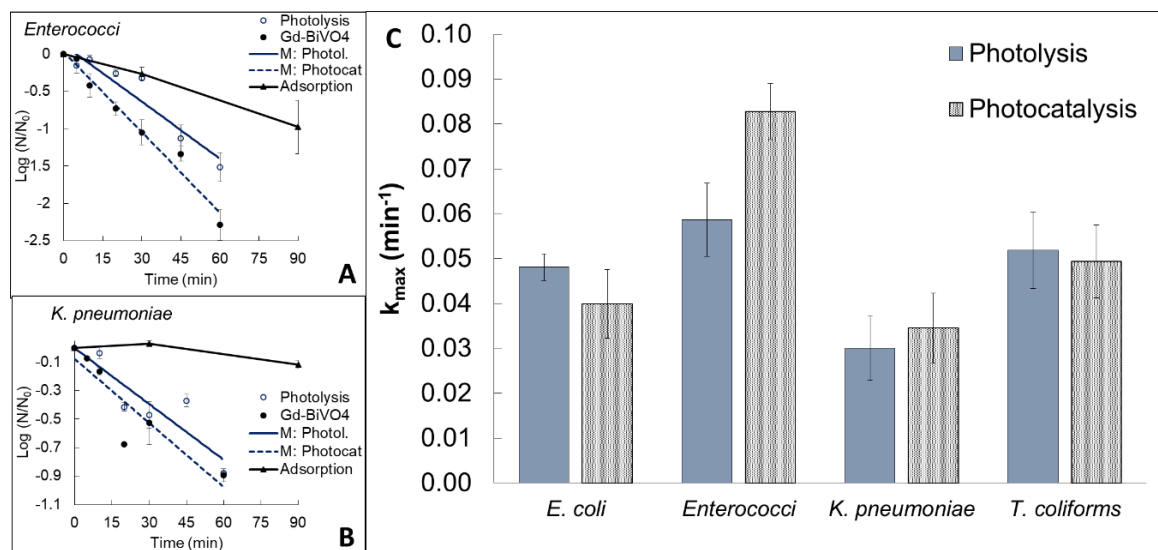


Figure 8. Selected examples of inactivation profiles obtained for a) *Enterococci*, and b) *K. pneumoniae*. Log-lineal model (M) is represented with lines on Photolysis and Photocatalytic processes (a, b). c) Kinetic rate constants (min⁻¹) obtained for photolytic (UVA-LED) and photocatalytic (1 g L⁻¹ of 4%-Gd-BiVO₄ + UVA-LED) inactivation of *E. coli*, *Enterococci*, *K. pneumoniae*, and *T. coliforms*.

Photolysis showed effectivity itself for bacterial inactivation. *K. pneumoniae* was the most resistant bacteria, since the LRV was not reached at 60 min of exposure

time, with a k_{\max} of $0.03 \pm 0.10 \text{ min}^{-1}$ in comparison with the k_{\max} obtained for the rest of bacteria which is in the range of $0.05\text{-}0.06 \text{ min}^{-1}$. It is known that direct UVA can inflict not only direct and indirect DNA damage, but also oxidative damages since some cell components absorb in the UVA region, such as catalase [53]. Thus, the higher resistance of *K. pneumoniae* can be attributed to their cellular structure. Particularly, it has been reported that *K. pneumoniae* have robust capsules that can protect it from bactericidal stressors, such as UV irradiation [54,55].

In comparison with single photolysis, an improvement in bacteria inactivation during photocatalytic processes was obtained for *Enterococci* which was quantified in an increase on k_{\max} by 41.1%, which means that the time for reach 1 LRV was reduced from 44.4 min (UVA) to 28.8 min (UVA/4%-Gd-BiVO₄). Nevertheless, this photocatalytic enhancement has not been detected for *E. coli* and T. coliforms. Also, *K. pneumoniae* showed a similar behaviour during photolysis and photocatalysis. The trend observed for bacterial inactivation by photocatalysis was *Enterococci* > T. coliforms > *E. coli* > *K. pneumoniae*. It is important to note that UV-transmittance at 370 nm notably differs in the absence of the photocatalyst (79.2%) and in the presence of it (25.7%). This has important implications in the experimental set-up since the mean UVA intensity within the photo-reactor markedly decreases. Accordingly, results reported of photocatalytic processes were obtained with rather low photonic flux in comparison with UVA photolysis, so it can be assumed that in every case, higher efficiencies are expected in the presence of photocatalyst.

As previously commented, the cell structure of the different bacteria can have a direct relationship with caused oxidative damages. For instance, *E. coli*, as gram negative bacteria are known to be sensitive to UV light, especially at high intensities [39]. This high sensitivity to UVA radiation might lead to more effective bacteria inactivation in photolysis as compared to photocatalytic processes [39,56,57] as was also observed in this study (Figure 8c). On the other hand, it was observed that *Enterococci*, which is a gram-positive bacteria, showed higher sensitivity to the photocatalytic process than to the photolytic one. Lastly, as observed in Figure 9 c, *K. pneumoniae* showed very similar inactivation rates in the presence of 4%-Gd-BiVO₄ (photocatalysis) and under direct UVA-LED radiation (photolysis). However, it is still is the most resistant bacteria against oxidative damages, suggesting the prominent capsule of these cells could protect it from direct attacks from oxidant radicals [54,55]. Though, if longer reaction times are applied, a complete inactivation can be possibly reached.

Another factor that should be taken into account is the interaction between photocatalysts and bacteria [39,42,58]. Close contact is required between bacteria and photocatalyst, since the adhesion onto the photocatalyst surface is positively correlated to the inactivation efficiency. This can be explained considering that photo-generated radicals are most likely present at photocatalyst surface and because of its short lifetime may easily interact with adsorbed bacteria, damaging its cell wall and consequently favoring bacteria inactivation [39]. In this regard, dark tests revealed that *Enterococci* showed higher adhesion onto the photocatalyst (0.91 LRV) what explains the higher photocatalytic inactivation of this group as compared to the other bacterial models studied.

Previous disinfection studies using BiVO₄ as photocatalyst have been reported [27,31,42,59]. For instance, Sharma et al. (2016), Adán et al. (2015), and Adán et al. (2016) reported high photocatalytic activity and higher antimicrobial activity in deionized water towards *E. coli* when it is compared with simple photolysis. Booshehri et al. (2017) reported similar results, in which the photocatalytic effect was also effective in well water and secondary wastewater effluent. However, they assessed the inactivation efficacy with pure strains spiked to the water matrices. These changes in experimental set-up (e.g. initial concentration of microorganisms or radiation intensities) make inactivation ratios difficult to compare between the different studies. Nonetheless, our results agree with these trends since the efficacy of 4%-Gd-BiVO₄ photocatalyst has also been confirmed in this study.

4. Conclusions

Photocatalytic activity of Gd³⁺ doped BiVO₄ was investigated through the decomposition of diclofenac in ultra-pure water (model solution) and 22 different PhACs from real urban wastewater effluent. In addition, photocatalytic inactivation of Total coliforms, *Escherichia coli*, *Enterococci*, and *Klebsiella pneumoniae* present in wastewater effluent was assessed. A UVA-LED lamp was used as irradiation source in all the performed photocatalytic studies. Concluding remarks can be summarized as follows:

- Characterization results of X-ray diffraction and X-ray photoelectron spectroscopy demonstrated that the crystalline structure of BiVO₄ was successfully doped by the Gd³⁺ ions. Moreover, three crystalline structures were identified forming a heterostructure that may favor the separation of charge carriers.

- The effect of 4%-Gd-BiVO₄ concentration on the initial disappearance rate of the diclofenac model solution was evaluated and a concentration of 1 g L⁻¹ was found to be the optimal photocatalyst dose. At the optimal dose, diclofenac decomposition reached up to 98.3% after 120 min under UVA-LED light.
- No dissolved metals (Bi, V, or Gd) were detected in effluent either before or after photocatalytic experiments. This suggests that 4%-Gd-BiVO₄ has good stability and that there will be no leaching of toxic metals in the treated effluent.
- The photocatalytic removal of PhACs in wastewater was quite variable due to the complexity of the matrix and physicochemical characteristics of each studied contaminant. Thus, high photocatalytic removal efficiency (80 – 100%) was observed for some of the studied PhACs such as naproxen, diclofenac, ketoprofen, and furosemide. On the other hand, other PhACs showed moderate removal efficiency (40 – 70%) for example, acetaminophen and azithromycin. Some of the studied PhACs such as clarithromycin or Ibuprofen showed poor removal efficiency (<30%).
- Although the irradiation (UVA-LED) by itself caused inactivation in all microbes tested, the bigger improvement from the photocatalytic treatment was appreciable in *Enterococci* bacterial indicator by increasing the k_{\max} in 41.1%. *Enterococci* were the most sensitive bacteria to photocatalytic treatment whereas *K. pneumoniae* showed the highest resistance for both processes.
- The capability of 4%-Gd-BiVO₄ for bacteria inactivation and PhACs elimination from real wastewater effluent was demonstrated at laboratory scale. However, not significant changes were observed on TOC and COD values of wastewater effluent after photocatalytic treatment (180 min of contact time; UVA dose = 139.5 Wh m⁻², t_{30W} = 279 min⁻¹). Thus, further studies are required in order to improve the photocatalytic activity of the synthesized material for possible up-scale application in wastewater treatment.

5. References

- [1] N.H. Tran, M. Reinhard, K.Y.-H. Gin, Occurrence and fate of emerging contaminants in municipal wastewater treatment plants from different geographical regions-a review, *Water Res.* 133 (2018) 182–207. doi:10.1016/J.WATRES.2017.12.029.
- [2] T. Deblonde, C. Cossu-Leguille, P. Hartemann, Emerging pollutants in wastewater: A review of the literature, *Int. J. Hyg. Environ. Health.* 214 (2011) 442–448. doi:10.1016/j.ijheh.2011.08.002.
- [3] I.Y. López-Pacheco, A. Silva-Núñez, C. Salinas-Salazar, A. Arévalo-Gallegos, L.A. Lizarazo-Holguin, D. Barceló, H.M.N. Iqbal, R. Parra-Saldívar, Anthropogenic contaminants of high concern: Existence in water resources and their adverse effects, *Sci. Total Environ.* 690 (2019) 1068–1088. doi:10.1016/j.scitotenv.2019.07.052.
- [4] A. Chiffre, F. Degiorgi, A. Bulete, L. Spinner, P.M. Badot, Occurrence of pharmaceuticals in WWTP effluents and their impact in a karstic rural catchment of Eastern France, *Environ. Sci. Pollut. Res.* 23 (2016) 25427–25441. doi:10.1007/s11356-016-7751-5.
- [5] European Comision, COMMISSION IMPLEMENTING DECISION (EU) 2018/ 840 establishing a watch list of substances for Union-wide monitoring in the field of water policy pursuant to Directive 2008/105/EC of the European Parliament and of the Council and repealing Commission Impleme, Brussels, 2018.
- [6] L. Prieto-Rodriguez, S. Miralles-Cuevas, I. Oller, a Agüera, G. Li Puma, S. Malato, Treatment of emerging contaminants in wastewater treatment plants (WWTP) effluents by solar photocatalysis using low TiO₂ concentrations., *J. Hazard. Mater.* 211–212 (2012) 131–7. doi:10.1016/j.jhazmat.2011.09.008.
- [7] L. Rizzo, S. Malato, D. Antakyali, V.G. Beretsou, M.B. Đolić, W. Gernjak, E. Heath, I. Ivancev-Tumbas, P. Karaolia, A.R. Lado Ribeiro, G. Mascolo, C.S. McArdell, H. Schaar, A.M.T. Silva, D. Fatta-Kassinos, Consolidated vs new advanced treatment methods for the removal of contaminants of emerging concern from urban wastewater, *Sci. Total Environ.* 655 (2019) 986–1008. doi:10.1016/j.scitotenv.2018.11.265.
- [8] G. Maniakova, K. Kowalska, S. Murgolo, G. Mascolo, G. Libralato, G. Lofrano, O. Sacco, M. Guida, L. Rizzo, Comparison between heterogeneous and homogeneous solar driven advanced oxidation processes for urban wastewater

treatment: Pharmaceuticals removal and toxicity, *Sep. Purif. Technol.* 236 (2020). doi:10.1016/j.seppur.2019.116249.

[9] J. You, Y. Guo, R. Guo, X. Liu, A review of visible light-active photocatalysts for water disinfection: Features and prospects, *Chem. Eng. J.* 373 (2019) 624–641. doi:10.1016/j.cej.2019.05.071.

[10] G. Iervolino, I. Zammit, V. Vaiano, L. Rizzo, Limitations and Prospects for Wastewater Treatment by UV and Visible-Light-Active Heterogeneous Photocatalysis: A Critical Review, *Top. Curr. Chem.* 378 (2020) 1–40. doi:10.1007/s41061-019-0272-1.

[11] P. Ganguly, C. Byrne, A. Breen, S.C. Pillai, Antimicrobial activity of photocatalysts: Fundamentals, mechanisms, kinetics and recent advances, *Appl. Catal. B Environ.* 225 (2018) 51–75. doi:10.1016/j.apcatb.2017.11.018.

[12] B. Tryba, S. Jafari, M. Sillanpää, A. Nitta, B. Ohtani, A.W. Morawski, Influence of TiO₂ structure on its photocatalytic activity towards acetaldehyde decomposition, *Appl. Surf. Sci.* 470 (2019) 376–385. doi:10.1016/j.apsusc.2018.11.137.

[13] L. V. Bora, R.K. Mewada, Visible/solar light active photocatalysts for organic effluent treatment: Fundamentals, mechanisms and parametric review, *Renew. Sustain. Energy Rev.* 76 (2017) 1393–1421. doi:10.1016/j.rser.2017.01.130.

[14] S. Helali, M.I. Polo-López, P. Fernández-Ibáñez, B. Ohtani, F. Amano, S. Malato, C. Guillard, Solar photocatalysis: A green technology for E. coli contaminated water disinfection. Effect of concentration and different types of suspended catalyst, *J. Photochem. Photobiol. A Chem.* 276 (2014) 31–40. doi:10.1016/j.jphotochem.2013.11.011.

[15] A. Malathi, J. Madhavan, M. Ashokkumar, P. Arunachalam, A review on BiVO₄ photocatalyst: Activity enhancement methods for solar photocatalytic applications, *Appl. Catal. A Gen.* 555 (2018) 47–74. doi:10.1016/j.apcata.2018.02.010.

[16] W. Jo, R.J. Tayade, New Generation Energy-Efficient Light Source for Photocatalysis: LEDs for Environmental Applications, *Ind. Eng. Chemistry Res.* 53 (2014) 2073–2084.

[17] I. Levchuk, M. Kralova, J.J. Rueda-Márquez, J. Moreno-Andrés, S. Gutiérrez-Alfaro, P. Dzik, S. Parola, M. Sillanpää, R. Vahala, M.A. Manzano,

Antimicrobial activity of printed composite TiO₂/SiO₂ and TiO₂/SiO₂/Au thin films under UVA-LED and natural solar radiation, *Appl. Catal. B Environ.* 239 (2018) 609–618. doi:10.1016/J.APCATB.2018.08.051.

[18] L.H. Levine, J.T. Richards, J.L. Coutts, R. Soler, F. Maxik, R.M. Wheeler, Feasibility of ultraviolet-light-emitting diodes as an alternative light source for photocatalysis, *J. Air Waste Manag. Assoc.* 61 (2011) 932–940. doi:10.1080/10473289.2011.596746.

[19] S.D. Dolić, D.J. Jovanović, K. Smits, B. Babić, M. Marinović-Cincović, S. Porobić, M.D. Dramićanin, A comparative study of photocatalytically active nanocrystalline tetragonal zircon-type and monoclinic scheelite-type bismuth vanadate, *Ceram. Int.* 44 (2018) 17953–17961. doi:10.1016/j.ceramint.2018.06.272.

[20] X. Chen, L. Li, T. Yi, W. Zhang, X. Zhang, L. Wang, Microwave assisted synthesis of sheet-like Cu/BiVO₄ and its activities of various photocatalytic conditions, *J. Solid State Chem.* 229 (2015) 141–149. doi:10.1016/j.jssc.2015.05.026.

[21] E.M. Siedlecka, Application of Bismuth-Based Photocatalysts in Environmental Protection, in: Inamuddin, A. Asiri, E. Lichtfouse (Eds.), *Nanophotocatalysis Environ. Appl. Environ. Chem. a Sustain. World*, Springer Cham, Switzerland, 2020: pp. 87–118. doi:10.1007/978-3-030-12619-3_4.

[22] X. Meng, Z. Zhang, Bismuth-based photocatalytic semiconductors: Introduction, challenges and possible approaches, *J. Mol. Catal. A Chem.* 423 (2016) 533–549. doi:10.1016/j.molcata.2016.07.030.

[23] R. He, S. Cao, P. Zhou, J. Yu, Recent advances in visible light Bi-based photocatalysts, *Chinese J. Catal.* 35 (2014) 989–1007. doi:10.1016/s1872-2067(14)60075-9.

[24] S. Obregón, G. Colón, On the origin of the photocatalytic activity improvement of BiVO₄ through rare earth tridoping, *Appl. Catal. A Gen.* 501 (2015) 56–62. doi:10.1016/j.apcata.2015.04.032.

[25] X. Luo, G. Zhu, J. Peng, X. Wei, M. Hojamberdiev, L. Jin, P. Liu, Enhanced photocatalytic activity of Gd-doped porous β-Bi₂O₃ photocatalysts under visible light irradiation, *Appl. Surf. Sci.* 351 (2015) 260–269. doi:10.1016/j.apsusc.2015.05.137.

- [26] X. Gao, Z. Wang, X. Zhai, F. Fu, W. Li, The synthesise of lanthanide doped BiVO₄ and its enhanced photocatalytic activity, *J. Mol. Liq.* 211 (2015) 25–30. doi:10.1016/J.MOLLIQ.2015.06.058.
- [27] C. Adán, J. Marugán, S. Obregón, G. Colón, Photocatalytic Escherichia coli inactivation by means of trivalent Er³⁺, Y³⁺ doping of BiVO₄ system, *Appl. Catal. A Gen.* 526 (2016) 126–131. doi:10.1016/j.apcata.2016.08.002.
- [28] A.M. Al-Hamdi, M. Sillanpää, J. Dutta, Gadolinium doped tin dioxide nanoparticles: an efficient visible light active photocatalyst, *J. Rare Earths.* 33 (2015) 1275–1283. doi:10.1016/S1002-0721(14)60557-3.
- [29] A.W. Xu, Y. Gao, H.Q. Liu, The preparation, characterization, and their photocatalytic activities of rare-earth-doped TiO₂ nanoparticles, *J. Catal.* 207 (2002) 151–157. doi:10.1006/jcat.2002.3539.
- [30] A.P. Reverberi, P.S. Varbanov, M. Vocciante, B. Fabiano, Bismuth oxide-related photocatalysts in green nanotechnology: A critical analysis, *Front. Chem. Sci. Eng.* 12 (2018) 878–892. doi:10.1007/s11705-018-1744-5.
- [31] A.Y. Booshehri, M.I. Polo-Lopez, M. Castro-Alfárez, P. He, R. Xu, W. Rong, S. Malato, P. Fernández-Ibáñez, Assessment of solar photocatalysis using Ag/BiVO₄ at pilot solar Compound Parabolic Collector for inactivation of pathogens in well water and secondary effluents, *Catal. Today.* 281 (2017) 124–134. doi:10.1016/J.CATTOD.2016.08.016.
- [32] A.R. Lado Ribeiro, N.F.F. Moreira, G. Li Puma, A.M.T. Silva, Impact of water matrix on the removal of micropollutants by advanced oxidation technologies, *Chem. Eng. J.* 363 (2019) 155–173. doi:10.1016/j.cej.2019.01.080.
- [33] R.S. Ribeiro, Z. Frontistis, D. Mantzavinos, A.M. T Silva, J.L. Faria, H.T. Gomes, Screening of heterogeneous catalysts for the activated persulfate oxidation of sulfamethoxazole in aqueous matrices. Does the matrix affect the selection of catalyst?, *J. Chem. Technol. Biotechnol.* 94 (2019) 2425–2432. doi:10.1002/jctb.6080.
- [34] R. María Baena-Nogueras, M. G. Pintado-Herrera, E. González-Mazo, P. A. Lara-Martín, Determination of Pharmaceuticals in Coastal Systems Using Solid Phase Extraction (SPE) Followed by Ultra Performance Liquid Chromatography – tandem Mass Spectrometry (UPLC-MS/MS), *Curr. Anal. Chem.* 12 (2016) 183–201. doi:10.2174/1573411012666151009193254.

- [35] W. Yin, W. Wang, M. Shang, L. Zhou, S. Sun, L. Wang, BiVO₄ Hollow Nanospheres: Anchoring Synthesis, Growth Mechanism, and Their Application in Photocatalysis, *Eur. J. Inorg. Chem.* (2009) 4379–4384. doi:10.1002/ejic.200900614.
- [36] M. Sevilla, A.B. Fuertes, Chemical and Structural Properties of Carbonaceous Products Obtained by Hydrothermal Carbonization of Saccharides, *Chem. - A Eur. J.* 15 (2009) 4195–4203. doi:10.1002/chem.200802097.
- [37] D. Stülten, S. Zühlke, M. Lamshöft, M. Spiteller, Occurrence of diclofenac and selected metabolites in sewage effluents, *Sci. Total Environ.* 405 (2008) 310–316. doi:10.1016/j.scitotenv.2008.05.036.
- [38] American Public Health Association, *Standard Methods for the Examination of Water & Wastewater*, 2005.
- [39] I. Levchuk, T. Homola, J. Moreno-Andrés, J.J. Rueda-Márquez, P. Dzik, M.Á. Moríñigo, M. Sillanpää, M.A. Manzano, R. Vahala, Solar photocatalytic disinfection using ink-jet printed composite TiO₂/SiO₂ thin films on flexible substrate: Applicability to drinking and marine water, *Sol. Energy.* 191 (2019) 518–529. doi:10.1016/j.solener.2019.09.038.
- [40] K. Zhong, H. Gao, J. Feng, Y. Zhang, K. Lai, Facile synthesis of Z-scheme Se/BiVO₄ heterojunction with enhanced visible-light-driven photocatalytic performance, *J. Mater. Sci.* 54 (2019) 10632–10643. doi:10.1007/s10853-019-03634-1.
- [41] Q. Yuan, L. Chen, M. Xiong, J. He, S.L. Luo, C.T. Au, S.F. Yin, Cu₂O/BiVO₄ heterostructures: Synthesis and application in simultaneous photocatalytic oxidation of organic dyes and reduction of Cr(VI) under visible light, *Chem. Eng. J.* 255 (2014) 394–402. doi:10.1016/j.cej.2014.06.031.
- [42] C. Adán, J. Marugán, S. Obregón, G. Colón, Photocatalytic activity of bismuth vanadates under UV-A and visible light irradiation: Inactivation of *Escherichia coli* vs oxidation of methanol, *Catal. Today.* 240 (2015) 93–99. doi:10.1016/j.cattod.2014.03.059.
- [43] O. Monfort, G. Plesch, Bismuth vanadate-based semiconductor photocatalysts: a short critical review on the efficiency and the mechanism of photodegradation of organic pollutants, *Environ. Sci. Pollut. Res.* 25 (2018) 19362–19379.

- [44] C. Regmi, Y.K. Kshetri, R.P. Pandey, S.W. Lee, Visible-light-driven S and W co-doped dendritic BiVO₄ for efficient photocatalytic degradation of naproxen and its mechanistic analysis, *Mol. Catal.* 453 (2018) 149–160. doi:10.1016/j.mcat.2018.05.008.
- [45] M. Wang, H. Zheng, Q. Liu, C. Niu, Y. Che, M. Dang, High performance B doped BiVO₄ photocatalyst with visible light response by citric acid complex method, *Spectrochim. Acta Part A Mol. Biomol. Spectrosc.* 114 (2013) 74–79. doi:10.1016/J.SAA.2013.05.032.
- [46] M. Moradi, G. Moussavi, K. Yaghmaeian, A. Yazdanbakhsh, V. Srivastava, M. Sillanpää, Synthesis of novel Ag-doped S-MgO nanosphere as an efficient UVA/LED-activated photocatalyst for non-radical oxidation of diclofenac: Catalyst preparation and characterization and photocatalytic mechanistic evaluation, *Appl. Catal. B Environ.* 260 (2020) 118128. doi:10.1016/j.apcatb.2019.118128.
- [47] I. Tbesi, M. Benito, J. Llorca, E. Molins, S. Sayadi, W. Najjar, Silver and manganese co-doped titanium oxide aerogel for effective diclofenac degradation under UV-A light irradiation, *J. Alloys Compd.* 779 (2019) 314–325. doi:10.1016/j.jallcom.2018.11.083.
- [48] V.C. Sarasidis, K. V. Plakas, S.I. Patsios, A.J. Karabelas, Investigation of diclofenac degradation in a continuous photo-catalytic membrane reactor. Influence of operating parameters, *Chem. Eng. J.* 239 (2014) 299–311. doi:10.1016/j.cej.2013.11.026.
- [49] A.S. Mestre, A.P. Carvalho, Photocatalytic degradation of pharmaceuticals carbamazepine, diclofenac, and sulfamethoxazole by semiconductor and carbon materials: A review, *Molecules.* 24 (2019). doi:10.3390/molecules24203702.
- [50] J.J. Rueda-Marquez, I. Levchuk, P. Fernández Ibañez, M. Sillanpää, A critical review on application of photocatalysis for toxicity reduction of real wastewaters, *J. Clean. Prod.* (2020) 120694. doi:10.1016/j.jclepro.2020.120694.
- [51] R. Loos, R. Carvalho, D.C. António, S. Comero, G. Locoro, S. Tavazzi, B. Paracchini, M. Ghiani, T. Lettieri, L. Blaha, B. Jarosova, S. Voorspoels, K. Servaes, P. Haglund, J. Fick, R.H. Lindberg, D. Schwesig, B.M. Gawlik, EU-wide monitoring survey on emerging polar organic contaminants in wastewater treatment plant effluents, *Water Res.* 47 (2013) 6475–6487. doi:10.1016/j.watres.2013.08.024.

- [52] R.M. Baena-Nogueras, E. González-Mazo, P.A. Lara-Martín, Degradation kinetics of pharmaceuticals and personal care products in surface waters: photolysis vs biodegradation, *Sci. Total Environ.* 590–591 (2017) 643–654. doi:10.1016/j.scitotenv.2017.03.015.
- [53] S. Giannakis, M.I. Polo López, D. Spuhler, J.A. Sánchez Pérez, P. Fernández Ibáñez, C. Pulgarin, Solar disinfection is an augmentable, in situ-generated photo-Fenton reaction—Part 1: A review of the mechanisms and the fundamental aspects of the process, *Appl. Catal. B Environ.* 199 (2016) 199–223. doi:10.1016/j.apcatb.2016.06.009.
- [54] S. Aguilar, D. Rosado, J. Moreno-Andrés, L. Cartuche, D. Cruz, A. Acevedo-Merino, E. Nebot, Inactivation of a wild isolated *Klebsiella pneumoniae* by photo-chemical processes: UV-C, UV-C/H₂O₂ and UV-C/H₂O₂/Fe³⁺, *Catal. Today.* 313 (2018) 94–99. doi:10.1016/j.cattod.2017.10.043.
- [55] D. Venieri, I. Gounaki, M. Bikouvaraki, V. Binas, A. Zachopoulos, G. Kiriakidis, D. Mantzavinos, Solar photocatalysis as disinfection technique: Inactivation of *Klebsiella pneumoniae* in sewage and investigation of changes in antibiotic resistance profile, *J. Environ. Manage.* 195 (2017) 140–147. doi:10.1016/j.jenvman.2016.06.009.
- [56] A.K. Benabbou, Z. Derriche, C. Felix, P. Lejeune, C. Guillard, Photocatalytic inactivation of *Escherichia coli*. Effect of concentration of TiO₂ and microorganism, nature, and intensity of UV irradiation, *Appl. Catal. B Environ.* 76 (2007) 257–263. doi:10.1016/j.apcatb.2007.05.026.
- [57] J. Rodríguez-Chueca, S. Guerra-Rodríguez, J.M. Ruez, M.J. López-Muñoz, E. Rodríguez, Assessment of different iron species as activators of S₂O₈²⁻ and HSO₅⁻ for inactivation of wild bacteria strains, *Appl. Catal. B Environ.* 248 (2019) 54–61. doi:10.1016/j.apcatb.2019.02.003.
- [58] C. Pablos, R. Van Grieken, J. Marugán, I. Chowdhury, S.L. Walker, Study of bacterial adhesion onto immobilized TiO₂: Effect on the photocatalytic activity for disinfection applications, *Catal. Today.* 209 (2013) 140–146. doi:10.1016/j.cattod.2012.12.010.
- [59] R. Sharma, Uma, S. Singh, A. Verma, M. Khanuja, Visible light induced bactericidal and photocatalytic activity of hydrothermally synthesized BiVO₄ nano-octahedrals, *J. Photochem. Photobiol. B Biol.* 162 (2016) 266–272. doi:10.1016/j.jphotobiol.2016.06.035.

Chapter 6

Conclusions

6.1 Conclusion

Different materials were synthesized and characterized in order to be applied in the removal of organic contaminants in the water. The physical and chemical modifications that were made to the prepared materials were shown to notably improve their performance during treatment compared to unmodified pristine materials. The effectiveness of the materials was also successfully tested under different experimental conditions such as pure water matrices and real effluents, or different light sources in the case of photocatalysis.

6.2 Contributions

Different materials were synthesized, modified, characterized, and successfully applied to the removal of organic pollutants in water. Specifically:

- Titanate nanotubes and modified titanate nanotubes were obtained by the hydrothermal method. The synthesized materials were applied as absorbents for contaminants removal in water and groundwater showing good adsorption capacity.
- BiVO_4 was synthesized by a thermal method and successfully doped with different concentrations of Gd^{3+} . The photocatalysts synthesized showed good photocatalytic activity under visible light for the degradation of disrupting endocrine compounds such as bisphenol A, bisphenol S, and bisphenol AF. A decomposition pathway was proposed.
- The photocatalytic performance of BiVO_4 doped with 4% of Gd^{3+} in molar mass was investigated through the decomposition of 22 different pharmaceutically active compounds naturally present in a real wastewater effluent using UV-LED as a light source. Moreover, disinfection tests were performed.
- A ternary z-scheme composite ($\text{Bi}_2\text{O}_3/\text{rGO}/\text{Mo}_n\text{O}_{3n-1}$) was synthesized through hydrothermal and thermal methods. The photocatalytic efficiency and the influence of the three components were corroborated through the degradation of bisphenol A and acetaminophen in pure water and, groundwater samples under UV and visible light.
- All the synthesized materials were successfully applied over real water matrices such as groundwater samples collected from the

metropolitan area of Monterrey as well as urban wastewater effluent collected from Viikinmäki wastewater treatment plant in Helsinki.

6.3 Future work

It has been demonstrated that the efficiency of a photocatalytic or adsorbent material can be improved by modifying its physical and chemical characteristics in their nano or micro scale. Therefore, there is a wide field in research to keep investigating new ways to modify those materials to improve their physicochemical properties and efficiencies during treatment. Besides, it is desirable to have more energy-efficient and zero-waste treatment processes.

On the other hand, it would be interesting to study in detail the formation of intermediate products during the treatment processes and corroborate their toxicity to avoid adverse effects in the ecosystems. There is also a great area of opportunity in the field of photocatalytic disinfection, where the synthesized materials could be modified to be effectively applied in such processes for inactivation of pathogens naturally present in wastewater effluents.

After testing the performance of the materials at the laboratory level, the next step is to test their effectiveness on a large scale. Then, it is important to look for alternatives that facilitate the recovery and regeneration of the materials so that they can be used in multiple cycles. Also, it would be relevant to continue research towards the immobilization of the adsorbent and photocatalytic materials, seeking to preserve their catalytic activity as much as possible.

Supplementary information

S1: Table A. Chemical and physical properties of selected pollutants.

Pollutant	Formula	Molecular Weight (gmol ⁻¹)	Water Solubility (mgL ⁻¹)	Isoelectric point	pKa 1	pKa 2	Log Kow
2,4-Dichlorophenol	C ₆ H ₄ Cl ₂ O	163	4500 at 20°C	N/A	7.89		3.06
2,4,6-Trichlorophenol	C ₆ H ₂ Cl ₃ OH	197.45	900	N/A	6.23		3.69
Captopril	C ₉ H ₁₅ N ₃ S	217.28	160000	1.38	3.7	9.8	0.34
Oxytetracycline	C ₂₂ H ₂₄ N ₂ O ₉	460.434	313	5.01	3.3	9.1	-0.9
Tolazamide	C ₁₄ H ₂₁ N ₃ O ₃ S	311.4	65.4 at 30°C	2.84	3.6		2.69
Metformin	C ₄ H ₁₁ N ₅	129.167	1060000 at 25°C	N/A	12.33		-2.64
Bisphenol A	C ₁₅ H ₁₆ O ₂	228.29	150 at 21.5°C		10.29		3.32
Bisphenol S	C ₁₂ H ₁₀ O ₄ S	250.27	1100		7		1.65
Bisphenol AF	C ₁₅ H ₁₀ F ₆ O ₂	336.23	32		8.74		4.47
Diclofenac	C ₁₄ H ₁₁ Cl ₂ NO ₂	296.15	2.37 at 25°C		4.18		4.51
Acetaminophen	C ₈ H ₉ NO ₂	151.16	14000 at 25°C		9.86		0.46

S2: XRD diffraction patterns of pristine and Gd³⁺ doped BiVO₄ materials.

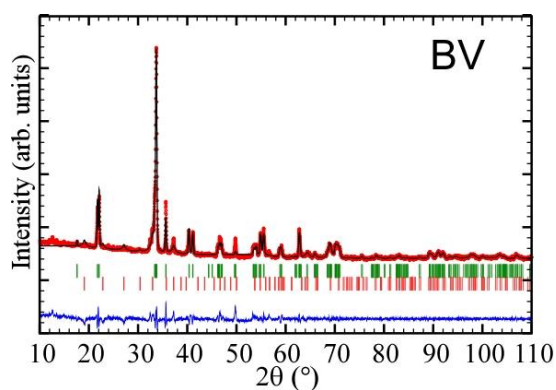


Figure S1. Pattern matching from X-ray diffraction data of the material BiVO₄ obtained from synthesis. Experimental data (Red dots), calculated for the monoclinic Clinobisvanite and Tetragonal bismuth oxide structures (Black continuous line), differences (Blue line), Bragg positions of Clinobisvanite (Green lines) and Tetragonal bismuth oxide structures (Red lines).

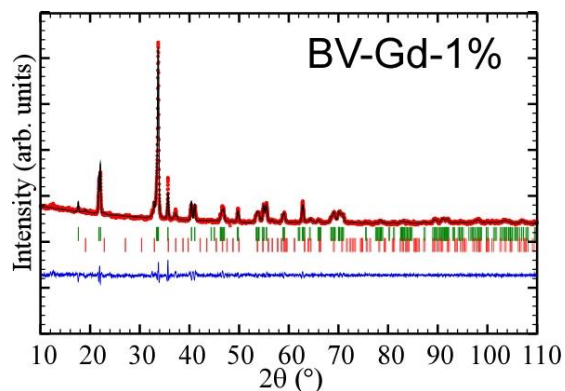


Figure S2. Pattern matching from X-ray diffraction data of the material 1% Gd in BiVO₄ system obtained from synthesis. Experimental data (Red dots), calculated for the monoclinic Clinobisvanite and Tetragonal bismuth oxide structures (Black continuous line), differences (Blue line), Bragg positions of Clinobisvanite (Green lines) and Tetragonal bismuth oxide structures (Red lines).

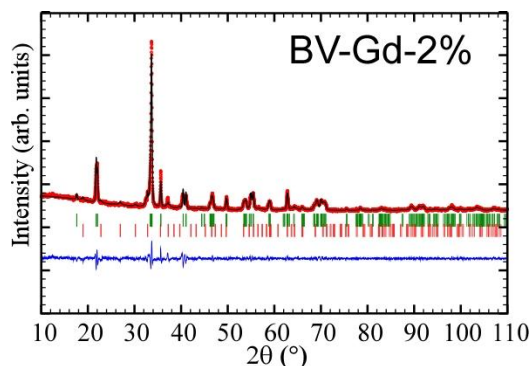


Figure S3. Pattern matching from X-ray diffraction data of the material 2% Gd in BiVO₄ system obtained from synthesis. Experimental data (Red dots), calculated for the monoclinic Clinobisvanite and Tetragonal bismuth oxide structures (Black continuous line), differences (Blue line), Bragg positions of Clinobisvanite (Green lines) and Tetragonal bismuth oxide structures (Red lines).

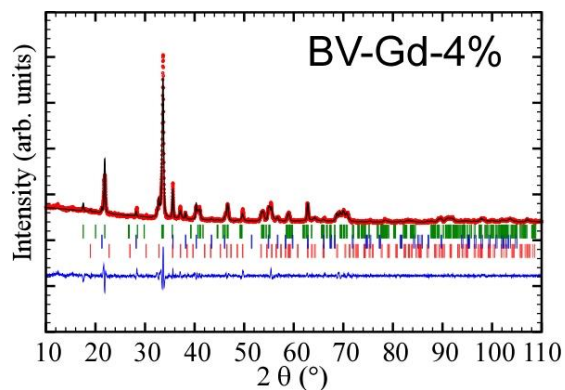


Figure S4. Pattern matching from X-ray diffraction data of the material 4% Gd in BiVO_4 system obtained from synthesis. Experimental data (Red dots), calculated for the monoclinic $\text{Bi}_{0.95}\text{Gd}_{0.05}\text{VO}_4$, Tetragonal bismuth oxide and Tetragonal dreyerite BiVO_4 structures (Black continuous line), differences (Blue line), Bragg positions of $\text{Bi}_{0.95}\text{Gd}_{0.05}\text{VO}_4$ (Green lines), Tetragonal dreyerite (Blue lines) and Tetragonal bismuth oxide structures (Red lines).

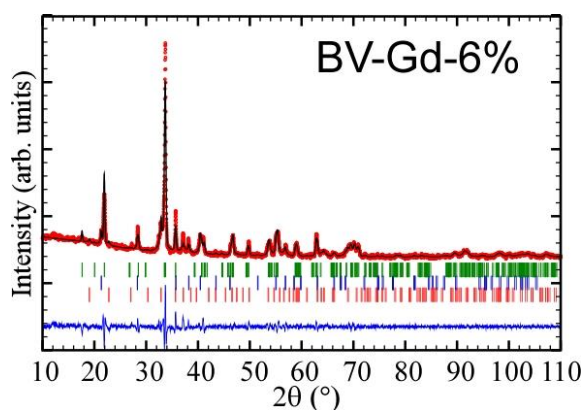


Figure S5. Pattern matching from X-ray diffraction data of the material 6% Gd in BiVO_4 system obtained from synthesis. Experimental data (Red dots), calculated for the monoclinic $\text{Bi}_{0.95}\text{Gd}_{0.05}\text{VO}_4$, Tetragonal bismuth oxide and Tetragonal dreyerite BiVO_4 structures (Black continuous line), differences (Blue line), Bragg positions of $\text{Bi}_{0.95}\text{Gd}_{0.05}\text{VO}_4$ (Green lines), Tetragonal dreyerite (Blue lines) and Tetragonal bismuth oxide structures (Red lines).

S3: Shear defect (Magnéli phases) for $(\text{Mo}, \text{W})_n\text{O}_{3n-1}$ ($n= 8, 9, 10, 11, 12, 13, 14$)

It has been noted that the removal of anions from some transition metal oxides can be accommodated by ordered planar defects rather than by random distributions of vacancies, such process is known as shear defect. The best known crystal shear structures are the so-called Magnéli phases $(\text{Mo}, \text{W})_n\text{O}_{3n-1}$ ($n= 8, 9, 10, 11, 12, 13, 14$) where the shear planes are regularly spaced [1]. Usually, these structures consist of blocks of perfect ReO_3 type structure joined together along planes of discontinuity (shear planes). The normal MoO_3 crystals are composed of cubic ReO_3 type structure, which consists of MoO_6 octahedra linked by sharing corners, as shown in figure S1a. On the other hand, in Mo_9O_{26} , due to the removal of oxygen, blocks of ReO_3 type structure are joined along shear planes where groups of four octahedra share edges, as shown in figure S1b, where the shear planes are regularly spaced [2 – 5].

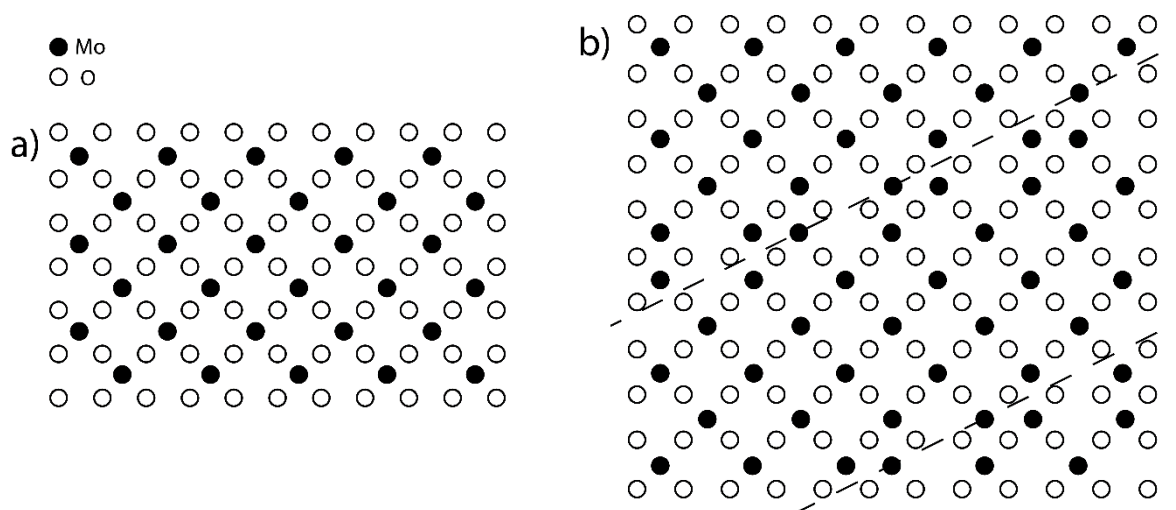


Figure S6. a) The cubic ReO₃ type structure of MoO₃ projected onto (001) where MoO₆ octahedra only share corners. b) Mo₉O₂₆ structure where the ReO₃ type structures are joined together along shear planes (dashed lines) and groups of four octahedral share edges instead of corners.

References:

- [1] A. Magnéli, The Crystal Structure of Mo₉O₂₆ (β' -Molybdenum Oxide) and Mo₈O₂₃ (β -Molybdenum Oxide), *Acta Chem. Scand.* 2 (1948) 501–517.
- [2] L.A. Bursill, Crystallographic Shear in Molybdenum Trioxide, *Proc. R. Soc. A Math. Phys. Eng. Sci.* 311 (1969) 267–290. doi:10.1098/rspa.1969.0118.
- [3] D. Wang, D. Su, R. Schlögl, Crystallographic shear defect in molybdenum oxides: Structure and TEM of molybdenum sub-oxides Mo₁₈O₅₂ and Mo₈O₂₃, *Cryst. Res. Technol.* 38 (2003) 153–159. doi:10.1002/crat.200310018.
- [4] M. Sato, M. Onoda, Y. Matsuda, Structural transitions in Mo_nO_{3n-1} (n=9 and 10), *J. Phys. C Solid State Phys.* 20 (1987) 4763–4771. doi:10.1088/0022-3719/20/29/013.
- [5] R.L. Smith, G.S. Rohrer, Scanning Probe Microscopy of Cleaved Molybdates: α -MoO₃(010), Mo₁₈O₅₂(100), Mo₈O₂₃(010), and η -Mo₄O₁₁(100), *J. Solid State Chem.* 124 (1996) 104–115. doi:10.1006/jssc.1996.0213.

S4: Possible mechanism for photogenerated e⁻/h⁺ pairs separation and transport at the interface of the BGM composite.

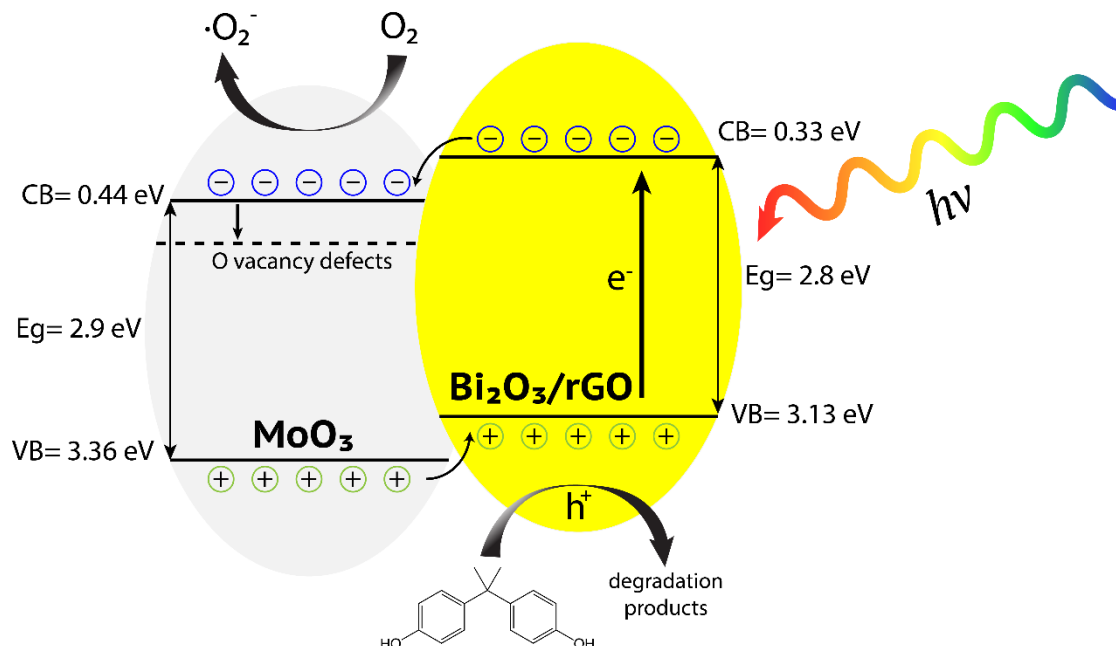


Figure S7. Possible mechanism for photogenerated e⁻/h⁺ pairs separation and transport at the interface of the BGM composite.

From figure S3 it can be seen that the photogenerated h⁺ are transferred from the VB of MoO₃ to the VB of Bi₂O₃ where the organic molecules (RhB, BPA and AMP) are directly oxidized to their corresponding degradation products. At the same time, photogenerated e⁻ are transferred from the CB of Bi₂O₃ to the CB of MoO₃ to reduce O₂ to O₂⁻ [1], which is in agreement with the results obtained from the photocatalytic activity experiments in the presence of scavenger species. These results are also in agreement with the results obtained by Zhao et al. [2] where they demonstrated that the degradation of BPA over Bi₂O₃ is initiated by its direct oxidation by the photogenerated h⁺.

References:

- [1] Bi₂O₃/MoO₃ composite nanocatalyst with improved photocatalytic activity under visible light, *Chem. Phys. Lett.* 706 (2018) 208–214. doi:10.1016/J.CPLETT.2018.06.006.
- [2] L. Zhao, X. Xiao, L. Peng, F.L. Gu, R.Q. Zhang, Visible-light photocatalytic mechanism of bisphenol-A on nano-Bi₂O₃: a combined DFT calculation and experimental study, *RSC Adv.* 4 (2014) 10343. doi:10.1039/c3ra46783j.

S5: STEM micrographs of BGM(300:1) composite after 6 photocatalytic cycles.

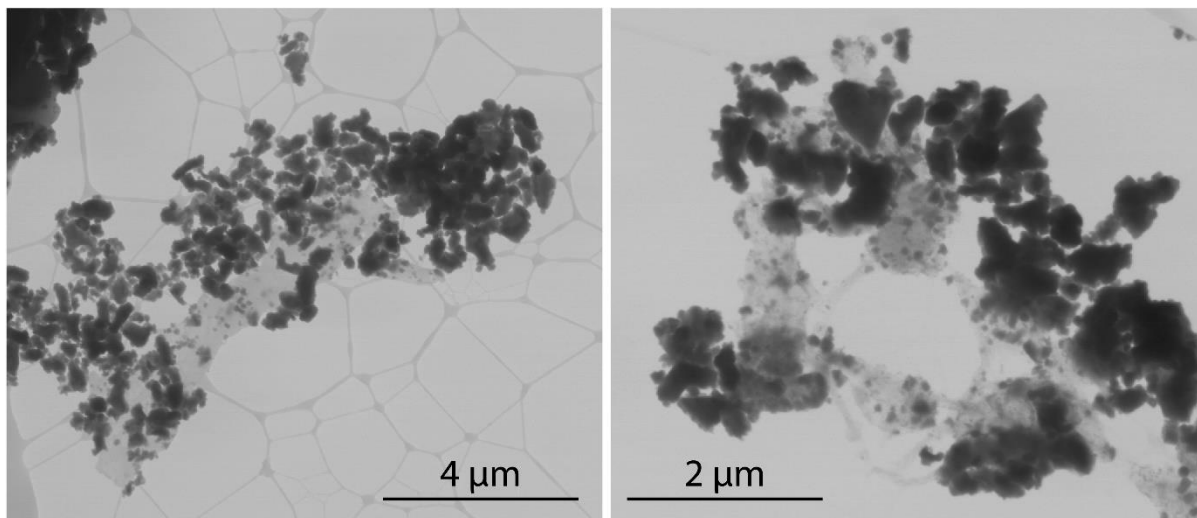
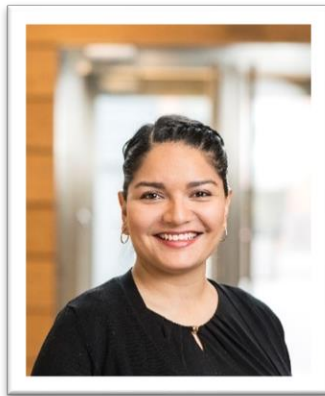


Figure S8. STEM micrographs of BGM(300:1) composite after 6 photocatalytic cycles.

Curriculum Vitae



Carolina Orona Návar was born in Durango, Durango, Mexico on November 13th, 1990. She received the Bachelor of Engineering degree in Chemical Engineering from Instituto Tecnológico de Durango in July 2013. After that, she earned the Master of Science degree from Instituto Tecnológico y de Estudios Superiores de Monterrey, Campus Monterrey in May 2017. She was accepted into the graduate program in Sciences and Engineering in August 2017. She is currently a Ph.D. candidate and a team member in the Laboratory of Environmental Nanotechnology at Water Center for Latin America and the Caribbean in Tecnológico de Monterrey. Her research interests include fundamental as well as applied aspects of novel materials for efficient removal of organic pollutants from water and wastewater through advanced treatment processes. She conducts research with enthusiasm looking to improve her skills and expand her knowledge.

This document was typed in using Microsoft Word by Carolina Orona Návar